

Contents lists available at ScienceDirect

Cement and Concrete Research

journal homepage: www.elsevier.com/locate/cemconres





Advances in atomistic modeling and understanding of drying shrinkage in cementitious materials

Mohammad Javad Abdolhosseini Qomi ^{a,1}, Laurent Brochard ^{b,1}, Tulio Honorio ^{c,1}, Ippei Maruyama ^{d,e,1}, Matthieu Vandamme ^{b,*,1}

- ^a Department of Civil and Environmental Engineering, Henry Samueli School of Engineering, University of California Irvine, E4130 Engineering Gateway, Irvine, CA 92697. United States
- ^b Laboratoire Navier, Ecole des Ponts ParisTech, Univ Gustave Eiffel, CNRS, Marne-la-Vallée, France
- ^c Université Paris-Saclay, ENS Paris-Saclay, CNRS, LMT Laboratoire de Mécanique et Technologie, 91190 Gif-sur-Yvette, France
- ^d Graduate School of Environmental Engineering, Nagoya University, Furocho, Chikusa-ku, Nagoya, 461-8603, Aichi, Japan
- ^e Graduate School of Engineering, The University of Tokyo, Hongo, Bunkyo-ku, 113-8656 Tokyo, Japan

ARTICLE INFO

Keywords: Molecular simulations Drying shrinkage Adsorption C-S-H Confined fluids

ABSTRACT

Despite more than a century of research, drying shrinkage still causes unwanted stresses and cracks in our concrete infrastructures. This is partly due to the lack of understanding of the underlying mechanisms governing the drying shrinkage in cementitious materials. Inspired by the tremendous impact of atomistic simulations on materials science, we expect such innovative simulation techniques to hold a key to unlocking the enigmatic nature of drying shrinkage at the nanoscale. In this treatise, we first introduce basic physics concepts and atomistic simulation methods in detail. Afterward, we discuss the progress brought by atomistic simulations in understanding the drying shrinkage in cementitious materials and other nanoporous and nanolayered systems. This review also highlights important remaining fundamental questions and practical issues regarding drying shrinkage and delineates how atomistic simulations can help resolve them.

1. Introduction

The fact that Portland cement-based materials deform over their lifetime under the combined effect of chemical, mechanical, thermal, and hydric solicitations (and in particular shrink upon drying, which is known as 'drying shrinkage') has been known and studied for many

decades. However, despite this decades-long scrutiny, there is still significant interest in studying cement-based materials' drying shrinkage. This continued interest results from the combination of an unprecedented push for decarbonizing the cement industry and the emergence of innovative modeling methodologies, namely molecular (a.k.a atomistic) simulations, that make it possible to shed new light on an old

Abbreviations: ASTM, American Society for Testing and Materials; AFm, Calcium aluminate mono-sulphate hydrates; ASR, Alkali-silica reaction; BET, Brunauer–Emmett–Teller; BJH, Barrett, Joyner and Halenda; C₂S, Dicalcium silicate; C₃A, Tricalcium aluminate; C₃S, Tricalcium silicate; C₄AF, Ferrite; CBMC, Configurational bias Monte Carlo; C-(N)-A-S-H, Sodium-based calcium-alumino-silicate; CPU, Central processing unit; C-S-H, Calcium silicate hydrate; CTE, Coefficient of thermal expansion; DFT, Density Functional Theory; DLVO, Derjaguin, Landau, Verwey, Overbeek; ENS, Elastic neutron scattering; FEP, Free Energy Perturbation; GCMC, Grand Canonical Monte Carlo; HD, High-density; HG, High grafting; ¹H NMR, Proton nuclear magnetic resonance; IUPAC, International Union of Pure and Applied Chemistry; LD, Low-density; LG, Low grafting; MC, Monte Carlo; MD, Molecular dynamics; MRI, Magnetic resonance imaging; M-S-H, Magnesium silicate hydrates; NPT, Isothermal-isobaric ensemble; N₂H_{ad}PT, Grand isobaric or osmotic ensemble; NVE, Microcanonical ensemble; NVT, Canonical ensemble; PBC, Periodic boundary conditions; PDF, Pair distribution functions; PFCR, Proton field-cycling relaxometry; PMF, Potential of mean force; PN-TrAZ, Pellenq and Nicholson Force Field, transferable for adsorption in zeolites; QENS, Quasi-elastic neutron scattering; RDF, Radial distribution functions; RH, Relative sumple point charge; SRA, Shrinkage-reducing admixture; SSA, Specific surface area; TEM, Transmission electronic microscopy; TGA, Thermo-gravimetry analysis; TIP (TIP3P, TIP4P05, TIP5P), Transferable intermolecular potential (with 3, 4, 5 points...); XANES, X-ray absorption near edge structure; XCSH, Crosslinked C-S-H; XRD, X-ray diffraction; μVT, Grand canonical ensemble.

E-mail address: matthieu.vandamme@enpc.fr (M. Vandamme).

^{*} Corresponding author.

 $^{^{1}\,}$ These authors contributed equally to the manuscript.

problem. Indeed, decarbonizing the cement industry implies supplementary cementitious materials and the development of innovative binders [1]. For those latter, drying shrinkage is less well understood than for ordinary Portland-based cement while playing a pivotal role in their durability (see, e.g., the case of alkali-activated binders [2]). Concurrently, as mentioned, molecular simulations have been developed in the last few decades, which led to tremendous progress in the general materials science community. For instance, this progress accelerated materials innovation by enabling 'in-silico' rapid prototyping of new materials [3] and drug discovery [4]. This review aims to build on this opportunity and show what we have learned and will possibly learn with molecular simulations regarding the drying shrinkage of cement-based materials.

Drying shrinkage is one of the few types of shrinkage that cementbased materials exhibit. Non-exhaustively, other types of shrinkage include [5] thermal shrinkage, autogenous shrinkage, and carbonation shrinkage. The thermal shrinkage occurs due to the cooling down of the sample after its initial heating by the hydration reactions. The autogenous shrinkage is the macroscopic shrinkage of a load-free sample in sealed and isothermal conditions. It partly results from chemical shrinkage (i.e., Le Chatelier contraction) due to hydration reactions. The carbonation shrinkage represents the sample's long-term response to environmental carbon dioxide [6]. If we restrain shrinkage (e.g., for a hyperstatic structure or because of internal restrain by the reinforcement), shrinkage will induce stresses that may cause cracking. The cracks, in general, are known to facilitate the ingress of chemical agents into the concrete (e.g., [7]) and impair the containment capacity of concrete barriers (e.g., in infrastructures for energy production such as dams and nuclear facilities [8]). By drying shrinkage, we refer to the shrinkage part due to the moisture loss. Even for an unrestrained sample, drying can induce stresses: indeed, drying occurs through the sample's surface, which will be drier than its core and will hence shrink more. Consequently, in such a case, upon drying, one expects tensile stresses at the surface of a sample and compressive stresses in its core, which can lead to surface cracks.

In 1900, when Le Chatelier identified the now called `Le Chatelier contraction' (or chemical shrinkage), which states that the volume of solids decreases during the hydration, the fact that the apparent volume of cement-based materials evolves over time was already well known [9]. Cement and concrete scientists have studied volume variations of cement-based materials for more than a century. The specific fact that cement-based materials shrink upon drying dates back at least to the 1930s with the works of Freyssinet [10] and Carlson [11].

The measurement of macroscopic drying shrinkage usually consists of placing a load-free sample in an atmosphere at various relative humidities and measuring the variation of its length. The specimen may be cement paste (e.g., [12]), mortar (like in the ASTM C-596 standard), or concrete (e.g., [11]). The sample's mass is often measured to obtain the specimen's water content, making it possible to display shrinkage strains versus relative humidity and versus water content. The relation between water content and relative humidity is called a water sorption isotherm. Fig. 1 displays a typical drying shrinkage experiment, in which the authors also measured water content. This experiment consists of a cycle of first drying and re-imbibition. One observes that drying induces shrinkage and that imbibition induces swelling. The shrinkage observed during the first drying is not fully recoverable as the first drying is partly irreversible, while subsequent drying cycles are known to be mostly reversible.

In the first section of this review, we introduce various topics: the multiscale porosity and microstructure of cement-based materials and the various types of water they contain, sorption theory, the physics of drying shrinkage, and the complexity of drying shrinkage and sorption experiments. Section 2 is devoted to introducing molecular simulation methods and discussing their relevance in length and time scales. In Section 3, we review what we have learned from molecular simulations regarding cement-based materials' drying shrinkage. In Section 4, by reviewing molecular simulation studies performed on other layered materials, we discuss what else could be learned from molecular simulations regarding drying shrinkage of cement-based materials. Section 5 is devoted to identifying molecular simulations' limitations and

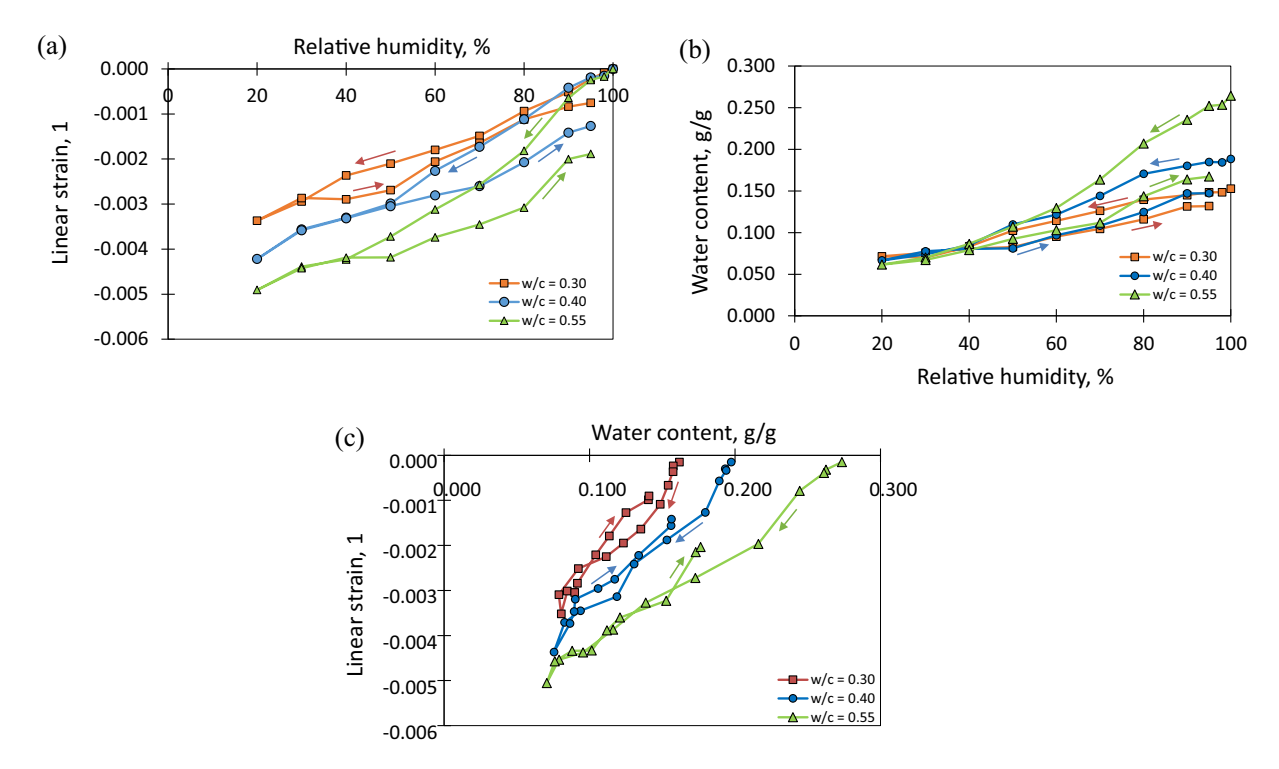


Fig. 1. Typical drying shrinkage experiment of cement pastes at different water-to-cement ratios w/c along with measured water content. (a-c) Drying shrinkage and (b) water content over a cycle of drying and imbibition. Drying shrinkage is displayed versus (a) relative humidity and (c) water content. The figures are adapted from [13]. Arrows indicate in which direction the experiment evolved with time.

perspectives to study drying shrinkage.

1.1. Multiscale porosity and microstructure in cement-based materials

The pore structure of cement-based materials is known to significantly impact several of their properties (e.g., permeability, mechanical properties, durability), among which their propensity to drying shrinkage. The total porosity depends on both the water-to-cement ratio w/c and the hydration degree, ranging for a mature ordinary Portland cement paste from about 27% at w/c=0.3 to about 45% at w/c=0.6 [14]. The porosity of cement-based materials is multiscale: the pores' size spans more than six orders of magnitude, from the millimeter scale down to the nanometer scale [15]. Because of the very small size of the smallest pores, the specific surface area of ordinary Portland cement pastes is high, namely on the order of $80-280 \, \mathrm{m}^2.\mathrm{g}^{-1}$ [16]. Because of this high value, surface effects impact the cement-based materials' shrinkage (see Section 1.4).

The pore structure of cement-based materials is complex and challenging to analyze, as it is, for instance, impacted by drying [17,16,12] and as the techniques used to characterize this pore structure (e.g., small-angle neutron scattering (SANS), sorption measurements, proton nuclear magnetic resonance (¹H NMR)...) require significant interpretation. One feature supported by various experiments is that the nanoscale porosity of calcium silicate hydrates (C-S-H) is multimodal: from SANS experiments, Allen et al. [17] identify nearly spherical pores with diameters of 5 and 12 nm; based on the interpretation of water sorption isotherms Jennings [18] proposes three characteristic pore sizes for C-S-H of about 1 nm, 1–3 nm, and 3–12 nm; from ¹H NMR data, Muller et al. [19] identify a bimodal distribution of the porosity of C-S-H.

As a consequence of the pore space's complexity, various conventions are used in the literature to classify the different types of porosity. In this review, we will use a convention based on pore size:

- Air voids entrapped in the material can range from a few dozen micrometers up to as much as 3 mm [15]. Entrained air voids, i.e., air voids trapped in the cement paste on purpose (e.g., to increase the resistance to freeze-thaw), typically range from 50 μm to 200 μm [15].
- Capillary pores (or capillary voids) are much smaller than air voids and range from about 8 nm up to 1 μ m or even 3 to 5 μ m in an early-age cement paste with a high water-to-cement ratio [15]. Their denomination comes from the fact that, in those pores, capillary effects (see Section 1.4) become significant. C-S-H does not contain all capillary porosity in the cement paste [19]. A mature paste's capillary porosity increases with the water-to-cement ratio. For instance, according to the Powers-Brownyard model [20], it is equal to 0 at w/c=0.3, and about 30% at w/c=0.6.
- We call *gel pores* the pores that range from about 0.5 nm to about 8 nm. C-S-H contains most of them.
- We call *interlayer spaces* the pores that are smaller than about 0.5 nm. Like gel pores, C-S-H contains most of the interlayer spaces. However, interlayer spaces are also present in AFm phases (e.g., monosulfoaluminate) and microporous zeolitic cavities in ettringite. These interlayer spaces can exchange water with their surroundings, such that the hydration state of monosulfoaluminate and ettringite varies with relative humidity and temperature [21]. Note that, for C-S-H, the limit size between gel pores and interlayer spaces is somewhat subjective. Different authors with different backgrounds or other investigation techniques may consider a different limit size. For instance, Jennings et al. [22], based on an analysis of water sorption isotherms, propose that the limit between interlayer spaces and gel pores is around 2 nm. Here we consider a limit size of about 0.5 nm because such interlayer space can only contain up to about two layers of adsorbed water. The dynamics of water under such confinement are known to differ significantly from the water dynamics in larger pores (e.g., gel pores) [23,24]. Some of the interlayer spaces can be

envisioned as well delimited by somewhat parallel C-S-H layers. We can also refer to the pore size (i.e., the distance between the C-S-H layers) and the interlayer spacing [22]. We can readily extend the notion of interlayer spacing to gel pores for gel pores that are delimited by parallel C-S-H layers. Note also that, in such subnanometric pores, defining a pore size is ambiguous for various reasons. These include atomistic roughness of the surface [25], fluctuation of the position of the atoms of the wall, existence of various definitions of the pore size (e.g., should one place the pore wall at the center of the outermost atoms of the skeleton, or take into account the Van der Waals radius of those atoms?).

The Powers-Brownyard model considers the hydration products' porosity constant and equal to 0.28 [20] for what concerns the solid constituents in ordinary Portland cement-based materials. Independent experimental techniques point to the formation of two types of C-S-H during hydration, generally called inner and outer product (e.g., in Daimon et al. [26] or Richardson [27]) or high-density (HD) and low-density (LD) C-S-H (e.g., Constantinides and Ulm [28]), respectively. Indeed, time-resolved SANS [29] and nitrogen sorption isotherms [30] separately capture the formation of two morphologies with different surface areas. Statistical nanoindentation experiments identify two distinct C-S-H phases from a mechanistic perspective, namely low-density and high-density, with identical composition but mechanically different signatures [28,31].

Several models have been proposed for the C-S-H's microstructure that mainly align with two seminal works: a sheet structure for Feldman and Sereda [32] and a globular/colloidal model for Jennings [18,33]. Transmission electron microscopy (TEM) images indicate a fine-textured inner product and a fibrillar/foil-like outer product [27,34]. A sheet-like structure is also more consistent with C-S-H growth mechanisms proposed at low supersaturation [35]. In contrast, a detailed analysis of SANS [36] is consistent with a microstructure of C-S-H obtained by a diffusion-controlled aggregation of C-S-H particles. Nanoindentation [31] and sorption [18] experiments independently support a unique nanogranular origin for low-density and high-density C-S-H. The two models for C-S-H may not be antinomic, as one can envision a microstructure made of particles-like regions constituted of sheet-like structure [22]. We can also explain the observed duality between low-density and high-density C-S-H by considering the formation of the C-S-H gel as a diffusion-controlled aggregation process [36] or the growth of twodimensional C-S-H sheets or ribbons with inherent stacking defects [37]. When measuring such particles' size, a characteristic dimension of about 5 nm is obtained from an analysis of SANS data [36]. Several authors recently obtained a characteristic length of about 4-5 nm for the size of C-S-H apparent crystalline domains perpendicular to the C-S-H layers from the analysis of the peak broadening of X-ray diffraction (XRD) data [38,39].

1.2. Various types of water in the cement paste and their physical attributes

The classification of water types in hardened cement paste is intimately related to the classification of its porosity. To be consistent with the porosity conventions introduced in Section 1.1, we categorize water into four types, as follows:

- Interlayer water (also known as nanoconfined water, structural water, and hindered adsorbed water) designates those water molecules adsorbed in the C-S-H porosity with an effective slit pore width of 0.5 nm and smaller. The water molecules in such nanoconfined geometries are strongly affected by the surface, and their chemophysical properties deviate from those of bulk. Interlayer water molecules play a critical role in adjusting the basal spacing distance in C-S-H.

- Interfacial water (also known as surface water) represents the layers of water molecules adsorbed on the surface of C-S-H layers/particles (corresponding to nanopores, capillary porosity, and air voids) and other hydrophilic phases. The thickness of the adsorbed water nanofilms depends on both the temperature and relative humidity [40,41]; see Section 4.3 for more details. The interfacial water nanofilm thickness reaches ~0.75–1.0 nm at room temperature and 90% relative humidity [42], equivalent to the size of three to four water molecules. Understanding the physics of interfacial water layers is critical in portraying a chemo-mechanical picture of saturated and unsaturated hardened cement paste.
- Gel water (also known as constrained water) corresponds to a portion of the water in the C-S-H gel's nanoporosity, excluding the interfacial water layers. The physical properties of gel water are still affected by the nanoconfinement and surface effect and differ from those in bulk.
- <u>Capillary water</u> (also known as free water) is the water in capillary porosity, excluding the interfacial water. The properties of free water are akin to those in bulk.

The above classification lends itself naturally when juxtaposing the results from quasi-elastic neutron scattering (QENS) and proton field-cycling relaxometry (PFCR) experiments with molecular dynamics (MD) simulation. In what follows, we provide a historical account of modern progress in understanding and characterizing water types in the cement paste and their physical properties in the twenty-first century.

While characterizing water in hydrating cement paste using QENS, Thomas et al. [43] distinguished three water types. Their classification includes chemically bound (structural), constrained, and free water types, which correspond to our interlayer, interfacial/gel, and capillary water, respectively. In this classification, the chemically bound water includes structural water and hydroxyl groups as they are indistinguishable in the scattering data. By applying a dynamical model to the QENS spectrum collected from hydrating tricalcium silicate (C₃S) pastes, Fratini et al. [23,24] distinguished between glassy water dynamics in the gel pores and immobile water in the interlayer spacing of C-S-H. In the meantime, Fratini et al. [44] studied the relaxation time τ_r of water in hydrating C₃S paste. They found that the relaxation time of water in the early-age cement paste is twice that of bulk water (~5 ps). They also showed that the water relaxation time increases gradually with increasing hydration degrees reaching 40 ps. Later on, they performed the same measurements on pastes of different clinker phases and showed that the relaxation time is longer in $C_4AF > C_3A > C_3S > C_2S$ (where C₄AF is ferrite, C₃A is tricalcium aluminate, C₃S is tricalcium silicate, C₂S is dicalcium silicate) beyond the first hydration day. They attributed this difference to the difference in hydration kinetics between the phases and the intrinsic porosity attributes of the resultant hydration product [45]. By analyzing the elastic neutron scattering spectra with a simplified analytical model, Fratini et al. [46] found that the diffusive dynamics of water in the hydrating cement paste decays from bulk-like to surface-like behavior with a self-diffusion constant an order of magnitude smaller than the bulk water, decreasing from 4×10^{-9} m²/s to $4 \times$ $10^{-10}\ \text{m}^2\text{/s}$. These findings are based on the measured characteristic time of \sim 40-50 ps at the later stages of hydration (2 days) and an average jump distance of 3 Å, i.e., roughly the size of a water molecule. Meanwhile, water's self-diffusion coefficient in the synthetic C-S-H gel was measured to be $\sim 1 \times 10^{-10}$ m²/s [47]. Interestingly, Li et al. [47] showed that the diffusion-coefficient-to-temperature ratio in C-S-H gel exhibits a temperature-dependent behavior at T < 240 K, which violates the Stokes-Einstein relation ($D/T = (k_B/6)\pi\eta R$). Such observation is the signature of dynamical cross-over (high-density to low-density phase transition in confined water in gel pores) observed by Ridi et al. [48] in low-temperature differential scanning calorimetry.

Nuclear magnetic resonance (NMR) relaxation studies have provided a wealth of information on the pore network structure and water dynamics in hydrating cement paste. In these studies, spin-lattice (T_1) and spin-spin (T_2) relaxation times are measured via the PFCR technique and

interpreted in the light of a two-dimensional surface diffusion model of spin relaxation. This technique provides direct access to the correlation time for molecular jumps τ_m and surface residence time τ_s of water molecules that describes the exchange between the interfacial and gel water. By analyzing T1 dispersion data, Barberon et al. [49] measured cement paste's surface area in terms of hydration degree and time. They also found that τ_m depends on the hydration degree, reaching 1.3 ns after 12 h. Later, Mcdonald et al. [50] performed T₁-T₂ and T₂-T₂ 2D nuclear spin relaxation correlation measurements and observed water exchange evidence between gel and capillary pores. After a careful analysis of 2D NMR T2-T2 exchange experiments, Monteilhet et al. [51] calculated the diffusion coefficient of interfacial water to be $\sim 2.3 \times 10^{-11} \text{ m}^2/\text{s}$ considering a mean hopping distance of 3 $\mbox{\normalfont\AA}$ over a relaxation time of ~ 1 ns. They also estimated the diffusion coefficient of gel water, $5\times 10^{-10}\,$ m^2/s , from a characteristic length of 4 µm exchange between the gel and capillary porosity and associated relaxation time of 5 ms. Interestingly, McDonald et al. [52] found that τ_m is not strongly affected by the cement type, remaining around 1 ns. However, surface chemistry strongly influences τ_s , decreasing it from 18.5 µs in white cement-based materials to 0.1 µs in ordinary Portland cement-based materials.

1.3. Basics of adsorption

The International Union of Pure and Applied Chemistry (IUPAC) formally defines the adsorption phenomenon as an increase of concentration of a gaseous (or dissolved) substance at the interface of a condensed (solid) phase due to surface forces. The surface forces originate from the inter-atomic interactions between the adsorbate (adsorbed molecules) and the adsorbent (adsorbing solid). The adsorption phenomenon becomes significant when these interactions are strong enough so that the decrease of energy of a molecule between the gas and the adsorbate is significant. As we shall detail formally later, 'significant' means with respect to the bulk Gibbs free enthalpy (a.k.a. chemical potential μ) and to the thermal agitation (whose energy per atomistic degree of freedom is on the order of k_BT). Consequently, the adsorption phenomenon usually depends on two state parameters of the fluid, namely chemical potential μ and temperature T (or equivalently relative humidity *RH* and *T* in the particular case of water vapor adsorption). The most common characterization of adsorption is the adsorption isotherm, which characterizes the amount adsorbed at a constant temperature as a function of the chemical potential or equivalent state parameter (partial vapor pressure, RH). The particular case of water in cement-based materials is more complex because adsorption exhibits hysteresis and couplings with deformation, and therefore its thermodynamics should include strain (or stress) and loading history.

The adsorption phenomenon can be characterized experimentally by several techniques. Standard measurement techniques are the gravimetric or volumetric methods, in which one measures the adsorbed amount (through mass or volume) at imposed chemical potential μ . There exist also the manometric techniques, in which one measures the chemical potential (through pressure) corresponding to given adsorbed amounts. Application of the usual methods to water adsorption in cement-based materials requires very long equilibration, during which other physical phenomena can occur alongside adsorption (see Section 1.5). Alternatively, other, less usual experimental techniques can also probe the adsorbate's presence directly in situ. Such methods are generally system-dependent and, in the case of water adsorption in cement-based materials, let us mention X-ray and neutron radiography and tomography [53,54], nuclear magnetic resonance techniques (NMR, magnetic resonance imaging (MRI)) [55], and neutron scattering techniques (QENS, SANS) [56,57]. These techniques offer the possibility to measure the spatial distribution and time evolution of water content and distinguish between the different water types (see Section 1.2). Such information provides a more detailed picture of water adsorption in cement-based materials, which alleviates the need for water content homogeneity throughout a sample.

One can view *physical* adsorption as an exothermic process, with the heat of reaction characterizing the coupling between energy and absorbed amount. This coupling is formally quantified by the isosteric heat of adsorption q_{SD} defined as the heat released per molecule adsorbed at a given temperature T, and (reservoir) pressure P_{res} : $q_{st} = h_v - h_a$, with the molar incremental enthalpy $h = \begin{bmatrix} \frac{\partial H}{\partial N} \end{bmatrix}_{T,P_{res}}$ (h_a and h_v refer to the adsorbed and vapor phases, respectively). Alternatively, h can also be related to the change of chemical potential with temperature, thanks to a Maxwell relation of the Gibbs free enthalpy: $h = \begin{bmatrix} \frac{\partial (\mu/T)}{\partial (1/T)} \end{bmatrix}_{N,P_{res}}$. Experimentalists generally measure the heat of adsorption using the calorimetry technique [20]. It is essential to understand how the adsorption isotherm evolves with temperature, offering an alternative route of measurement [58].

isotherm in cement paste. As we shall explain hereafter, the relative humidity axis can also be interpreted as an axis of pore size. Water adsorption and desorption vary over the full range of relative humidity, and there is no sharp change in water content that would correspond to particular pore size. One can distinguish the domain RH < 40% corresponding to micro-pores less than 2 nm large, and the range of RH > 40% corresponding to mesopores or macropores larger than 2 nm. Accordingly, the adsorption isotherm encompasses different water types (see Section 1.2), and various theoretical descriptions must be combined to interpret it fully. In practical applications, the adsorption and desorption are incomplete, i.e., they do not cover the full range of relative humidity. The corresponding scanning isotherms remain inside the area delimited by the entire adsorption-desorption cycle, and the hysteresis is truncated. The origin of the hysteresis is debated [59], and no clear consensus has emerged so far. Possible hysteresis sources are the ink bottle effect, the surface effects for the capillary process, the incomplete equilibration, the accessibility and binding to adsorption sites, and the coupling with deformation. Most probably, no single origin can explain the hysteresis in cement-based materials over the full range of RH.

Since adsorption is at the crossroads of physics and chemistry, there are different ways to formalize it from a theoretical perspective. Here, we adopt a description based on statistical physics and thermodynamics, which is the most common for the molecular simulation community. Consider the system made of the adsorbent and the adsorbate in contact with the gaseous reservoir. As a consequence of the thermal and osmotic equilibrium with the reservoir, the amount adsorbed is distributed following Boltzmann statistics in the Grand Canonical ensemble: $p(N) = \frac{1}{N} \left(\frac{1}{N} \right)^{N}$

$$\frac{1}{Z_{GC}}\sum_{i \text{ with } N_i=N} exp\left(\frac{-E_i-\mu N}{k_BT}\right)$$
. $Z_{GC}=\sum_{i} exp\left(\frac{-E_i-\mu N_i}{k_BT}\right)$ is the grand canonical

partition function and E_i and N_i are the energy and number of adsorbate molecules of the micro-state i. Boltzmann statistics provide a general way to understand the adsorption phenomenon: in the 0 K limit, the system will occupy most favorable adsorption configurations with energy $E_i < \mu N_i$, and none above. The occupation factor is no more discontinuous at finite temperature, but there is still a transition for configurations with $E_i \sim \mu N_i$. The rigorous estimation of the average adsorbed amount requires integrating over the entire phase space, but only a small fraction of the phase space contributes to non-negligible Boltzmann probabilities. Molecular simulation techniques provide estimates by sampling those regions only. One eventually recovers the thermodynamic relation: $N = -\frac{\partial A}{\partial \mu}\Big|_T$, with $A = -k_BT \ln{(Z_{GC})}$. In the

thermodynamic limit, Λ is identified as the grand potential $\Lambda = E - TS - \mu N$, which is the thermodynamic potential minimum for a system in thermal and osmotic equilibrium. Therefore, a thermodynamic approach to adsorption consists of evaluating how the grand potential depends on the chemical potential. The thermodynamic and statistical physics routes are equivalent, but the former is more adapted to continuum approaches, and the latter to molecular techniques. As we shall discuss in Section 2, molecular simulations of adsorption, based either on Molecular Dynamics (MD) or Monte Carlo (MC) simulations, aim at sampling the phase space according to the Boltzmann statistics. In contrast, macroscopic analyses are based on the thermodynamic description.

How this formal description translates in practice depends on how the energy evolves with adsorption. The most simple adsorption model (Langmuir) assumes identical independent adsorption sites, i.e., $E_i =$ N_iU_{ads} with U_{ads} characteristic energy. In that case, one easily integrates the Boltzmann statistic and obtains the Langmuir isotherm [60]: $\frac{N}{N_{sites}}$ $\frac{P}{P+P_0(T)}$ where the vapor phase is assumed to be an ideal gas (i.e., its chemical potential is $\mu(P,T) = \mu_0(T) + k_B T \ln{(P)}$ and the characteristic pressure is $P_0 = exp\left(\frac{U_{ods} - \mu_0(T)}{k_BT}\right)$. Another well-known adsorption model is the BET model [61], which is also easily derived by allowing multiple adsorbed layers. Site adsorption can represent adsorption on surfaces or in sub-nanometric pores (intralayer pores, the surface of gel pores). Still, the filling process in larger pores falls in the domain of capillary processes. The capillary description assumes that the adsorbate can be described as an under-saturated liquid whose stability is ensured by surface energies. The pressure of this liquid must be decreased (capillary pressure) to satisfy the osmotic equilibrium with the vapor phase $(\mu_{\nu}(RH,T) = \mu_{sat}(T) + k_BT \ln (RH)$ with $\mu_{sat}(T)$ the chemical potential at saturation). Assuming an incompressible liquid of number density ρ_l and integrating the Gibbs-Duhem equation at a constant temperature, one

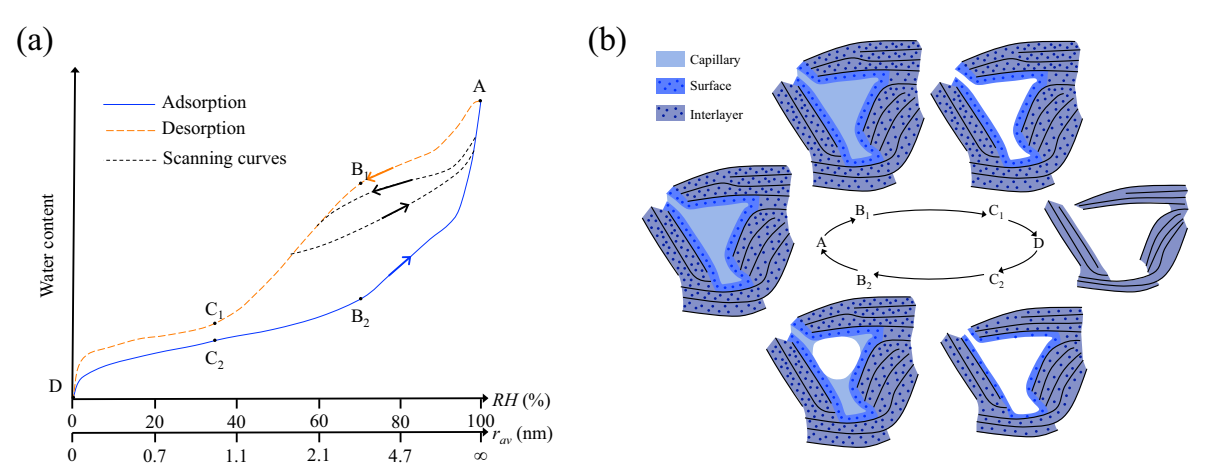


Fig. 2. (a) Schematic adsorption isotherm of water in cement-based materials. (b) Hand-made sketch of the adsorption/desorption process at the nanoscale. Configurations A and B1 are assumed to differ in larger pores only (not displayed).

gets the change of chemical potential due to a drop of pressure in the liquid phase: $\mu_l - \mu_{sat}(T) = \frac{P_l - P_{sat}(T)}{\rho_l}$. Equality of the chemical potentials of the liquid and vapor phases, $\mu_l = \mu_{\nu}$ leads to a pressure drop that increases as the relative humidity RH decreases:

$$P_l - P_{sat}(T) = \rho_l k_B T ln(RH) \tag{1}$$

In this equation, like in all equations in this manuscript, the relative humidity RH is dimensionless, even though we usually give its magnitude in percents: as an example, relative humidity of 90% corresponds to RH = 0.90.

The undersaturated liquid is metastable, but surface energies can ensure its stability if the liquid is the wetting phase and the Laplace pressure across the liquid-gas interface compensates the capillary pressure.

$$P_{v} - P_{l} = \frac{2\gamma}{r_{vir}} \tag{2}$$

with γ the liquid-vapor surface tension and r_{av} the average radius of curvature of the liquid-gas interface. Combined with additional assumptions on the pore geometries and contact angle, r_{av} can be related to the pore radius. For instance, $r_{av} = r_{pore}$ for the desorption from a cylindrical pore with perfect liquid wetting. The vapor and saturation pressures are usually on the order of the atmospheric pressure or less, thus of much smaller magnitude than the capillary pressure. Neglecting P_v and $P_{sat}(T)$, one eventually obtains the Kelvin equation relating the relative humidity RH to r_{av} :

$$ln(RH) = \frac{-2\gamma}{\rho_i k_B T r_{av}} \tag{3}$$

The Kelvin equation, combined with a pore size distribution, predicts the capillary filling or emptying of porous solids upon RH change. In this framework, a classical interpretation of the adsorption hysteresis is that desorption is associated with the formation of a hemispherical meniscus ($r_{av}=r_{pore}$ for perfect wetting). In contrast, capillary condensation is related to forming a cylindrical liquid film on the channel wall ($r_{av}=2r_{pore}$ for perfect wetting). Kelvin equation is applicable provided that the pores are large enough to ensure that the liquid's usual thermodynamics is valid. Table 1 provides estimates of the correspondence between the radius r_{av} and the RH for water at ambient temperature (T=300K). Kelvin equation breaks down when the pores' size approaches the nanometer, i.e., for RH below 40%.

The Kelvin equation predicts the filling of macro-pores, i.e., of pores in which surface and micro-pore adsorption are negligible. A widely used extension to mesoporous media is the BJH analysis [62] (where BJH stands for its authors Barrett, Joyner and Halenda), which superposes multi-layer surface adsorption and capillary filling. The BJH method assumes an idealized porous structure made of independent cylindrical pores with perfect liquid wetting. Therefore, the Kelvin equation application provides the difference between the largest por radius filled with liquid and the adsorbed film thickness: $r_{av} = r_{pore} - t$ (for desorption). The BJH analysis combines the Kelvin equation with a model of surface adsorption to predict the adsorption isotherm. Several models are used in the cement science community to describe the thickness of the water adsorbed layer on the pore wall, mainly the models of Hagymassy et al. [41] and Badmann et al. [42].

When the pore size approaches the nanometer scale, adsorbate molecules start to interact with the solid on both sides of the pores, and the BJH analysis is no more valid. The adsorbate molecules' energy becomes sensitive to the pore size, which gives rise to a mechanical

pressure of the fluid different from the ordinary 'bulk' pressure (i.e., the bulk fluid pressure at the same chemical potential and temperature). The difference is called the disjoining pressure and was introduced initially by Derjaguin [63]. The thermodynamic equilibrium corresponds to a liquid film thickness that balances the disjoining pressure and the capillary pressure. Derjaguin's model extends BJH analysis to nanometer-large pores, and one recovers the Kelvin equation when the disjoining pressure vanishes [64]. In Derjaguin's model, the adsorption hysteresis is interpreted as a difference in thermodynamic stability between adsorption and desorption, consistent with the BJH model. The adsorption follows the metastable branch, and the condensation occurs at the point of instability, whereas desorption follows the stable branch. A difficulty, though, for practical application, is to estimate the disjoining pressure. Some analytical expressions were proposed [65,64] but remain limited to specific situations (geometry, interactions) that are calibrated with data for each adsorbate-adsorbent system.

Kelvin equation, BJH analysis, and Derjaguin's model are thermodynamic approaches that distinguish the liquid, vapor, and solid phases separated by infinitesimal interfaces and model a liquid-vapor phase transition at the capillary condensation. Yet, as pore size approaches a few molecule diameters, the phase transition phenomena are strongly impacted. In particular, the critical temperature is known to decrease with the pore size. For a given temperature, there is a pore size below which capillary condensation cannot be observed anymore [66,67]. In that context, a thermodynamic representation based on liquid and vapor phases is no more valid, and molecular simulation offers an exciting alternative to thermodynamic models (see Section 2). Molecular modeling relies on inter-atomic interactions only and does not suffer from the limits of continuum approaches. Yet, it remains limited to very small system sizes (a few nanometers). Following Neimark and Ravikovitch [64], who studied adsorption in silicates with well-defined pore sizes, Table 2 lists the above approaches' applicability range. The range is given in pore size and equivalent RH at 300 K, assuming that the Kelvin equation is applicable. It is clear that a single technique cannot predict a complete description of the adsorption isotherm of water in cement-based materials, and combining molecular and continuum approaches is necessary.

The schematic isotherm of Fig. 3 can illustrate a general description of adsorption hysteresis. This isotherm depicts the case of a single pore. For reversible adsorption, each chemical potential corresponds to a single amount adsorbed, and the isotherm increases monotonously. Hysteresis corresponds to the co-existence of several amounts adsorbed at the same chemical potential. The decreasing branches are thermodynamically unstable, and only the increasing branches can be observed. The thermodynamic equilibrium corresponds to the minimum of the grand potential. The chemical potential at the point of transition

from one increasing branch to the other must satisfy Maxwell's rule: $\footnote{\colored}$

 $\mu dN = 0$, i.e., the dashed areas in Fig. 3 are equal. Hysteresis arises because the system does not follow the most stable branch during

Table 2The domain of applicability of the different approaches to model adsorption.

Approach	Kelvin equation	ВЈН	Derjaguin	Molecular simulation
Pore size	>50 nm	>10-20 nm	>4 nm	any
RH (at 300 K)	>0.98	>0.90-0.95	>0.77	any

Table 1 Correspondence between the radius r_{av} (cylindrical pores) and the relative humidity *RH* according to Kelvin equation for water at ambient temperature.

			_						
RH (%)	1	10	20	40	60	80	90	99	99.9
r_{av} (nm)	0.228	0.456	0.653	1.15	2.06	4.71	9.97	104	1050

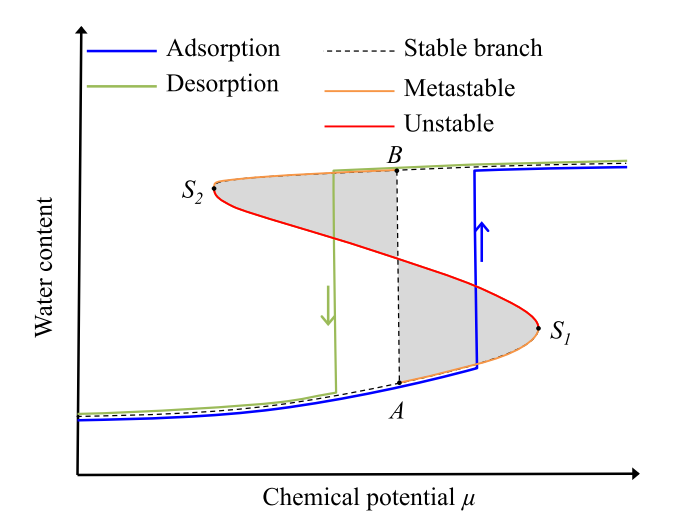


Fig. 3. Schematic isotherm of a single pore, which exhibits the different domains of stability.

adsorption or desorption but remains in a metastable configuration. For instance, in the BJH analysis, only the desorption branch is considered to follow the stable branch (formation of a hemispherical meniscus in a cylindrical pore) and can be used to derive the pore size distribution. Adsorption may proceed along the metastable branch. For instance, a cylindrical meniscus' formation would correspond to adsorption following the metastable branch until the spinodal point S_1 . The domain bounded by the two spinodal points S_1 and S_2 gives the maximum hysteresis. The type of hysteresis observed in cement-based materials exhibits no sharp change in adsorbed amount, suggesting the superposition of a wide variety of pore sizes. Why adsorption or desorption follows their metastable branches can have many origins. Regarding water in cement-based materials, let us mention the ink-bottle effect (a.k.a. poreblocking), the change of contact angle between adsorption and desorption, the difference in spatial pore connectivity during adsorption and desorption, and the coupling between adsorption and deformation [68].

So far, our description of adsorption disregarded the couplings between adsorption and deformation. Yet, capillary and disjoining pressures are known to reach hundreds of MPa in magnitude, generating significant adsorbent deformations. In turn, a deformation of the adsorbent can affect the adsorption energy and thus change the amount adsorbed. This observation calls for a thermodynamic description of adsorption that is not limited to RH and extends to the porous medium's strain. Drying shrinkage of cement-based materials is an illustration of these couplings and is the focus of the next section.

1.4. Physics of drying shrinkage

Upon drying, cement-based materials shrink as a consequence of the

release of water from their pore space. This shrinkage is due to the variation of the in-pore water's mechanical action on the solid skeleton [69–76]. Despite the apparent simplicity of the relationship between shrinkage and water content displayed in Fig. 1c, how the in-pore fluid acts mechanically on the solid skeleton is complex, as various physical processes are involved. For a thorough review of adsorption-induced deformations, we refer to [77]. Here we provide an overview of the physical processes at stake. They are (see Fig. 4):

• Capillary effects: Upon drying, the in-pore solution is gradually replaced by air, such that the meniscus between air and the pore solution recedes into the pore space, as explained in detail in Section 1.4. Because of the surface tension of this meniscus and the contact angle between this meniscus and the surface of the pore, the meniscus is curved and, to satisfy Laplace law (Eq. (2)), the pressure of the pore solution must be lower than the pressure of air (which is equal to the atmospheric pressure). This difference of pressure (which is called capillary pressure) is all the more important that the meniscus is curved. During drying, the meniscus recedes into smaller and smaller pores. It becomes more and more curved, such that the capillary pressure increases and the pore solution becomes more and more in depression, and hence "pulls" on the pore walls, leading to shrinkage.

During the drying, the remaining pore solution is in so much tension because of capillary effects that the liquid phase becomes unstable and cavitates. At room temperature, cavitation occurs at a relative humidity of about 30% [78], which corresponds to a tension of about 150 MPa in the liquid capillary water. Once cavitation has occurred, the system contains no more capillary water (and hence is not subjected to capillary effects anymore), such that all remaining water is adsorbed at the surface of the desaturated pores or in the interlayer space.

• Surface adsorption and Bangham effect: Even if a pore has been desaturated, its surface is still covered by a layer of adsorbed water, whose thickness t is on the order of the nanometer but depends on temperature and the relative humidity (i.e., the drier the air, the smaller the thickness of the adsorbed layer of water). This adsorption lowers the surface free energy γ of the pore surface, according to the so-called Gibbs isotherm [79]: $d\gamma = -\Gamma(\mu)d\mu$, where Γ is the amount of water adsorbed per unit surface or pore wall and μ the chemical potential of the water. Assuming that the number density of the water in the adsorbed layer is the number density ρ_1 of the liquid considered incompressible, this Gibbs isotherm can be rewritten as a function of the adsorbed thickness t as $d\gamma = -\rho_l t(\mu) d\mu$. Phenomenologically, Bangham and his co-workers (see Bangham and Razouk [80] and references therein) showed that the expansion $\Delta \varepsilon$ of charcoal is proportional to the lowering of the surface free energy (which is now called the Bangham effect), i.e.:

$$\Delta\varepsilon\propto\Delta\gamma = -\rho_l \int_{-\infty}^{\mu} t(\mu)d\mu \tag{4}$$

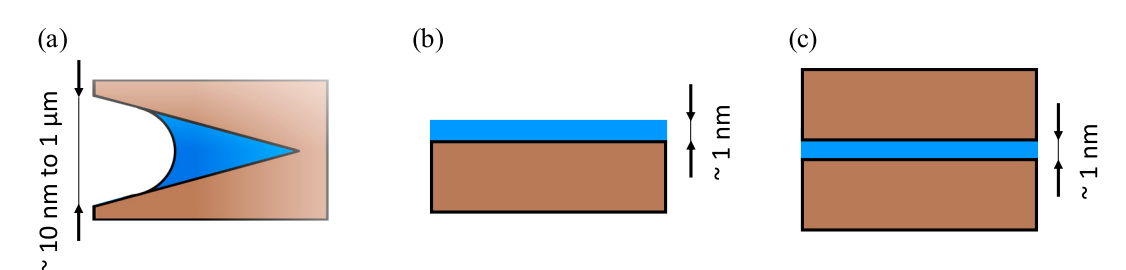


Fig. 4. Various physical processes through which water can deform a porous solid: (a) capillary effects, (b) Bangham-type surface effects, (c) disjoining pressure effects. Water is shown in blue, and the solid skeleton in brown. (For interpretation of the references to colour in this figure legend, the reader is referred to the web version of this article.)

Upon drying, the thickness of the adsorbed layer decreases with a decreasing relative humidity, which increases the pore surfaces' free energy and hence induces a contraction. Several models exist to describe the thickness t of the adsorbed layer of water, mainly the models of Hagymassy et al. [41] and Badmann et al. [42]. When comparing surface adsorption effects with capillary effects, one expects capillary effects to prevail at high relative humidity (i.e., larger than about 50%) and surface adsorption effects to prevail at low relative humidity levels (i.e., lower than about 50%) [81]. Note that, strictly speaking, deformations are due to variations of the surface stress and not of the surface free energy. The so-called Shuttleworth relation links surface stress and surface free energy [82]. Bangham's relation (4) is only approximate, but Gor and Bernstein [83] showed that it is applicable in most cases.

• Disjoining pressure effects: Disjoining pressure effects prevail when water is adsorbed between two solid surfaces separated by a distance on the nanometer's order. Hence, they are significant in the interlayer space. As explained in Section 1.3, because of the confinement, the fluid's thermodynamic pressure (i.e., the pressure in a bulk reservoir that contains fluid at the same chemical potential) differs from its mechanical pressure. This pressure difference is called disjoining pressure [84]. At a given temperature and chemical potential of the water, the relation between disjoining pressure and the interlayer spacing is called a disjoining pressure isotherm. The disjoining pressure is a non-monotonic function of the interlayer spacing, which oscillates between a positive few hundred MPa and a negative few hundred MPa. When the pore size becomes larger than 1 to 2 nm, confinement becomes sufficiently low, such that Eq. (1) gives the difference between mechanical and thermodynamic pressure of the liquid. In such sufficiently large pores, the disjoining pressure converges toward the capillary pressure.

On top of those effects, one should also note that, since the pore solution contains ions, some osmotic pressure effects (related to the heterogeneity of ion concentration in the system) can occur. Disjoining pressure, in particular, includes osmotic effects.

Because of the complexity of the shrinkage and sorption experiments in cement-based materials (as will be discussed in the next section) and the complexity of the materials themselves, disentangling the contributions of those various physical processes can be very challenging. In this respect, simulations to model each of those processes independently can prove beneficial. Also, surface adsorption effects and disjoining pressure effects are, by nature, nanometer-scale phenomena that involve intermolecular interactions. Hence, employing molecular simulations to study those phenomena is advantageous.

1.5. The complexity of the drying shrinkage and adsorption experiments

As already explained in the introduction, the measurement of macroscopic drying shrinkage usually consists of placing a load-free sample in an atmosphere at various relative humidities and measuring the variation of its length. The relative humidity can, for instance, be controlled in desiccators containing salt solutions (e.g., [12]), saturated salt solutions (e.g., [85]), or in chambers with active control of temperature and relative humidity (e.g., [32,86]). Fig. 1a displays a typical drying shrinkage experiment. When displaying strain versus water content (see Fig. 1c), data points roughly line up around a line and show smaller hysteresis than when displayed versus relative humidity (see Fig. 1a). As explained earlier, in parallel to drying shrinkage (i.e., lengthchange isotherms), experimentalists often measure sorption isotherms. Sorption isotherms measurements consist of placing a sample into an atmosphere at a controlled relative humidity (for water sorption measurements) or controlled partial pressure (for any vapor) and measuring the amount of fluid in the sample. One can measure sorption isotherms on specimens identical to those used for the drying shrinkage measurements by weighing them once they have reached hydric equilibrium. However, sorption measurements are often performed on powders using devices specifically dedicated to sorption measurements, based on gravimetric or volumetric methods (see Section 1.3). Such devices vacuum the sample before measuring its sorption isotherm. Consequently, the specimen needs to be dried before being placed into the device, a necessary pretreatment step. Pretreatment methods include solvent exchange and P-drying. For solvent exchange, the sample is immersed in a solvent (often isopropanol or acetone) to replace water before evaporating the solvent. For P-drying, the specimen is equilibrated at a water partial vapor pressure of 0.008 mmHg = 1.06 Pa. Although simple in principle, drying shrinkage and sorption experiments are quite complex to perform and interpret properly, as will be readily addressed next.

The shrinkage experiments' first complexity is that the hydrated cement paste samples themselves may not be homogeneous. Gravity-induced segregation may cause anisotropy in the specimen [87], which could impair the experiments' reproducibility. Even if samples are homogeneous, moisture gradients occur during drying, as drying occurs through the sample surfaces. Those gradients make it more challenging to interpret the data than if drying was homogeneous throughout the sample. Moisture gradients manifest themselves, for instance, as surface cracks, which can only be avoided by working with specimens with a size smaller than 2–5 mm [88] or even with 1-mm-thick samples [89–91].

Another difficulty is due to the material's complexity that can allow multiple physicochemical phenomena to occur simultaneously. This complexity overshadows the unequivocal interpretation of the experimental data. Such phenomena include hydration, de-hydration of cement hydrates [92], carbonation [93–96], and other reactions that modify the water amount or the microstructure. For instance, ettringite easily releases water molecules as it is dried and absorbs water when rehumidified. How those evolutions of the crystal structure impact the macroscopic length change, which probably plays a role in delayed ettringite formation [97,98], is not clarified yet. Regarding carbonation, since gaseous CO₂ is omnipresent, perfectly mitigating the carbonation of calcium-based samples during the experiment is difficult. Each hydrate that contains CaO is prone to carbonation [99]. The carbonation of portlandite and calcium silicate hydrate (C-S-H) affects the cement paste's shrinkage and the evaporable water content [94,100–102].

In addition to these complexities, C-S-H is metastable [37,103]. C-S-H's local microstructure can easily evolve due to the local variations of relative humidity, which, as we will see, makes it challenging to define hydric equilibrium. The fact that the microstructure evolves after a longterm (i.e., months-long) drying has been proven by nitrogen sorption [104–106], water vapor sorption [12,22,107,108], small-angle neutron or X-ray scattering [109–114], low-temperature calorimetry [115,116], and scanning electron micrography [117-119]. An example of such a phenomenon is visible in Fig. 5, which shows that the pore size distribution, as investigated by hours-long water sorption isotherms, depends significantly on the relative humidity at which the samples have been equilibrated beforehand for six months. More rapid microstructure evolutions have been observed by ¹H NMR relaxometry during water uptake [120-124] and drying [125-127]. The data suggest that those dynamic microstructural evolutions are due to time-dependent evolutions of the interlayer's basal spacing [110,120,125,128] and the distances between C-S-H sheets across gel pores [22,121,125]. Indeed, one observes that synthetic C-S-H's basal spacing (which shows 002 reflections with an ordered structure in the c-axis direction) evolves upon drying [128–131]. Such evolution of the basal spacing is considered the main reason for anomalous water transport in cement-based materials [123,124,132]. It implies that reaching hydric equilibrium upon drying takes a very long time. This C-S-H dynamic rearrangement's characteristic time differs significantly from those of water vapor transport and adsorption, such that properly defining hydric equilibrium is difficult. Suppose the size of the specimen is large. In that case, the moisture transport, which is affected by the C-S-H dynamic rearrangement,

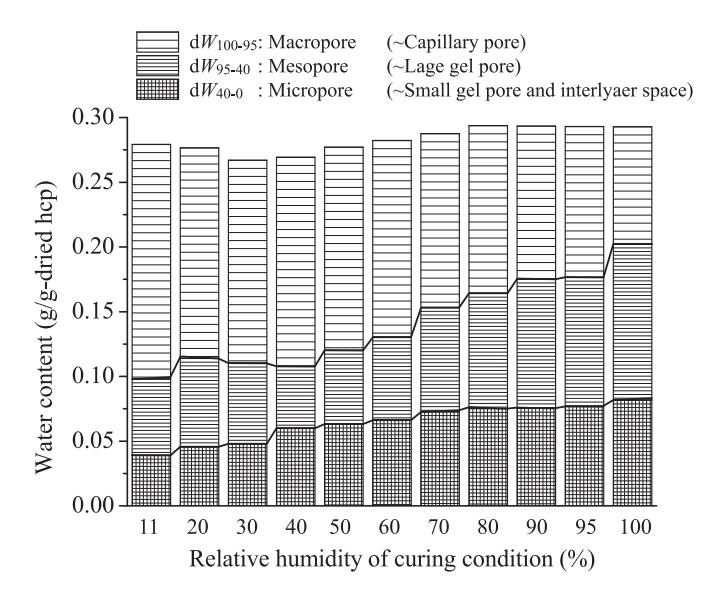


Fig. 5. Impact of long-term drying (6 months) on the pore size distribution of a cement paste with w/c = 0.55 (Figure from [12]).

dominates the phenomenon. As a result, it is challenging to obtain a homogeneous equilibrium for both microstructure and moisture content. When the specimen is tiny, the water content can reach a homogeneous equilibrium value in a reasonable time. Still, the microstructure evolves over a more extended time. Typically, if we consider a specimen whose thickness is 3 mm, hydric equilibrium and the length change will not reach their equilibrium values within a year.

A part of the C-S-H dynamic intra-layer rearrangement (rearrangement of gel pores) and the dynamic variation of inter-layer distance is considered irreversible. Such irreversibility was initially confirmed by length-change isotherms [85,133] and later by nitrogen sorption measurements [106]. The latter showed reversible evolutions of the Brunauer-Emmett-Teller (BET) surface area. The BET surface area is the surface area obtained by applying the BET method to the sorption isotherm. The mechanisms of this irreversibility and the associated modifications of the C-S-H atomic structure remain unknown. Based on quantitative gel permeation chromatography of the trimethylsilyl silicate derivatives [134] and ²⁹Si solid-state nuclear magnetic resonance (NMR) [135], the silicate structure of C-S-H in alite paste and synthesized C-S-H did not show significant evolutions during drying at room temperature. However, with drying at elevated temperatures, the population of Q3-position silicates (i.e., bridging site silicates with an interconnection to a bridging site silicate of a neighboring C-S-H layer) increases. In the case of calcium-aluminate hydrate phases, the number of aluminum atoms in the pairing position increases with drying [12], and the carbonation process enhances this trend [136,137]. Gartner et al. [37] proposed reactions (e.g. \equiv [SiO-Ca(H₂O)₅]⁺ + $^{-}$ OSi $\equiv \rightarrow \equiv$ $SiO-Ca(H_2O)_4-OSi \equiv + H_2O)$ to explain how neighboring C-S-H layers become connected under drying. Still, these propositions are not confirmed by experiments yet. The fact that this alteration of C-S-H upon drying is not fully understood makes understanding water sorption and length-change isotherms difficult. While obtaining experimental data regarding the silicate and aluminate groups is relatively easy, for instance with NMR or X-ray absorption near edge structure (XANES), obtaining data regarding the calcium groups is difficult. From this point of view, molecular simulations could help understand potential pathways of how drying alters the microstructure of C-S-H.

Like for drying shrinkage measurements, performing sorption isotherms measurements and correctly interpreting them is complex. The sorption isotherms are very sensitive to how the hydrated cement paste was pretreated, i.e., how the hydrated cement paste was dried before being placed in the device for sorption measurement. This significant

sensitivity makes it difficult to compare various sets of sorption isotherms with each other [138]. First, as the rate at which water evaporates from the C-S-H is affected by the specimen particle size and by the type of C-S-H, a precise reproduction of the initial conditions for the measurement is difficult. Second, the microstructure's modification is inevitable during the pretreatment. The isopropanol exchange technique is the best pretreatment method for nitrogen sorption and mercury intrusion porosimetry measurements [139,140]. However, Zhang and Scherer showed with TG measurements that isopropanol replacement induces slight carbonation of the hydrated cement paste [140]. This observation indicates that the isopropanol molecules remain in the C-S-H structure, possibly as alcohol-ethylene oxide polymers between C-S-H sheets [141]. Consequently, even isopropanol solvent exchange affects water vapor sorption isotherms and the resultant BET surface area.

We will now give two examples showing the knowledge gaps regarding cement-based materials' sorption behavior. The first example is a discrepancy between N2 and H2O sorption measurements. The specific surface area (SSA) calculated from water sorption measurements is consistently larger than the SSA calculated from nitrogen measurements. For instance, for cement pastes with water-to-cement ratios w/c between 0.35 and 0.7, based on water sorption measurements, Mikhail and Selim [142] found a SSA around 200 m²/g and independent of w/c. In contrast, with nitrogen, they found a SSA that increased with w/c and varied between 50 m²/g to 140 m²/g. There is no consensus on why there is a difference in SSA measured with N2 and H₂O. Feldman and Sereda [32] pointed out that the difference in the adsorbents' size cannot explain the SSA difference. However, they suggest that this difference can be attributed to a) solid-solid contact between C-S-H sheets after drying and/or b) molecular bridging in slit pores the size of a molecule, restricting the adsorption process. They believe that the SSA measured with N_2 is the true SSA of the C-S-H structure. On the contrary, Brunauer et al. [59] provided evidence that the SSA measured with N₂ can only be a fraction of the true SSA of C-S-H: theoretical calculations based on X-ray data showed that the SSA of C-S-H sheets consisting of 3 and 2 molecular layers is 244 and 376 m²/g, respectively, and that, when counting not only the external surface but the interlayer surface as well, this SSA is 755 m²/g.

2. Molecular simulations: methods

2.1. Principle of various types of molecular simulations

Quantum and classical simulation methods are capable of modeling materials at the nanoscale. Atomistic modeling of adsorption phenomena is more common with methods of classical mechanics. The classical atomistic simulations can only be applied if the quantum effects are negligible, i.e., the system size is much larger than the de Broglie wavelength. Otherwise said, the system size should be greater than the characteristic size of the matter's wave-like behavior at the nanoscale. At room temperature, this thermal length scale is in the order of 0.01 nm for a water molecule that is roughly 0.3 nm in diameter. Therefore, computational researchers can safely use atomistic simulations to study nanoconfined water's physical attributes, dynamics, and adsorption in the cement paste. Chemical processes involve the formation or breaking of chemical bonds or charge transfer (e.g., in the case of water dissociation or cross-link C-S-H formation). When chemical processes are relevant to the phenomenon of interest, one needs to use quantum simulations or classical methods that account for bond formation and breaking (such as ReaxFF). The classical molecular simulations' main ingredients are the atomic structures, interatomic potentials, and simulation conditions. The classical molecular simulations' main ingredients are the atomic structures, interatomic potentials, and simulation conditions.

The atomic structures generally adopted in adsorption studies in C-S-H are based on tobermorite structure. For a detailed discussion on the C-S-H structure, the reader should consult the review paper by Manzano

et al. [Reference to Manzano et al. review in the same special issue]. The computational researchers use Hamid's tobermorite crystalline structure [143] to investigate the C-S-H's intermolecular interactions and physical origins of its cohesion [25,144,145]. These studies take the basal distance as the main reaction coordinate. However, they occasionally consider sliding and edge-to-edge configurations as in [25], as well as other arrangements such as face-to-edge and turbostratic stacking [146]). Researchers have also simulated the adsorption isotherms [40,147] and effective intermolecular interactions [146,148,149] using realistic C-S-H models [150]. These studies adopt the defective tobermorite models of Pellenq et al. [150] and its refinement by Qomi et al. [151]. This C-S-H model captures the water content and interlayer spacing -two relevant features for adsorption-related investigations-. With defective structures, it is possible to account for the effects of C-S-H's compositional variability on adsorption processes. For example, effective intermolecular interactions show a dependence on the Ca/Si molar ratio with larger equilibrium interlayer distances (see Table 7) associated with Ca/Si of 1.1 and 1.3 compared to Ca/Si of 1.5 and 1.9 [149]. Kunhi Mohamed et al. [152] have also built a useful C-S-H model based on Merlino's 14 Å tobermorite [153,154]. This model can be useful for molecular simulations of adsorption processes. For this C-S-H model, the authors report silicate chain speciation and mean chain length consistent with experimental data. Still, the water content (under ambient conditions) is lower, and interlayer space larger than the experimental values. In any case, we note that C-S-H exhibits compositional and structural variability that can be difficult to capture with a single model (or even experimentally with synthesized C-S-H). Different crystallinity levels can be associated with C-S-H with, for instance, the existence or not of the 002 XRD or electron diffraction peak (e.g., model of Kunhi Mohamed et al. [152]). A combinatorial ansatz [155] may help overcome this obstacle, but at the expense of increased complexity in computations and analysis.

Computer simulations can only handle a relatively small number of particles. According to the system size, a significant fraction of particles lies close to the boundary of the simulation box, which introduces undesired surface effects. Periodic Boundary Conditions (PBC) enable overcoming this problem [156]: a particle close to the simulation box boundary interacts with the periodic images of the particles on the opposite side of the simulation box, which results in a system without undesired interfaces. However, the use of PBC affects the property of systems close to phase transitions and may introduce artifacts in the computation of diffusion [157].

The interatomic potentials used to describe interactions in the adsorption-related phenomenon in C-S-H are PN-Traz [40,158], CSH-FF [159], and ReaxFF [160]. Mishra et al. [161] reviewed in detail the available force fields used to model the present phases in the cement paste. In the case of non-reactive force fields, one usually describes the potential energy as a sum of various contributions: electrostatic (using the Coulomb potential), van der Waals (often using a Lennard-Jones potential, which includes steric repulsion), and bond (using the harmonic potential, often for covalent bonds and angles). These force fields generally use well-established water models from SPC or TIP families. Ji et al. [162] quantify water models' influence on the water dynamics, lattice parameters, infrared and X-ray spectra, and C-S-H's elasticity. This study comparatively tested SPC, TIP3P, TIP4P, TIP4P05, and TIP5P water models and reported that SPC and TIP5P predict C-S-H's structural features and elasticity better. Force fields are often limited to the application (e.g., capturing elastic properties or interfacial properties) for which they were conceived. Any application out of this scope requires a specific study checking the transferability of the force field. Quantum simulations, being based on first principles, are not subject to this limitation.

A variety of simulation methods are available to investigate adsorption phenomena. Monte Carlo (MC) simulation is the most frequently used method since it allows studying systems with a varying number of particles compared to standard molecular dynamics at a fixed

number of particles. Note that in adapted protocols for a controlled number of adsorbent particles, one can use molecular dynamics (MD) to compute adsorption properties. While classical MD works by integrating Newton's laws of motion, MC simulation follows the random particle displacements that respect a given probability distribution set by the statistical ensemble it operates in. The cornerstone of Monte Carlo (MC) and Grand Canonical Monte Carlo (GCMC) methods is the Metropolis algorithm [163], also known as the Metropolis-Hasting algorithm. The MC method proceeds by applying a random MC move (translation, rotation, insertion, and deletion) to an atom or a molecule. Subsequently, it evaluates the move's energetic cost by computing the potential energy change. The move is either accepted or rejected based on a probability condition related to the calculated Boltzmann factor. In dense molecular systems, the probability of insertion or deletion of a molecule is low. Frenkel and coworkers developed the Configurational Bias Monte Carlo (CBMC) algorithms to increase MC moves' efficiency [164]. The general principle is to grow the molecule piece by piece. The method attempts to place the next atoms in the molecule based on the biased positions with respect to the molecular topology. The CBMC's various formulations differ in how the algorithm inserts atoms in a given

Various simulation packages are available to perform classical molecular simulations, including LAMMPS [165] for MD and MC, DL_POLY [166] for MD, GULP [167] for MD and GCMC, GROMACS [168] for MD, and Towhee [169] for MC (including CBMC).

A small set of parameters (i.e., the pressure *P*, temperature *T*, volume V) define the thermodynamic state of a multi-component system consisting of *N* particles. The position and momenta of the various particles in the system constitute a 6N-dimensional space called the *phase space*, l. The system properties (e.g., density, elastic response, heat capacity, diffusion coefficient, etc.) are a function of the thermodynamic state instead of being a function of the particles' various positions and momenta with a given instantaneous state. The ergodicity hypothesis states that a given observable's time average converges to the "macroscopic" thermodynamic value, $H = \langle \mathcal{H}(l(t)) \rangle_{time}$ [156]. This time average can be replaced by an ensemble average on snapshots of the system at a given time, in which an ensemble is a collection of points l(t)in the phase space. These points follow a given probability distribution in an ensemble corresponding to thermodynamic state parameters. Thus instead of following the system's time evolution in equilibrium, the sampling of the probability distribution function associated with a given ensemble can generate various snapshots. This aspect is central to the Monte Carlo simulations.

The prominent ensembles used in atomistic simulations include (e.g., [156,164,170]):

- Microcanonical ensemble (NVE): The number of particles *N*, the volume *V* and energy *E* are fixed. This ensemble corresponds to a completely isolated system, with no exchange of particles or energy with the outside environment.
- Canonical ensemble (NVT): The number of particles *N*, the volume *V* and temperature *T* are fixed. This ensemble corresponds to a system that is allowed to exchange energy with a large grand reservoir with a given temperature (i.e., a thermal bath) but is not permitted to exchange particles with this reservoir (i.e., a closed system).
- Grand canonical ensemble (μ VT): The chemical potential μ , the volume V and temperature T are fixed. Therefore, the number of particles, pressure, and energy fluctuations. This ensemble corresponds to a system that can exchange energy and particles with a large reservoir, imposing the system's temperature and chemical potential.
- Isothermal-isobaric ensemble (NPT). The number of particles *N*, the pressure *P*, and temperature *T* are fixed. This ensemble corresponds to a system that can exchange energy and volume with a large reservoir at a given temperature and pressure but with no particles (i. e., a closed system).

• Grand isobaric or osmotic ensemble ($N_s\mu_{ad}$ PT): The chemical potential μ_{ad} of the sorbent, the pressure P, and temperature T are fixed in a system with a number constant number of non-sorbent particles N_s (e.g., particles in the solid pore walls or counterions). This ensemble corresponds to a system that can exchange energy and sorbent particles with a grand reservoir imposing the temperature and the sorbent chemical potential. The system is also exchanging volume with this reservoir to set the mechanical pressure. However, we should note that simulating the osmotic ensemble is possible only if one extensive parameter is fixed to specify the system size. We cannot simulate a fluid in this ensemble alone because μ , P, and T are not independent. After all, the Gibbs-Duhem relation links these quantities. This ensemble can treat a porous medium filled with a fluid, though, since the number of solid particles provides the extensive parameter needed to quantify the system size.

One can compute various observables during the simulation or at a later post-processing stage to unveil the atomic-level details of adsorption processes (e.g., [156,164,170]):

- Structural data: Radial and Pair distribution functions (RDF and PDF) provide information on the structural correlation of pairs of particles and provide critical information regarding structural and phase changes in the material (see, e.g., [171] for the case of phases in cement-based systems). Researchers use the total and pair radial distribution functions to compare the structure obtained from simulation with experiments [150,155,172,173]. The RDF analysis reveals the effects of confinement in water structure [174]. The integration of the RDF provides the coordination number, which can be useful in quantifying hydration shells in electrolytes (e.g. [175]). The Fourier transform of the RDF is directly related to the structure factor S(q), which is crucial in interpreting scattering patterns obtained from diffraction experiments. Post-processing of the atomic configurations with specific codes (e.g., Debyer, Mercury) yields estimations of the diffraction (neutron or X-ray) patterns. One can compute density profiles to show how the density or the number of particles varies along a given coordinate (for example, the pore thickness). This information is essential to unveil the water's layering adjacent to surfaces (e.g., [25,145,176-178]). Comparison with Xray reflectivity data is also possible when this data is available, as is the case for calcite and quartz, for example.
- Pressure: the calculation of pressure in a molecular simulation follows the virial equation (e.g., [156,164,170]):

$$P = \frac{Nm\langle v \rangle^2}{dV} + \frac{\sum_{i}^{N'} r_i f_i}{dV}$$
 (5)

where d is the system's dimension, and the number of the atoms N' includes the periodic replicas in periodic boundary conditions. The second term is the virial, which is equal to -dU/dV, and it is the default method of computing pressures in most simulations. The ensemble average of the Virial yields a measure of Cauchy's stress. Still, there is a discussion in the literature on using the interatomic force term alone to define the Cauchy stress [179]. In layered materials, the stress orthogonal to the layers is referred to as the confining pressure. The difference between the *confining pressure* and the pressure of a fluid reservoir with which the system is in equilibrium (this pressure corresponds to the capillary pressure in hierarchical porous materials) is the so-called disjoining pressure (see Section 1.3). Confining and disjoining pressure exhibit an oscillatory behavior resulting from fluid ordering within pore sizes on the order of a few molecules diameter. Fig. 6 sketches a typical pressure isotherm and corresponding free energy for layered materials. pHdependent ionic correlations interactions modulate these forces [180–182]. The minimum value of the disjoining pressure is the *cohesive* pressure, corresponding to the pressure required to disjoin two layers.

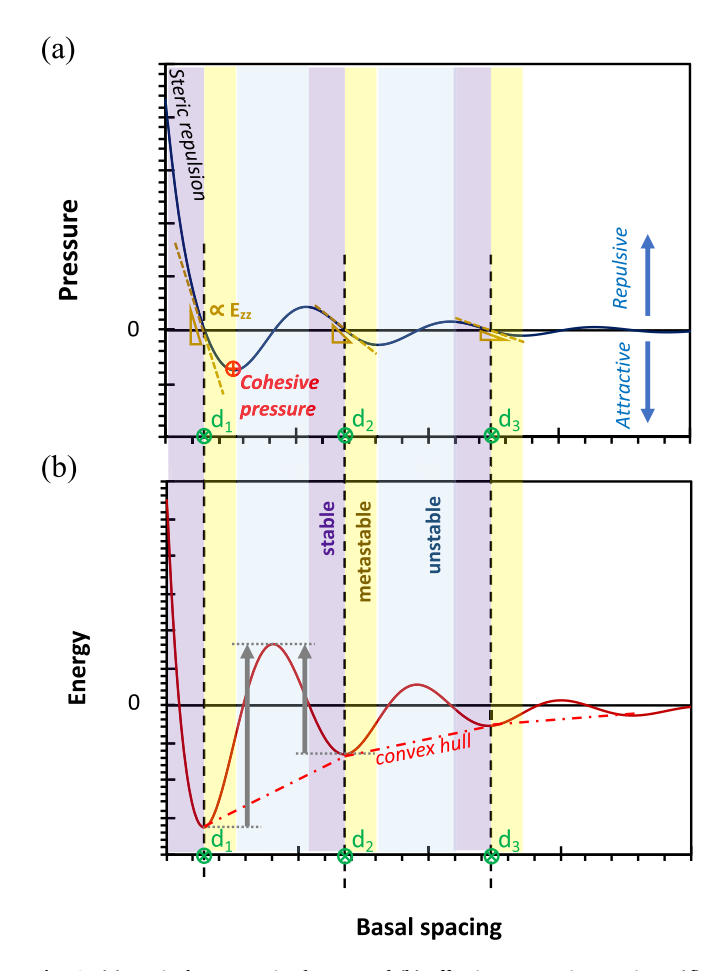


Fig. 6. (a) Typical pressure isotherms and (b) effective energy interaction $\Lambda(d)$ (Eq. (6)) of adsorbing layered material. For small basal spacings, steric repulsion drives the behavior; then, oscillatory pressure and energy profiles arise due to water layering within the slit pore. Each oscillation is associated with a hydration state (or a specific number of water layers within the slit pore). The figure depicts the stable (purple), metastable (yellow), and unstable (light blue) domains for each hydration state. The equilibrium basal spacing d_X (corresponding to the (local) minima in the energy profile) for each hydration state X are identified (see Table 7 for the values reported in the literature). The figure also shows the cohesive pressure, i.e., the minimum in the pressure isotherm and the slope from which one can compute the Young's modulus E_{zz} orthogonal to the pore plane. See Section 4.1 for more details. (For interpretation of the references to colour in this figure legend, the reader is referred to the web version of this article.)

- Hydration energy is computable as $\Delta U_H = (\langle U(N) \rangle \langle U(0) \rangle)/N$, where $\langle U(N) \rangle$ is the average potential energy when the water content is N. The hydration energy tends to the average bulk water energy when the water content increases. A hydration state different from *N*=0 can serve as a reference in hydration energies computation, e.g., when a stable intralayer crystalline water is reported (as in crystalline alkali-silica reaction (ASR) products [183]). Besides the effects of adsorbent water's potential energy, the hydration energy accounts for the changes in the interaction among layers and counterions due to variable water content, including the energy needed to disjoin dehydrated layers [184]. This parameter relates to the relative thermodynamic stability of the adsorbent layered material. A ΔU_H lower than the energy of bulk water designates a thermodynamic driving force for hydration. A ΔU_H larger than the energy of bulk water, however, shows thermodynamic driving force for dehydration.
- Isosteric heat (or enthalpy) of adsorption can be approximated by a finite difference method using $q_{st}(N_m) = (\langle U(N) \rangle \langle U(N') \rangle)/(N-N')$,

where $N_m = (N + N')/2$ [177]. In general, q_{st} oscillates around the value of bulk water vaporization enthalpy. A q_{st} value above the vaporization enthalpy indicates an enthalpic driving force for further hydration. A q_{st} below the vaporization enthalpy indicates an enthalpic driving force for dehydration. The isosteric heat of adsorption can be computed from GCMC simulation using a fluctuation formula (see Table 3).

- Immersion energy is defined as $Q_{im} = \langle U(N) \rangle \langle U(N^\circ) \rangle \langle N-N^\circ\rangle U_{bulk}$, where $\langle U(N^\circ) \rangle$ is the average potential energy at an arbitrarily chosen reference hydration state N° , and U_{bulk} is the average interaction energy of bulk water using the same water model [177]. The main limitation of these approaches based on water content control is that the water content imposed cannot be directly linked to (and may not correspond to typical variations of) the relative humidity.
- Effective interactions. The effective interaction is computable via the integration of the confining pressure along the basal spacing direction as follows:

$$\Lambda(d) = \Lambda_0(d_0, T, \mu) - A \int_{d_0}^{d} \langle P \rangle d(d_c)$$
 (6)

for a system under volume control. Under pressure control, the corresponding energy, often called swelling free energy in clay science (e.g., [185,186]) is $\Lambda_*(d) = \Lambda - A\langle P\rangle d$. These free energy profiles provide information on the stable hydration states of the layered material, the prevalence of these states, and the energy barriers associated with hydration state transitions. Bonnaud, Honorio, and coworkers [145,146] used GCMC to compute the effective interactions between calcium silicate hydrates layers. It is also possible to calculate this in an NVT ensemble using free energy methods such as umbrella sampling and free energy perturbation methods [25,187]. The effective interactions are one of the main inputs in coarse-grained simulations at the mesoscale. The simulation literature reports effective interactions [146,181,187] or without repulsive shoulders [25,145]. Masoumi et al. [187] showed that the repulsive shoulders are only present at Ca/Si > 1.5 due to the double-layer repulsion absent at low Ca/Si ratio. Properties such as the *surface energy* γ_s , *cohesive pressure* P_{co} , i.e., the pressure needed to disjoin two layers, and the Young's modulus orthogonal to the pore plane E_{zz} is computable from pressure isotherms and effective interactions. The analysis of pressure isotherms and interaction energies might perform a stability analysis and define hydration phases diagram for layered adsorbing layered materials [188]. Such stability analysis is critical to the comprehension of adsorption phenomena driven by snapthrough instabilities [189,190]. Multiscale approaches, using quantum and coarse-grained computation, show that the surface forces in C-S-H are pH-dependent [191].

Table 3 Physical properties. *E* is the Hamiltonian [156].

	Finite difference	Fluctuation- dissipation
Heat capacity (at constant volume) C_V	$\left(\frac{\partial E}{\partial T}\right)_{V}$	$\langle \delta E^2 \rangle_{NVT}/(k_B T^2)$
Heat capacity (at constant pressure) C_P	$\left(\frac{\partial H}{\partial T}\right)_{p}^{r}$	$\langle \delta(E+PV)^2 \rangle_{NPT} / (k_B T^2)$
Coefficient of thermal expansion α_P	$\frac{1}{V} \left(\frac{\partial V}{\partial T} \right)_{P}$	$\langle \delta V \delta (E+PV) \rangle_{NPT} / (V k_B T^2)$
Isothermal compressibility $\beta_T = 1/K$ (i.e., the reciprocal of the bulk modulus K)	$\frac{-1}{V} \left(\frac{\partial V}{\partial P} \right)_T$	$\langle \delta V^2 \rangle_{NPT} / (V k_B T)$ or $\langle \delta N^2 \rangle_{\mu VT} / (N^2 k_B T / V)$
Stiffness tensor C_{ijkl}	$\frac{1}{V} \frac{\partial^2 E}{\partial \epsilon_{ij} \partial \epsilon_{kl}}$	$rac{k_BT}{\langle V angle}ig[raket{\delta\epsilon_{ij}\delta\epsilon_{kl}}_{NPT}ig]^{-1}$
Isosteric heat of adsorption $q_{st} = RT - q$	$qpproxrac{\partial\langle E angle}{\partial\langle N angle}$	$q = \langle \delta E \delta N \rangle_{\mu VT} / \ \langle \delta N^2 \rangle_{\mu VT}$

- H-bond statistics can quantify the "structuredness" of water [192], shedding light on the changes in fluid structures due to phase transitions, specific ion effects, and confinement. Various criteria regarding donor-donor distance and O-H···H triplet angle are available in the literature [192]. The OH groups outside of molecular water (e.g., in silanol or hydroxide ions in the pore solution) also contribute (as donors) to the H-bond network may play a crucial role in hysteresis in microporous materials [193]. In C-S-H, the number of bonds between silica oxygen (Os) and water oxygen (Ow) decreases with the increase of water content in the interlayer, while the number of Ow-Ow H-bonds increase, making these bonds the main bridging links between the layers [194]. Ab initio simulations used to analyze H-bonds in 11 Å tobermorite providing helpful information to interpret infrared and Raman spectra based on the vibrational density of states [195]. The quantification of H-bonds connectivity in jennite, assessed by ab initio simulations [196], helps to explain some discrepancies in the NMR and X-ray diffraction results.

The changes in water content in the microporous phases in cement-based materials may result in physical properties changes. The equilibrium configurations obtained from molecular simulations at a given RH and temperature can be used as input in simulations to estimate the various physical properties gathered in Tables 3 and 4. Auto-correlation functions, a.k.a. Green-Kubo relations, yield transport coefficients. A cross-correlation function provides the dielectric permittivity.

2.2. The relevance of molecular simulations in terms of length and time scales

Like any other experimental, theoretical, and simulation technique, atomistic simulations have their limitations (e.g., [156]). The MC scheme's success is contingent on applying numerous single atom moves to ensure the convergence of statistical averages. In practice, this limit renders parallelizing techniques inapplicable to MC methods. Therefore, these methods remain limited to small domain systems. Particularly, in bulk and confined water simulations, the MC moves can entail rearrangement of the hydrogen bond network that would be computationally prohibitive to converge accurately.

In Molecular Dynamics (MD) simulations, the statistical averaging requires either performing the block average technique or equivalently averaging over unbiased samples along the MD trajectory. This requirement necessitates that the MD trajectory is long enough to allow proper sampling of the physical observable, to obtain the average and standard deviation. Similarly, when calculating autocorrelations, one should pay special attention to numerical convergence. The autocorrelation function's convergence can be erroneous at long time lags when the signal-to-noise ratio becomes strongly affected by the MD trajectory

Table 4 Coefficients of transport from auto-correlation functions (for static values) (e.g., [156,164,170]). In the correlation functions, v is the velocity, J is the heat flux, J_I is the ionic current flux, M is the polarization or total dipole moment, and P' is the instantaneous pressure.

	Correlation function
Self-diffusion coefficient D	$D=rac{1}{3}\int\limits_{0}^{\infty}\langle v(t)v(0) angle dt$
Thermal conductivity λ	$\lambda = \frac{V}{k_B T^2} \int_{0}^{\infty} \langle J(t)J(0) \rangle dt$
Electrical conductivity σ_E	
Dielectric permittivity ϵ_D	$egin{aligned} \sigma_E &= rac{1}{3\epsilon_0 V k_B T} \int \limits_0^\infty \langle J_I(t) J_I(0) angle dt \ & \epsilon_D &= 1 - rac{1}{3\epsilon_0 V k_B T} \int \limits_0^\infty \left\langle M(t) rac{d}{dt} M(0) ight. ight angle dt \end{aligned}$
Dynamic viscosity η	$\eta = \frac{V}{k_B T} \int\limits_0^\infty \langle P'(t)P'(0) \rangle dt$

size. Since MD simulations are based on the finite-difference technique, their trajectory size is strongly dependent on the designated time step [156]. This time step should be, in principle, much smaller than the period of the fastest vibrational frequency present in the system.

The fastest vibrational frequency in hydrated cement pastes corresponds to OH bonds' stretching mode in water molecules and hydroxyl groups, \sim 110 THz or \sim 3700 cm⁻¹. The period of this frequency is \sim 0.01 ps (picosecond: 10^{-12} s). Therefore, a time step of 1 fs (femtosecond: 10⁻¹⁵ s) is required to resolve OH bond dynamics when employing classical non-reactive force fields. In reactive simulations, e. g., ReaxFF, the time step is usually reduced to 0.1-0.2 fs to ensure numerical stability and accurate description of chemical reactions such as proton transfer steps. If, for computational cost considerations, one decides to use rigid water models (e.g., rigid SPC) and OH bonds, the fastest frequency will correspond to the stretching and bending vibration of silicate monomers and dimers, $\sim 35~\mathrm{THz}$ or $\sim 1150~\mathrm{cm}^{-1}$. These vibrations correspond to a period of ~ 0.03 ps, which necessitates a time step of at most 3 fs with classical force fields. Therefore, depending on the employed force field and associated time step, one needs to simulate 0.33 to 10 million MD steps to reach only 1 ns. The need to compute millions of finite-difference steps highlights MD simulations' computational expense and their limitations to achieve longer time scales.

While nanosecond MD simulations are accessible thanks to computational power advancements, one should pay close attention to the finite difference scheme's accumulated numerical error. When running long MD simulations, numerical errors accumulate, resulting in the deviation of the state variables from the designated ensemble by exploring thermodynamically inaccessible regions of the phase space (e.g., [156]). For instance, when running MD simulations in the NVE ensemble, the internal energy should remain strictly constant during the simulation, as per the microcanonical ensemble definition. However, due to numerical errors, the internal energy might deviate from a predefined value. It is needless to say that the numerical errors depend on the finite difference scheme used to integrate the equations of motion. The explicit velocity Verlet algorithm is usually adopted and sufficient to describe the dynamics accurately. However, if the error accumulations are significant, more expensive implicit methods such as higher-order Gear are suggested. From a practical perspective, finite difference errors become significant when reaching 10 ns using 1 fs time steps. Therefore, while achieving 100 ns is computationally feasible with existing supercomputing infrastructures, one should treat long MD simulations with utmost caution.

Resolving time scale limitations is the subject of advanced computational physics and statistical mechanics techniques. A breakthrough in developing and applying such methodologies to cement-based materials bears the promise to provide a mechanistic picture of nanoscale cement chemistry processes at macroscopic time resolutions. Such progress would ultimately enable one to study the atomic origins of creep, shrinkage, and dissolution processes, to name only a few. From the perspective of statistical physics, such methods are deeply rooted in the notion of rare event sampling, i.e., exploring the regions of the phase space that are "rarely" accessible via thermal fluctuations in the conventional MD or MC frameworks. Otherwise stated, if the energy barrier between two adjacent local minima is greater than a few k_BT , the system might not explore the two minima and become metastable by being confined into a local minimum. Rare event sampling methods allow the system to overcome energy barriers by introducing bias potentials. Researchers in the MC community refer to these methods as the enhanced or biased sampling methods [164], e.g., parallel-tempered Markov Chain Monte Carlo [197] and modifications of Wang-Landau Algorithm for adsorption simulations [198]. In the MD community, there are multiple techniques such as replica exchange MD [199], metadynamics [200], and transition path sampling [201], among others. While the detailed description of these methods falls beyond this treatise's scope, interested readers are encouraged to read the highlighted papers and references therein.

The most computationally intensive task in MC and MD simulations is evaluating coordinate-dependent potential energy and interatomic forces. Within these evaluations, the most expensive step is evaluating non-bonded interactions. Considering a system composed of *n* particles, typical molecular dynamics simulations scale by $O(n^2)$, if one considers all pairwise electrostatic and van der Waals interactions explicitly. Employing electrostatics methods such as particle mesh Ewald summation (O(n*log(n))), particle-particle-mesh, or spherical cutoff-based Wolf summation (O(n)), can reduce this computational cost. Therefore, the computational cost increases linearly with the number of particles or otherwise stated the system size. Parallel computing techniques such as the domain decomposition method have primarily solved the system size's computational limitations. While it is possible to run simulations with millions of atoms corresponding to a cubic simulation box with a side of $\sim\!25$ nm, such simulations are rare in the cement chemistry community.

The underlying reason to settle with smaller simulation cells is limited access to vast multi-node supercomputing resources. Even though such computational resources might be accessible, it is challenging to perform rigorous statistical analysis. It requires simulating many copies of the systems with different initial conditions (e.g., initial velocity seeds, defect locations, etc.), which is computationally prohibitive. In MD simulations of the solid C-S-H (C-S-H globules), the simulation cell sides vary between 2 and 5 nm, containing ~1000-4000 atoms depending on the defect population considerations. With the current computing technology, it is possible to simulate such systems on a desktop computer and collect a nanosecond trajectory within a few hours. When studying the interfacial phenomena, gel porosity, and surface forces, MD system size can reach 10 nm to explore either larger slit pore widths or provide enough screening to avoid the spurious consideration of surface forces from the periodic images. In such relatively large simulations, the number of atoms can reach 10,000-20,000 particles. For instance, when calculating the face-to-face surface forces between tobermorite layers, Masoumi et al. [202] modeled two calciumsilicate layers and ~ 3500 water molecules, reaching a total of $\sim 12,000$ atoms. Each nanosecond of these simulations consumed ~150 central processing unit (CPU) hours on a distributed computing server.

An alternative approach to overcome time and length scale limitations in atomistic simulations is applying coarse-graining techniques. With these methods, the simulation size can approach the micrometer length [203], and simulation times of tens of microseconds are accessible [204]. We will discuss applying these methods to model the C-S-H gel's structure and explore the drying shrinkage effects on the C-S-H gel structure in more detail in Section 3.2.

3. What was learned from molecular simulations regarding drying shrinkage of cement paste?

Various authors have utilized molecular simulations to study the adsorption and interfacial processes in crystalline and defective calcium silicates hydrates (Table 5). First-principles, classical molecular dynamics, and Monte Carlo simulation techniques have been deployed to obtain atomic-level information. Obtaining such information experimentally and under well-controlled conditions can be challenging. The properties computed from simulation include the disjoining pressure, adsorption isotherms, mechanical, thermal, and dielectric properties. The simulations enable quantifying how the confinement changes water structure and properties. They also help to understand the physical origins of phenomena such as hysteresis and volume changes under sorption. We discuss the main advances in the understanding of these aspects in the following.

3.1. Physical properties of water confined in cement paste

Molecular simulations have so far provided information to complement the nanoscopic picture of confined water in C-S-H. Table 6

Table 5

Non-exhaustive inventory of molecular modeling studies on adsorption and interfacial related process in calcium silicates hydrates.

Study	Type of molecular simulation	Model for solid	Interaction potential	Conditions	Properties studied
Gmira et al. [144]	0 K (classical minimization and ab- initio)	Tobermorites of Hamid [143] and Merlino et al. [154]	Core-shell (solid and water)	T: 0 K	Dis. press.
Bonnaud et al. [40]	GCMC	Defective C-S-H from Pellenq et al. [150], $C/S = 1.65$	PN-TrAZ and Rigid SPC	T: 300 K, RH: 0% to 100%	H2O cont. Heat ads. Dis. press.
Manzano et al. [205]	MD (NPT)	Defective C-S-H from Pellenq et al. $[150]$, C/S = 1.65	ReaxFF parametrized as in [160]	$T=298~\mathrm{K},~1~\mathrm{atm}$	RDF, shear stresses, MSD Elastic Mod. Dipole moment distribution
Bonnaud et al. [148]	GCMC, MD (NPT/ NVT)	Defective C-S-H from Pellenq et al. $[150]$, C/S = 1.65	CSH-FF and flexible SPC (intra- granular), PN-TrAZ and rigid SPC (inter-granular)	T: 260 K to 575 K, Constant fugacity (saturation at 300 K)	H2O cont. Elastic mod. Deformation Heat cap. Th. exp. Dis. press.
Hou et al. [194]	MD (NPT/NVT)	Defective C-S-H created with the same procedure as from Pellenq et al. [150], $\label{eq:constraint} \text{C/S} = 1.69$	CSH-FF and Rigid SPC	Т: 300 К	Deformation Density prof. MSD TCF Elastic mod. Strength
Bonnaud et al. [146]	GCMC	Defective C-S-H Pellenq et al. [150], C/ $S = 1.65 \label{eq:section}$	PN-TrAZ and Rigid SPC	T: 300 K, RH: 10% Varying basal distance and stacking configurations	H2O cont. Dis. press Elastic mod.*
Bonnaud et al. [206]	GCMC/MD (NVT)	Defective C-S-H Pellenq et al. [150], C/ $$\rm S=1.65$	PN-TrAZ and Rigid SPC	T: 100 K to 575 K, Fugacity and the saturation vapor pressure	Drained and undrained pore pressures MSD Diff. Ea
Masoumi et al. [25]	MD (NVT/FEP)	Tobermorite of Hamid [143]	CSH-FF	T: 300 K, Varying basal distance Liquid saturation	PMF (face to face and sliding) Surface energy Elastic mod. Pco
Masoumi et al. [187]	MD (NVT/FEP)	Defective Tobermorite with Ca/Si $=$ 1.1, 1.3, 1.5, 1.7 and 1.9	CSH-FF	T: 300 K, Varying basal distance Liquid saturation	PMF Surface energy Elastic mod. Pco Diel. Const.
Honorio [145]	GCMC	Tobermorite of Hamid [143]	CSH-FF	T: 290 K to 330 K, Water pressure – 235 to705 MPa, Varying basal distance Liquid saturation	PMF Surface energy Elastic mod. Pco App. Biot Coeff.

 $\label{eq:H2O} \mbox{H2O cont.} = \mbox{water content}$

 $Heat \ ads. = isosteric \ heat \ of \ adsorption$

Dis. press. = disjoining pressure

Elastic mod. = elastic moduli (bulk, shear, Young's moduli) *Young's modulus orthogonal to the pore plane

Heat cap. = heat capacity

Th. exp. = thermal expansion

Density prof. = density profile

RDF = radial distribution function (and associated statistics)

MSD = mean square displacement (and diffusion)

Diff. Ea = energy of activation of self-diffusion

 $TCF = time \ correlation \ function \ (and \ derived \ properties, \ e.g., \ viscosity)$

Strength = compressive or tensile strength

 $PMF = Potential \hbox{-of-mean-force}$

Pco = cohesive pressure

 $Diel.\ Const. = Water\ static\ dielectric\ constant$

summarizes a comprehensive collection of confined water properties in the C-S-H from the experimental and simulation literature. We categorize the properties according to the definition of water type presented in Section 1.2. Kalinichev, Korb, and coworkers [207,208] compared the self-diffusion constant of the interfacial water on the surface of 14 Å tobermorite in molecular dynamics simulations with those measured by

PFCR in the cement paste. They found that the diffusion coefficient of water between silicate asperities on the tobermorite surface is 5×10^{-11} m²/s, an order of magnitude smaller than the calculated diffusion coefficient of water in the slit pore, 6×10^{-10} m²/s. These values are remarkably close to the measurements of self-diffusion coefficients in the gel $(4\times 10^{-10}$ m²/s from ENS and 5×10^{-10} m²/s from PFCR) and

Table 6
Classification of water types in the cement paste and associated thermophysical properties from experiments and atomistic simulations. Consult the main text for the definition of different characteristic times. (s): molecular simulations. (e): experiments. We discuss the definitions of m, s, and r in Section 1.2. || designates the component of the dielectric permittivity parallel to the surface.

Water type	Characteristic length (nm)	Characteristic times (ns)	Self-diffusion coefficient (m²/s)	Heat capacity C_p (J/g/K)	Isosteric heat of adsorption (KJ/mol)	Dielectric constant	T2 relaxation time (us)
Interlayer	d < 0.5	$ au_m \sim 1.0$ for mobile H ₂ O and much longer for immobile (s) [210]	Immobile or 3.0×10^-12 (s) [210]	~0.9–1.05 (s) [148,211]	120 @ low ads. 90 to 61 with increasing ads. (s) [40]	$\epsilon_{\lor} < 10$ (s) [149]	63–126 ^a (e) [19,126,127,215]
Interfacial	d < 0.75	$\tau_m \sim 1.0-1.3$ (e) [49,51] $100 < \tau_s < 20,000$ Depending on the cement paste(e) [52]	2.6×10–11(e) [3] to 5×10 ⁻ -11 (s) [207,216]	N.A.	120 @ low ads. 105 to 55 with increasing ads. (s,e) [149,217]	$\epsilon_{\lor} < 20$ (s) [149]	N.A.
Gel	0.5 < d < 8	$\tau_r \sim 0.04$ (e) [46]	4×10^-10 (e) [46] to 6×10^-10 (s) [207,216]	N.A.	~55 (s,e) [40]	$10 < e_{\lor} < 64 \text{ (s)}$ [149]	300–420 [19,126,215]
Capillary/ Bulk	d > 8	0.005 (e) [44]	2.3×10 ⁻⁹ (e) [210]	~ 4.2 (e) [211]	45 (e) [40]	66.3 (s) [217] - 80.4 (e) [218]	>1000 ^b [19,126,215]

^a The relaxation time depends on the presence of ferrite and other elements that affect the applied magnetic field. These experimental values are typical of European white cements and include the signal from H atoms of C-S-H's hydroxyl groups.

interfacial ($2.6 \times 10^{-11} \text{ m}^2/\text{s}$ from PFCR) water in experiments that are respectively one and two orders of magnitude smaller than the selfdiffusion coefficient of water at the room temperature, 2.3 $\times\ 10^{-9}$ m²/s. By calculating dipolar correlation functions in MD simulations, Bhatt et al. [209] studied the dependence of relaxation times on translational and rotational motion of water molecules in the interlayer of anomalous tobermorite and a 1 nm slit pore. They computed a correlation time of several orders of magnitude larger than those measured in NMR measurements. They rightfully connected it to the absence of paramagnetic impurities in the C-S-H model. Youssef et al. [174] studied water structure in the interlayer of C-S-H. They found it has a glassy nature akin to those observed in QENS [24] and low-temperature nearinfrared spectroscopy [48]. Later on, Oomi et al. [210] studied the diffusive water behavior in C-S-H interlayer at different calcium-to-silicon ratios. They found that while some water molecules remain immobile within the span of a molecular dynamics simulation, others perform slow concerted successive hops with a diffusion coefficient at least three orders of magnitude smaller than that of bulk water. Interestingly, they calculated that such molecular jumps' characteristic time was roughly 1.0 ns, in striking agreement with PFCR measurements of 1.3 ns. This result suggests that molecular jumps of interfacial and "mobile" interlayer water molecules might have the same characteristic

Bonnaud et al. [40] calculated the isosteric heat of adsorption in the C-S-H interlayer and a C-S-H gel nanoporosity. In agreement with experiments on tobermorite, they showed the adsorption energy decreases with increasing water content due to the hydrophilicity of the C-S-H surface. Bonnaud et al. [148] also showed that the interfacial and gel water contents depend strongly on the temperature. They demonstrated quantitatively that, as the temperature increases, water leaves the C-S-H nanoporosity allowing drying shrinkage. Later, Bonnaud et al. [206] considered the effect of pore connectivity (closed vs. open porosity) on nanoconfined water and its thermophysical properties. They confirmed that, for what concerns nanopores, only open ones collapse upon heating the cement paste (drying): the pressure build-up in closed pores prevents shrinkage since water molecules remain trapped in the closed nanopores. The process of temperature-induced drying shrinkage is intimately related to the thermal properties of cement paste. Qomi et al. [211] calculated the thermal properties of cement paste and showed that the apparent heat capacity of interlayer water is ~25% of that of the bulk water (4.2 J/g/K). These calculations agree with Bentz's postulate stating that the heat capacity of chemically and physically bound water within the C-S-H gel should be significantly lower than that of bulk water [212]. The surface forces between C-S-H layers influence drying shrinkage directly. The permittivity of the gel water screens these forces. Masoumi et al. [149] calculated the dielectric constant of water in nanoconfined water as a function of pore size. They showed that the constant dielectric water exponentially decreases with decreasing pore width. MD simulations in hydrophilic and hydrophobic slit pores show that the parallel and perpendicular components of the dielectric permittivity tensor oscillate near the pore walls, retrieving the bulk values for distances exceeding approximately 1 nm [213,214].

3.2. Impact of relative humidity and temperature change on water content, dimensional change, and hysteresis

3.2.1. C-S-H modeling by considering Ca/Si ratio and H₂O/Si

To demonstrate the predictive power of atomistic simulations, we present a quantitative comparison of the predictions of C-S-H's water content and basal spacing as a function of calcium-to-silicon ratio (Ca/ Si) between simulations and experiments in Fig. 7. As shown in Fig. 7a, both experiments and simulations indicate that C-S-H's water content increases linearly with increasing Ca/Si. In this case, the quantitative comparison between the simulation and experiments requires recognizing the experiment's nuances and whether they explore interlayer water, or perhaps they include interfacial and gel water in the water content estimations. It appears that mild drying experiments (below 110 °C) performed by Fujii et al. [219], Richardson [220], Beaudoin et al. [221], Cong and Kirkpatrick [222], and L'Hopital et al. [223] explore to some extent the interfacial and gel water content in addition to the interlayer water. So do the sorption and thermo-gravimetry analysis (TGA) experiments by L'Hôpital et al. [223]. However, through severe drying at 110 °C performed by Richardson [220] and Cong and Kirkpatrick [222], the measured water content seems to correspond to the interlayer water. Such measurements agree with Muller et al.'s ¹H NMR relaxometry [19] and Allen et al.'s SANS experiments [224]. These interlayer water content measurements are in quantitative agreement with Qomi et al.'s GCMC calculations [210]. By performing reactive molecular simulations, Qomi et al. [151] showed that a portion of interlayer water decomposes to hydroxyl groups and protons. They also showed that the hydroxyl groups coordinate with interlayer calcium atoms, and the protons are transferred to the silicate groups to produce silanol groups. They subsequently revealed that the number of formed Ca-OH bonds agrees quantitatively with those measured by Thomas et al. [225] via the inelastic neutron scattering technique. These observations confirm that atomistic simulations can

 $^{^{}b}$ ¹H NMR Carr-Purcell-Meiboom-Gill (CMPG) decay shows four distinct T_2 decays. The largest one is assigned to capillary pores, and the second largest is assigned to interhydrate pores. The value that we present here is the second-largest T_2 value.

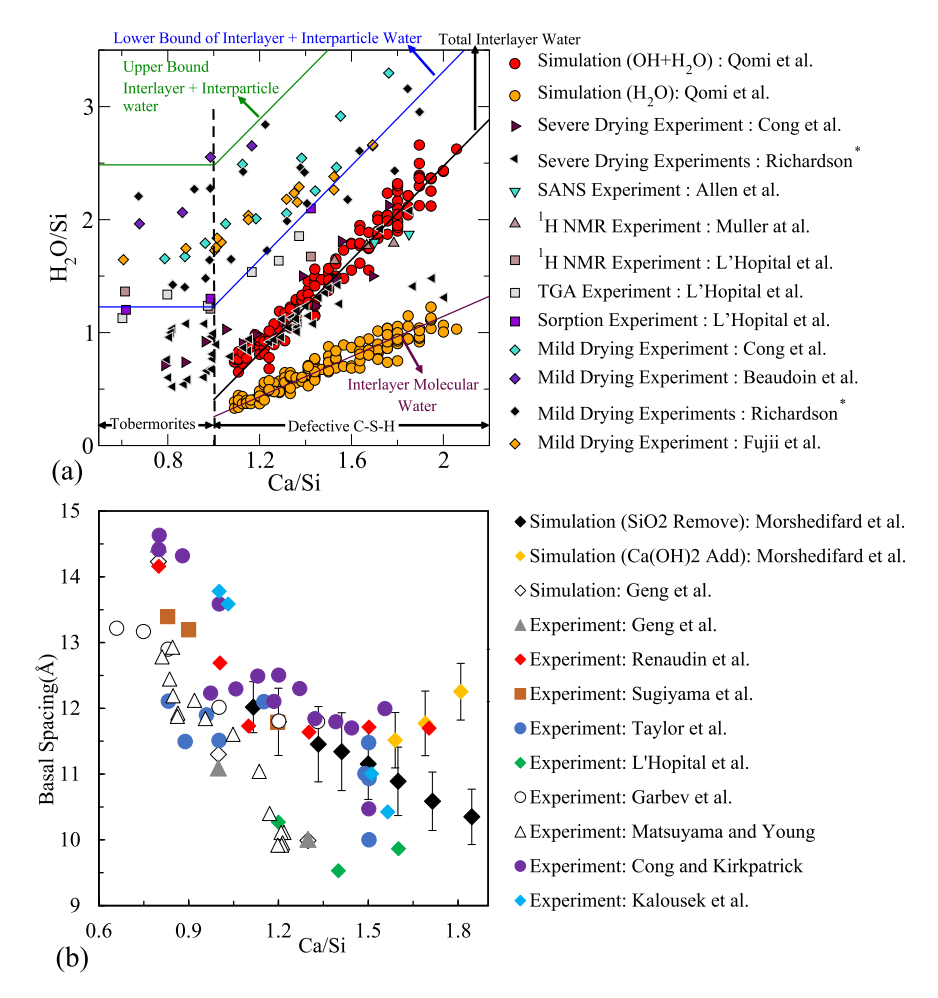


Fig. 7. Collection of molecular simulation and experimental literature data on the effect of calcium-to-silicon ratio on C-S-H's (a) water content and (b) basal spacing. While ¹H NMR, TGA, SANS, sorption, and drying experiments shed light on C-S-H's water content, the experimental measurements of the basal spacing are based on the XRD technique.

predict the exact amount of water content and hydroxyl groups in the C-S-H without calibration factors.

The atomistic simulations have also been used to predict the basal spacing of C-S-H in the NPT ensemble. The C-S-H's molecular structure, i.e., defect content and geometry and interlayer calcium content, strongly affects such sensitive calculations. As shown in Fig. 7b, the experimental literature based on the peak assignment in XRD measurements shows that C-S-H's basal spacing decreases with increasing Ca/Si [222,223,226-231]. By combining high-pressure XRD experiments and atomistic simulations, Geng et al. [232] explained the reduction in the basal spacing by relating it to the interlayer spacing region's densification. In preparation to study the impact of water on C-S-H's time-dependent properties, Morshedifard et al. [233] performed a careful combinatorial study to quantify the Ca/Si ratio's effect on the basal spacing of defective tobermorite models. In this work, they simulated 1000 configurations at each Ca/Si ratio. To avoid metastable configurations, they applied volumetric stress cycles to densify C-S-H's interlayer spacing. As presented in Fig. 7b, they found that the basal spacing decreases when including more defects in C-S-H's silica chains, i. e., removing SiO2 groups, in agreement with experiments. However, when they inserted Ca(OH)2 in the interlayer of C-S-H, they found that the interlayer distance increases. These results suggest that an intricate combination of SiO2 removal and Ca(OH)2 addition might produce realistic C-S-H structures to meet the basal spacing requirement.

3.2.2. Water content in interlayer space and gel-pore space versus RH with the constant basal space $\,$

3.2.2.1. Interlayer water. For C-S-H at the equilibrium pore size (clength of 23.69 Å), GCMC simulations at 300 K show that, under desorption, the interlayer water content remains roughly constant from 100% to 20% RH, then water content slightly drops in the range of 20%to 1% RH, followed by a steep decrease in the water content for RH below 1% [40]. For slit pores with an increment of 10 Å (i.e., a simulation box with a c-length of 33.69 Å), they observed similar trends, with a drop in water content more pronounced for RH below 10%. Under adsorption, they observed no significant hysteresis in all cases from 0 to circa 1% RH. In contrast, they observed hysteresis in the range 1 to approximately 20% RH, and this hysteresis is more pronounced in the case with a larger interlayer pore. They performed their simulation at constant volume, so no volume adjustment or even collapse and reopening of the interlayer space upon sorption can be observed. In the case with equilibrium pore size, the system remains filled with water at low RH. In the slit pores with an increment of 10 Å, they observed cavitation for RH below 15% with a water bridge formation between the adsorbed water layers on the two pore walls. This water bridge disappears at RH below 5%.

Pinson et al. [147] also show the sorption isotherms of interlayer water in C-S-H, and its drying starts below 15 to 25% RH. With rewetting, water reenters the interlayer continuously over almost the full RH range, as inspired by Feldman and Sereda [32]. In their work, Pinson et al. [147] calculated the sorption isotherms of interlayer water under

fixed basal spacing of C-S-H. However, as Pinson et al. pointed out [147], the water amount in interlayer space affects the basal spacing. Morshedifard et al. [233] calculated the relationship between density and basal spacing of C-S-H as a function of H/Si ratio without information of equilibrium relative humidity, and it revealed that the defective C-S-H shows the change in basal spacing from 1.5 to 1.0 nm with changing of H/Si from 4.3 to 0.8.

3.2.2.2. Gel pore water. Based on the calculation by Bonnaud et al. [40], the charge balancing Ca²⁺ ions in the interlayer is the origin of the cohesion of mono C-S-H layers as confirmed experimentally by Plassard et al. [182]. An isotropic pressure changes the basal space, and compressive stress makes basal space short [145]. The mono-C-S-H layers construct gel pores, whose slit size is larger than 0.5 nm. Bonnaud et al. [40] calculated the sorption isotherms and interaction forces between the mono C-S-H layers of gel pores. They presented the sorption isotherm with 1.0 nm width of gel pores, and found that the pore was filled with water at 18% RH, started to dry at 15% RH, and showed the cavitation under desorption branch at the 8% RH. Due to the surface roughness, capillary condensation is gradual when relative humidity increases. Interestingly, the desorption branch is very close to the interlayer water behavior proposed by Feldman and Sereda [32] and Pinson et al. [147], while the capillary condensation of the adsorption branch is much faster than those.

Using mesoscale simulations, Zhou et al. [234] showed that structural relaxation due to capillary (eigen)stresses arising from moisture changes results in hysteresis on water sorption isotherms. This simulation captures the main features of water vapor sorption experiments on cement pastes. The mechanism proposed by these authors to explain the hysteresis loop is the metastability of ink bottleneck states on desorption due to the constrictions in the pore structure of cement paste. In this framework, the pore size distribution plays a crucial role in the capillary forces' manifestation. The largest capillary stresses were observed at the closure point of the hysteresis loop (under desorption) and associated with the menisci at the gel pore / capillary pore interface. Irreversible particle rearrangements are associated with these stresses.

3.2.3. Basal space change as a function of H_2O/Si (or water content) The drying shrinkage corresponds to the microscopic and nanoscopic

porosity redistribution in the C-S-H gel upon water loss via drying. A proxy to better understand this mechanism is to study how an increase in the interlayer water content modifies the basal spacing (see Fig. 8a). In atomistic simulations, water molecules are adsorbed between calcium silicate layers, and the structure is subsequently relaxed to accommodate the increase in the basal spacing. Hou et al. [194] and Morshedifard et al. [233] perform such adsorption relaxation simulations for C-S-H and Honorio [145] for tobermorite. These simulations unequivocally reaffirm that the average distance between C-S-H layers should decrease in response to drying at low relative humidity levels. The slopes of basal spacing increase from 1.0 Å/(H₂O/Ca) to 2.5 Å/(H₂O/Ca). Such slopes are much greater than those expected based on macroscopic drying shrinkage measurements. For instance, Pinson et al. [147] needed to introduce a scaling factor of 0.07 to explain macroscopic shrinkage from microscopic calculations. In fact, not all drying shrinkage deformations occur at the interlayer spacing scale, as shrinkage might also entail reorientation and stacking of C-S-H layers [235] at the mesoscale. Otherwise said, drying shrinkage can redistribute the C-S-H gel's porosity. Several authors concluded that the drying-induced pore structure evolutions occur at a constant total pore volume [12,91,125,127,132,236,237]. Therefore, to provide a more consistent picture of drying shrinkage, we need to consider C-S-H's multiscale porosity, which will be discussed briefly in Section 5.1.

3.2.4. Temperature

Temperature affects the structure of C-S-H and the resultant thermophysical properties. Honorio [145] calculated the impact of temperature on the basal spacing of wet tobermorite. He found that increasing temperature under saturated conditions does not significantly affect the stable basal spacing of tobermorite between 290 K and 330 K. In a more extensive T range, simulations by Bonnaud et al. [148] in drained conditions showed that increasing temperature reduces the C-S-H's water content (i.e., dehydrates C-S-H) and increases the C-S-H's density. Experimental data gathered at the interlayer scale of C-S-H, tobermorite, or jennite [238–240] confirm these trends. Indeed, the water content decreases with an increase in temperature. Two discontinuities are also observed, which correspond to a reduction of water density (at $\sim\!328$ K) and the nucleation of gas bubbles (at $\sim\!422$ K) in the slit pore.

Regarding the coefficient of thermal expansion (CTE), Qomi et al.

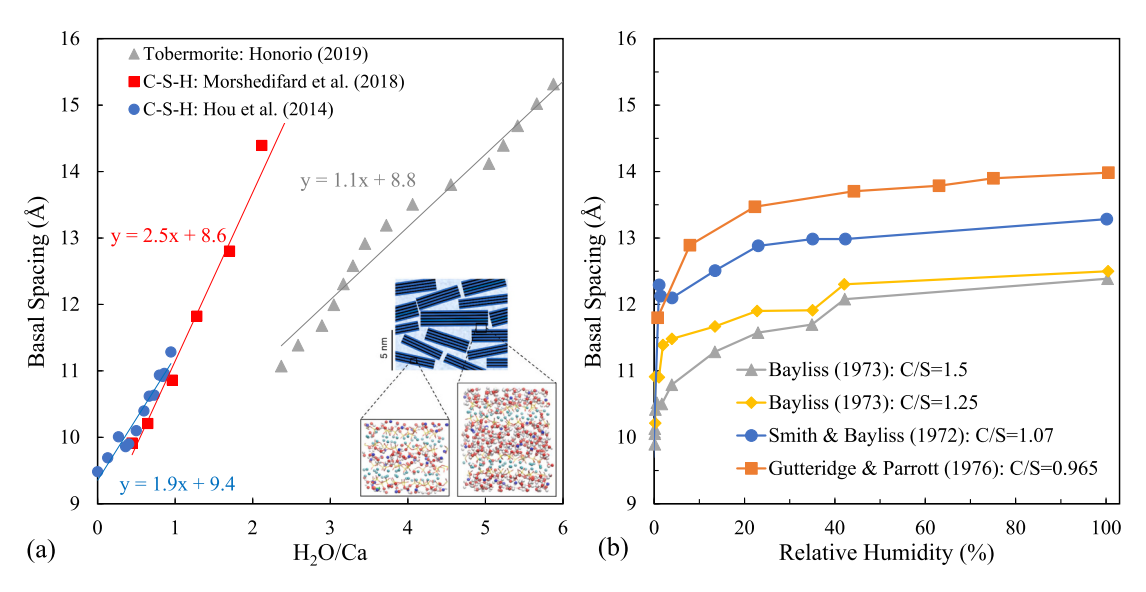


Fig. 8. Collection of simulation and experimental data on the water- and RH-dependence of the basal spacing. (a) Collection of literature simulation data on the dependence of C-S-H's basal distance on the water-to-calcium ratio. While Hou et al. [194] and Morshedifard et al. [233] performed simulations on defective tobermorite at Ca/Si = 1.7, Honorio [145] performed GCMC calculations in tobermorite slit pores. The linear fits and their respective equations are provided for quantitative comparison. The inset demonstrates that different basal spacings can correspond to interlayer spacing and the gel porosity. (b) Collection of experimental data on RH-dependence of basal spacing in C-S-H samples of various Ca/Si ratio.

[211] computed the CTE for C-S-H with Ca/Si of 1 and 1.75 using a finite difference approach. Krishan et al. [241] observed an increase in the CTE when the Ca/Si ratio exceeded 1.5. The authors related this phenomenon to the increase in the water confinement in the C-S-H nanostructure. Bonnaud et al. [148] performed simulations in which they varied the temperature while keeping the fugacity constant: they calculated large negative values (-11 to $-14 \times 10^{-5} \, \mathrm{K}^{-1}$) of the C-S-H particle's CTE between 300 K and 600 K, which correspond to a shrinkage of the C-S-H particle with an increasing temperature. In contrast, Qomi et al. [211] for C-S-H and Honorio [145] for tobermorite both find positive CTE when the water content is held constant instead of the fugacity. This 'undrained' CTE depends on the temperature and whether the temperature increases or decreases; its value is in the range 39–57 10^{-5} K⁻¹. Reproducing perfectly homogeneous constant fugacity or constant interlayer water content is not possible experimentally. But a transition from thermal expansion to thermal contraction is observed in experiments: tests on samples of moderate sizes and short times, i.e., approximately undrained, report thermal expansions, whereas tests on small samples over long times, i.e., approximately drained, report thermal contraction. Several authors observed the combined effect in which the subsequent contraction under the heating process follows the expansion [242-244]. Nevertheless, macroscopic CTE values reported for hardened cement paste are of much smaller magnitude, a few 10⁻⁵ K⁻¹. This difference suggests that the link between C-S-H CTE and macroscopic CTE is not direct but requires further micro-mechanical investigations at intermediate scales. Note also that some experiments report both thermal expansions and contractions; for instance, Cruz and Gillen report positive CTE between 300 K and 450 K, around 1.5×10^{-5} ${
m K}^{-1}$, and negative CTE between 450 K and 600 K, down to about -2.5 imes $10^{-5} \, \mathrm{K}^{-1}$ [245]. The fact that the hardened cement paste does not reach equilibrium during the measurement can probably explain this observation [244]. Higher temperatures can facilitate faster equilibrium, which would imply that measurements at low temperatures would correspond to the mostly undrained response. In contrast, measurements at high temperature would correspond to the mostly drained response.

3.3. Impact of water content on mechanical and physical properties

The presence of water directly affects the layers' cohesion in nanolayered materials, impacting the materials' various physical properties. We discuss key insights in the following, in particular for C-S-H.

3.3.1. Mechanical properties

Using molecular simulation, Hou et al. [246] observed that the Young's modulus and the tensile strength of C-S-H decrease with the water content. Bonnaud et al. [40,148] quantified how the intra- and intergranular forces change with the relative humidity and temperature variations. The intergranular cohesion shows a moderate decrease in which the RH decreases from 100% to approximately 50%, then a more pronounced increase when the system goes from 20% to 0% RH. The intergranular cohesion is stable in the range of 20% to 100% RH and decreases from 20% to 0% RH. These observations may partly explain the decrease in cement-based materials' mechanical strength in very dry environments or at high temperatures (note that microcracking is often evoked to explain that reduction in mechanical properties).

3.3.2. Thermal properties

C-S-H's heat capacity has been computed using lattice harmonic approximation and phonon with methods based on GULP in-built strategy [211] or fluctuations [148]. The heat capacity of water confined in C-S-H is four-fold smaller than the bulk value [211]. Qomi et al. [211] also provided the thermal conductivity of C-S-H with a Ca/Si ratio equal to 1 and 1.75 and an analysis of the vibrational density of state.

Coupling properties such as the coefficient of thermal expansion (CTE) (as commented in the previous section) and apparent Biot coef-

ficient have been computed using molecular simulation. The apparent Biot coefficient b can be computed from a series of GCMC simulations with imposed various water pressures P_W using the definition $b = -\left(\frac{\partial P}{\partial P_W}\right)_d$ [247]. Confinement changes the transfer of the fluids' pressure to the solid. The apparent Biot coefficient of adsorbing materials might be larger than 10 or even negative, as observed in confined Lennard-Jones fluids and liquid water in clay [247] and C-S-H [145].

3.3.3. Mass transport properties

Various authors deployed equilibrium MD to study the dynamics of water and ions in C-S-H. Under confinement in a slit pore, the parallel component of the self-diffusion coefficient is expected to decrease [248]. The perpendicular component is expected to exhibit an anomalous subdiffusive behavior (i.e., D scaling as t^{α} with α <1, instead of a Fickean regime with $\alpha = 1$) [249,250]. Water confined in clay's and C-S-H's micropores has been called, respectively, "glassy" [174] and "supercooled" [251]. Profiles of water self-diffusion coefficient show that closer to the C-S-H pore walls it is drastically reduced [176]. Diffusion in C-S-H micropores is also heterogeneous due to adsorption processes and hopping sites [210]. The MD simulation outputs (such as the mean square displacement of individual particles, Van Hove space-time correlation function, and non-Gaussian parameter) provide a complete picture of confined diffusion inhomogeneity [155,174]. Capillary effects and forced flows can be simulated using non-equilibrium MD. Hong et al. [252] simulated capillary adsorption in an initially empty C-S-H slit pore (3.5 nm undeformable channel) using MD. These authors observed water transport rates in agreement with the Lucas-Washburn equation in classical capillary adsorption theory. Botan et al. [253] deployed Non-Equilibrium MD to study hydrodynamics in clay micropores: for slit pores larger than 3 nm, they observed the parabolic velocity profiles expected from "macroscopic" Navier-Stokes, but they needed a slip boundary condition. Honorio and Abahri [254] obtained similar results for tobermorite but with a larger slip length attributed to the tobermorite layers' surface roughness.

3.3.4. Electromagnetic properties

Probing the electrical and dielectric properties of cement-based materials is useful for non-destructive testing and evaluation. These properties depend on pore size [255]. The frequency-dependent response of the electrical conductivity and dielectric permittivity can be calculated from the Fourier transform of the signal obtained in the molecular simulations. Using MD simulations, Masoumi et al. [187] showed that the (static) dielectric constant of water confined in C-S-H is roughly one-tenth of the bulk value for slit pore size approximately 0.5 nm thick. The dielectric constant of water increases with the pore thickness tending to the bulk value at a pore thickness exceeding 5 nm.

3.3.5. Time-dependent properties

Creep is also one of the major intrinsic reasons for the deformation of concrete under load, and it is a nanoscale process affected by adsorptionrelated phenomena. To analyze C-S-H's creep behavior, Morshedifard et al. [233] applied an incremental stress-marching technique. The calculated creep compliance of C-S-H as a function of H/Si was close to the experimental data obtained by nanoindentation. The computed transition of behavior from purely exponential to a combined logarithmic-exponential of the creep's progress proved that each individual C-S-H globule(/block/grain) behaves viscoelastically. Interestingly, interglobular water caused logarithmic creep behavior. They confirmed the hypothesis that the creep of hydrated cement-based materials originates from the rearrangement of C-S-H globules at the mesoscale rather than the sliding of the individual C-S-H sheets over each other. Several authors confirmed experimentally that C-S-H's creep depends on relative humidity (or on the water content in interlayer and gel pores) by performing microindentations on materials equilibrated at

various RH. In combination with a multi-scale analysis, Suwanmaneechot et al. [256] did it by indenting cement pastes and Chen and Sorelli [257] by indenting tobermorite and jennite.

3.4. Moisture-induced swelling of phases other than C-S-H

3.4.1. Alkali-silica reaction (ASR) products

Moisture-induced swelling has been evoked as a cause for the expansion observed in concrete structures under ASR damage. MD methods provided the hydration energy and isosteric heat of hydration of kanemite (a crystalline product deemed to share similarities with crystalline ASR products) with various cationic substitutions (K, Na, Ca, and Li) [184]. The kanemite hydration energies and enthalpy of adsorption depend on the cationic isomorphic substitutions [184]. Some recent studies on crystalline ASR products [183,258] employ shlykovite structure, reported to represent better the atomic structure of crystalline ASR products [259]. Those studies used MD and GCMC simulations to provide hydration energies and enthalpy of adsorption at controlled water content, potential of mean force (PMF) in saturated conditions, and adsorption isotherms. Volume and water content stability was observed in K- and Na-shlykovite under sorption with no significant hysteresis, in agreement with experimental results [260].

3.4.1.1. AFm. Calcium aluminate mono-sulphate hydrates (AFm) phases are hydrated compounds with a layered double hydroxide structure: positively charged calcium aluminate-ferrite hydroxide layers sandwich water and an anion layer. Various anions may occur in AFm phases relevant to cement-based systems (OH-, NO3-, SO24, CO3-, Cl-, $AlSiO_8H^{8-}$, Kuzel salt in which interlayer with SO_2^{-4} and Cl^- are intercalated). The main AFm formed in cement-based systems is the monosulfoaluminate, which presents the Ms14, Ms12, Ms10.5, and Ms9 hydration states (with the notation Ms.(6 + n), where n is the interlayer water content per Ca₄Al₂) [261]. Molecular simulations show that the monosulfoaluminate's elastic moduli are reported to increase with the water content (n + 6) = 8 to 12 and remain approximately stable for (n + 6) = 8+ 6) of 12 and 14 [262]. The density remains constant with the water content (n + 6) = 8 to 12, then decreases for the MS14 hydration state. Kirkpatrick, Kalinichev, and co-workers studied layered double oxides, especially Friedel's salt, using experimental techniques and molecular simulations [263-266]. Their simulations shed light on the preferential binding sites, their effects on confined water structure and dynamics in AFms [263-265]. The experimental studies show the existence of temperature-induced phase transition in Friedel's salt and hydrotalcite [266], which must still be studied with molecular simulations.

3.4.1.2. M-S-H. Magnesium silicate hydrates (M-S-H) may form in cement-based systems with magnesium sulfate (found, for instance, in groundwater) and in the interface between clayey materials and cement-based materials [267]. The occurrence of M-S-H is associated with low-pH cements (with applications for nuclear-waste encapsulation) [267]. M-S-H exhibits a phyllosilicate-like structure with short-range stacking order with similarities to talc structure [268]. Experimentally, Bernard et al. [269] observed hysteresis under sorption in M-S-H. They evoked water under "confined" and "very confined" states to explain M-S-H behavior. M-S-H has not yet been studied using molecular simulations. A full understanding of the volume stability of this phase can benefit from simulations at the molecular scale.

3.4.1.3. Ettringite. Swelling is one of the mechanisms proposed to explain the durability problems related to ettringite (delayed) formation. Ettringite is not a layered material but a mineral composed of calcium oxide columns with zeolitic micropores in-between these columns. Water and sulfate ions occupy these micropores. Ettringite exhibits a large hysteresis under sorption [270], which has not yet been studied using molecular simulations. This hysteresis is essential in

applications such as using ettringite for thermal energy storage [271,272]. The water content in ettringite ranges from 24 to 27 water molecules per Ca_6Al_2 . The density increases linearly with the water content, and the elastic properties also vary with the hydration state [262,273]. At RH < 10%, ettringite converts into metaettringite (with 10–13 total water per Ca_6Al_2), for which Zhou et al. [274] reported a more disordered structure. Ettringite-metaettringite transition is reversible under sorption. It also occurs under temperature control (being reversible in a particular domain of RH and T). We still poorly understand the mechanisms associated with ettringite-metaettringite transition.

4. What else could be learned from molecular simulations regarding drying shrinkage of cement paste: an example from other materials

4.1. Drying shrinkage of other hydrophilic layered minerals

Recent progress in the molecular structure of C-S-H points to a nanoscale structure made of defective mineral layers separated by an interlayer containing water and Ca counterions [150,155] (see Fig. 9). Defects in the layers cause an amorphization of the structure. Still, the layering remains significant and strongly affects the mechanics, especially at large interlayer distances (high water content), for which solvation forces dominate cohesion [144,40]. A limit case of C-S-H with a Ca/Si ratio of 1 and a high water content is tobermorite, the closest crystalline analog of C-S-H. Tobermorite is a layered material made of crystalline layers separated by interlayer water (see Fig. 9). Tobermorite is part of a broader family of materials, namely hydrated minerals. Hydrated minerals often exhibit a layered structure and cohesion through a hydrated interlayer space. They can include a variable amount of water and are of particular interest concerning hydro-mechanical couplings. Swelling clays in particular have attracted much attention because of their applicative importance in geomechanics and colloidal science. C-S-H and swelling clays share a similar elemental composition, a layered structure at the nanoscale, and similar elementary atomic interactions [275] (e.g., montmorillonite, see Fig. 9). From the fundamental point of view, C-S-H mechanics does not look very different from that of hydrated clays [144,276]. From a macroscopic point of view, though, cement-based materials and hydrated clays differ regarding their formation (chemical reaction vs. pre-existing), their cohesion (strong vs. moderate to low), their stability in freshwater (stable vs. disintegration), and the possibility to perform cationic exchange of the interlayer cation (impossible vs. possible). Like cement-based materials, swelling clays exhibit drying shrinkage, although the magnitude of shrinkage can be much larger. Part of the drying shrinkage (called 'crystalline') is attributed to the interlayer water. The crystalline shrinkage of swelling clays can be addressed at the nanometer scale both experimentally by XRD [277] and theoretically by molecular simulation [185,278]. Consequently, our current understanding of the fundamentals of drying shrinkage in swelling clays has made much progress. Hereafter, we present the physics of drying shrinkage in swelling clays, and we discuss the implication for C-S-H.

The nanoscale interaction between two layers through the interlayer electrolyte governs hydrated layered materials' mechanics (see Fig. 9). The interaction between two charged surfaces separated by an electrolyte is a long-standing issue in colloid science, and the DLVO theory (Derjaguin, Landau, Verwey, Overbeek) is widely accepted to describe such an interaction [279,280]. The DLVO theory treats the electrolyte as a continuum with a static ionic distribution minimizing the electrostatic energy (double layer), which gives rise to an osmotic pressure (repulsion) and an electrostatic attraction. It also accounts for the Van der Waals forces that prevail even in the absence of charges. The overall interaction predicts reasonably well the humidity-induced swelling of low charged minerals (e.g., montmorillonite) at large interlayer distances (> 3 nm) [281]. Such large distances are not relevant for

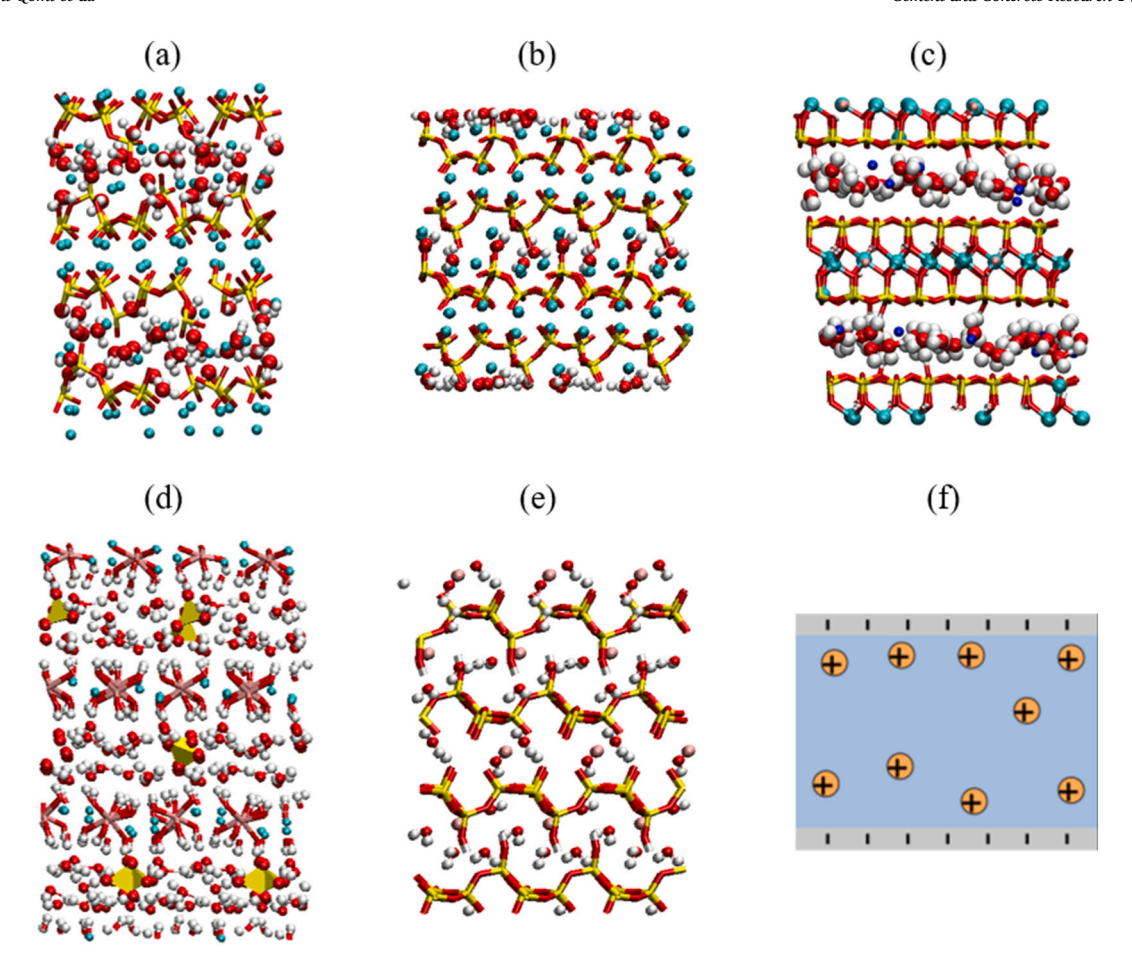


Fig. 9. Molecular models of (a) C-S-H (model of Pellenq et al. [150]), (b) tobermorite (Hamid 11 Å Ca/Si of 1), (c) montmorillonite, (d) monosulfoaluminate, (e) (K-) shlykovite (crystalline ASR product), and (f) idealized case of two charged layers separated by a continuum electrolyte.

compacted clays or cement-based materials, for which crystalline shrinkage involves interlayer distance smaller than 1 nm (two to three water molecules thick). As the interlayer distance decreases, additional contributions to the interaction become significant. Let us mention the finite size of electrolyte molecules, the hydration forces, and the ion correlation forces. Much effort has been dedicated to improving the DLVO description with these additional contributions. Still, for interlayer distances below 1 nm, using a full atomistic description becomes necessary to capture the interaction correctly [144] (e.g., the interlayer ions lose part of their hydration shell, the solid surfaces constrain the water structure and dynamics highly).

The literature about atomistic modeling of swelling clays hydration is much more numerous than for cement-based materials. It dates back to the 1990s [282] (mostly because the layers are crystalline and not defective as for C-S-H). The phenomenon of drying shrinkage at the layer scale can be understood by following the disjoining pressure isotherm's evolution versus the relative humidity [278]. Fig. 10 illustrates this evolution for Na-montmorillonite (results obtained following the method of Honorio et al. [188] but in the undersaturated domain). The isotherms of Fig. 10 are computed during GCMC molecular simulation, i. e., the water content is fluctuating to maintain osmotic equilibrium with an external reservoir of water vapor. The disjoining pressure is defined

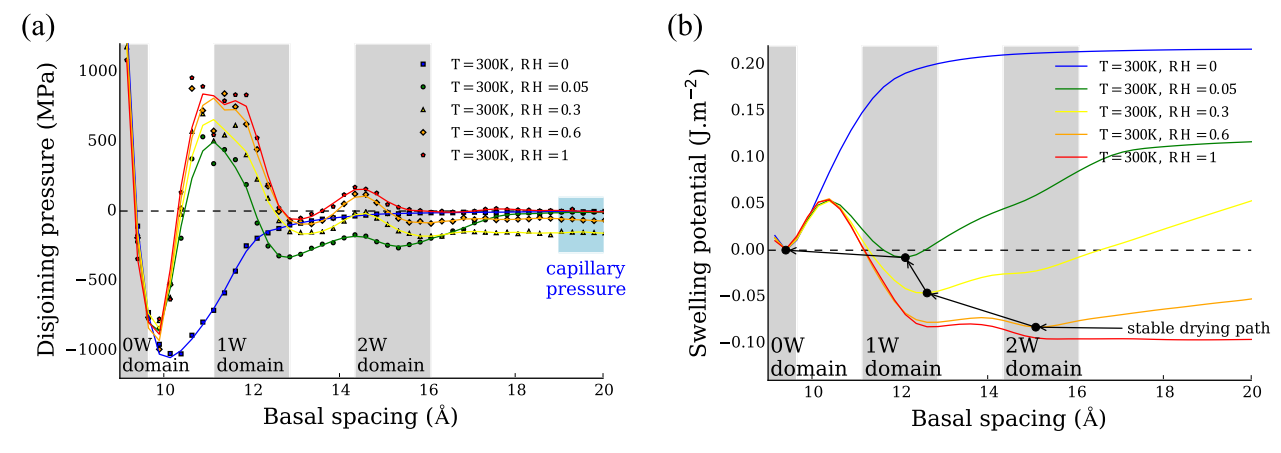


Fig. 10. (a) Disjoining pressure isotherm of Na-montmorillonite (surface charge: -0.124C/m²) versus relative humidity, (b) corresponding swelling potential.

as the difference between the actual pressure exerted orthogonal to the mineral layers and the bulk fluid pressure (reservoir fluid) in osmotic equilibrium with the porous medium: $P_{dis} = P - P_{bulk}^{fluid}$. It quantifies the layered porous medium's mechanics in the direction orthogonal to the layers, at thermal and chemical equilibrium with the water vapor. In a capillary pore, the disjoining pressure is the capillary pressure. But the disjoining pressure deviates from the capillary pressure for interlayer thickness below 1 nm (see Fig. 10 and Section 1.3). Interestingly, the disjoining pressure isotherm is non-monotonous versus the basal spacing, i.e., a pressure can correspond to multiple basal spacings. Such a degenerate situation is an unusual behavior in mechanics and requires a proper thermodynamic analysis. Integration of the disjoining pressure versus the basal spacing provides the so-called 'swelling potential' ω

$$-\int\limits_{-}^{e}P_{dis}de$$
, that is, the thermodynamic potential per unit area of the

layer, minimum when $P=P_{bulk}^{fluid}$. $P=P_{bulk}^{fluid}$ corresponds to a situation where the layered medium is immersed in the vapor and free to deform. One can easily generalize to the case where any prescribed pressure $P_{control}$ is imposed on the layered medium by considering the alternative definition of disjoining pressure $P_{dis}{}'=P-P_{control}$. In the particular case of $P_{control}=0$, one recovers the effective interaction energy between clay layers (see Section 2.1).

Fig. 10b displays the swelling potential isotherms. Thermodynamic stability requires the swelling potential to be a convex function of the basal spacing. More precisely, the convex envelope of an isotherm corresponds to the stable configurations, and the convex portions that are not part of the convex envelope are metastable. Thus, only the decreasing branches of a disjoining pressure isotherm correspond to (meta)stable configurations; and determination of the stable configurations requires analyzing the swelling potential. We can identify three (meta)stable 'domains' in the isotherms. Detailed observation of the corresponding molecular configurations shows that these domains are associated with a structuration of the interlayer water at the smallest pore sizes: two water layers (2 W domain), one water layer (1 W domain), and dry states (0 W domain). XRD experiments confirm that we can only observe some specific ranges of basal spacings, and the measured ranges compare well with those predicted by molecular simulation [277]. Interestingly, the ranges of basal spacing of the xW domains are almost insensitive to the relative humidity change, but the corresponding disjoining pressures evolve significantly, which affects the stability analysis. In particular, as RH decreases, the global minimum of the swelling potential changes from the capillary domain to the 2 W. 1 W, and ultimately 0 W domain, i.e., following the most stable configuration, drying shrinkage is expected (see Fig. 11). In case of metastability, which is likely in geological conditions [283], one could

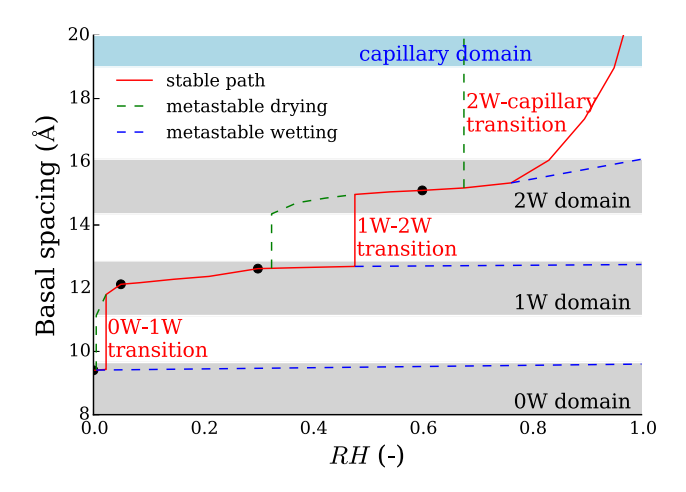


Fig. 11. Drying shrinkage of Na-montmorillonite obtained by thermodynamic analysis of the disjoining pressure isotherm of Fig. 10.

follow part of the metastable branches from the stable hydration transition to the spinodal points (extrema of the disjoining pressure isotherm). Metastability causes hysteresis in the drying shrinkage and adsorption isotherms (see Fig. 11). Interestingly, shrinkage versus water content does not show hysteresis, which means that the two hystereses originate from the same irreversibility. This thermodynamic analysis provides the basis for understanding the drying shrinkage of clays and its hysteresis. Many in the literature have investigated application to different clay types, counterions, surface charges, or other layered media with other fluids [284]. Molecular simulation can provide valuable insight into practical interest; for instance, it explains why some cations can mitigate drying shrinkage of swelling clays (e.g., potassium in montmorillonite [285]).

A significant difference between cement and swelling clay is the surface charge and the nature of the counterion. The equivalent surface charge of C-S-H is about 4 to 8 times larger than that of the Namontmorillonite considered above, and the counterion is the calcium ion, which is divalent (Ca²⁺). Early molecular simulation works on C-S-H cohesion point to the surface charge and the counterion as the central factors that differentiate C-S-H from clay [276,144,180,286]. How surface charge affects the disjoining pressure and swelling potential isotherms is illustrated in Fig. 12. It appears that the fact that the surface charges are large favors lower hydration states and amplifies the energy barriers between hydration states, i.e., it makes it more difficult to overcome meta-stability. This phenomenon explains why hydrated clays with large surface charge (e.g., vermiculite) exhibit little sensitivity to humidity; there are still different hydration states, but the high energy barriers strongly limit hydration transitions. Regarding the counterion ion, the valency strongly affects the osmotic repulsion: monovalent ions exhibit a much stronger osmotic repulsion than divalent ions. Thus, calcium ions appear essential to the cohesion of C-S-H.

Recent results for model C-S-H nanolayers and tobermorite (closest crystalline analog of C-S-H) suggest that, because of the high surface charge, the 0 W state becomes the most stable state at ambient pressure [25,145,187] (see Fig. 13). The 1 W and 2 W hydration states still exist but are expected only for systems under tensile conditions. The magnitude of the tensile strength (pressure well) is 4 to 5 times larger than for montmorillonite. The swelling potential increases monotonously after the 0 W state. Those two observations are consistent with the strong cohesion of cement-based materials. We list in Table 7 the associated cohesive pressure, stiffness, and cohesive energy reported in the literature. Hydration transitions (2 W to 1 W, or 1 W to 0 W) could explain drying shrinkage, but only if the layered medium is maintained under tensile conditions. Such conditions could well occur because of the stress heterogeneities within the cement-based material's matrix (see next section). Only the small fraction of layers under high tension would exhibit hydration transitions, hence a drying shrinkage of smaller magnitude than for swelling clays. These studies of layered C-S-H and analogs provide a first insight into the mechanics in a nanometric pore scale of cement-based materials. Still, more accurate results are needed, and additional investigation is necessary to get a full picture of the hydromechanics of C-S-H. The defects in the layers (amorphization), the intragranular water, the heterogeneities in the surface charge of C-S-H, or shear are all topics of importance regarding the fundamentals of drying shrinkage, but current studies do not address them.

4.2. Is it essential to take into account the microstructure's deformability to correctly estimate water content?

The issue of adsorption-induced deformation is not limited to cement or hydrated minerals, but it is relevant to a wide variety of porous media and fluids. Let us mention microporous carbons (coal, activated carbons) and organic polymers in general in the presence of organic fluids. Or cellulose and other hydrophilic polymers in the presence of water. Or microporous and mesoporous silicate (zeolites, aerogels) with a wide variety of adsorbates. Accordingly, in the adsorption community, much

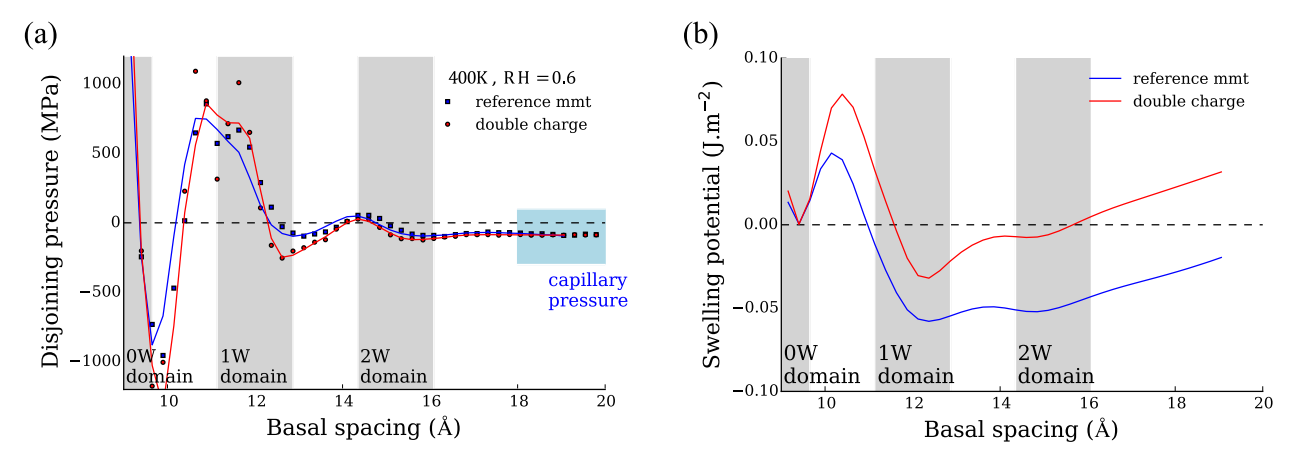


Fig. 12. Effect of surface charge on the (a) disjoining pressure and (b) swelling potential isotherms.

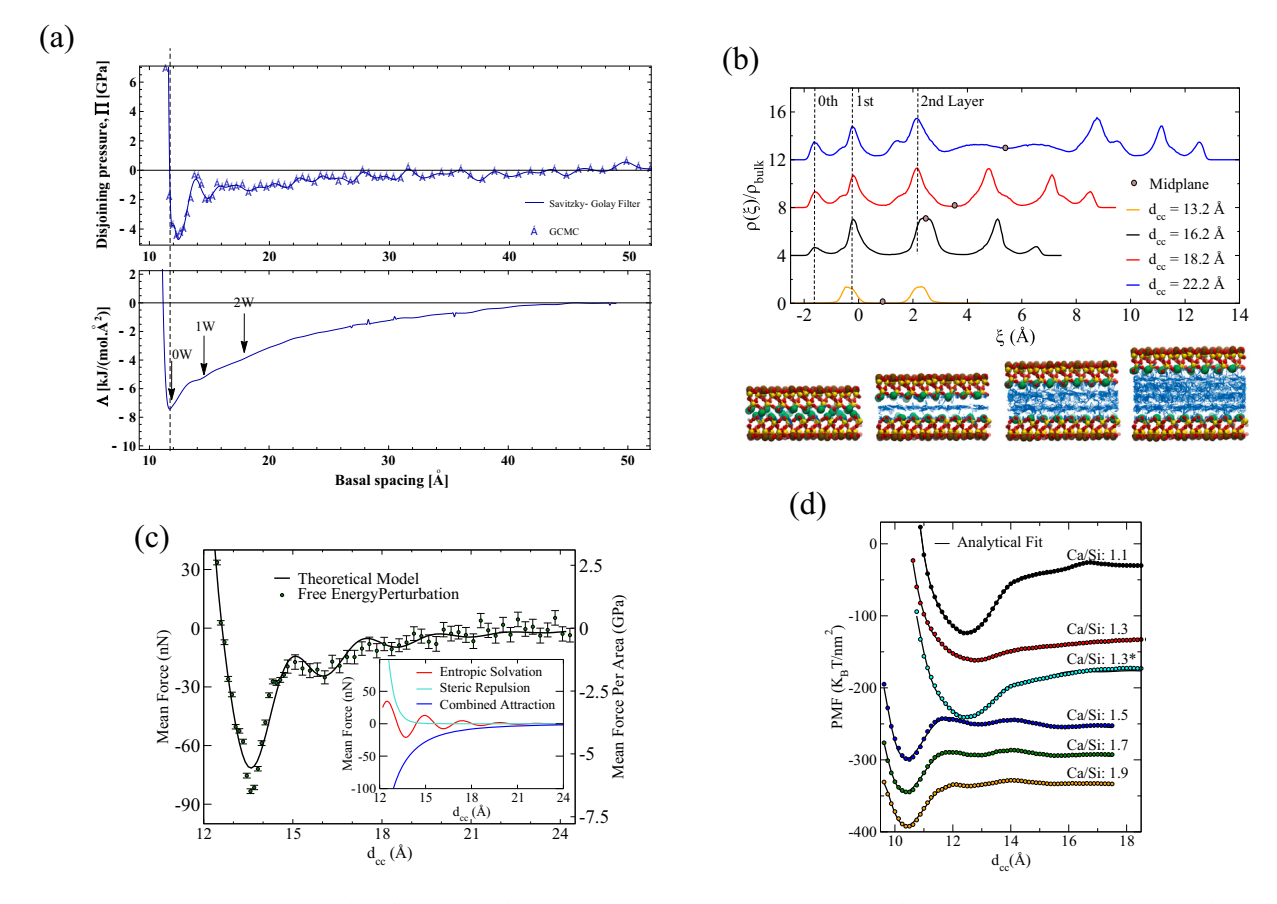


Fig. 13. (a) Disjoining pressure and associated swelling potential of tobermorite [145]. (b) water density profiles, (c) mean force, and (d) potential of mean force between nanolayer models of C-S-H [25]. The mean force is equal to the disjoining pressure times the nanolayers' area, and the potential of mean force is equal to the swelling potential [187]. Reprinted with permission from [145] [25] [187]. Copyright (2017 and 2019) American Chemical Society.

effort has been dedicated to studying adsorption-induced swelling and shrinkage. In that respect, the possibility to synthesize porous media with highly controlled porosity (size and shape) at the nanometer scale has provided ideal benchmarks for the theory [294]. It is now well accepted that the disjoining pressure is the appropriate thermodynamic concept to address the mechanical pressure induced by adsorption in a single pore of controlled size. Note that one can adapt the concept of disjoining pressure to pore shapes that are not slits. However, for amorphous media with micropores that can accommodate only a few molecules (e.g., C-S-H, see Fig. 9), the concept of pore size and pore surface becomes questionable. In such microporous media, the very

definition of disjoining pressure becomes ambiguous. A proper thermodynamic description of such situations cannot distinguish a volume occupied by the fluid phase and a volume occupied by the solid. An alternative theoretical approach is needed. Such an approach was developed in the context of amorphous polymeric media (e.g., natural carbons, cellulose), starting from the thermodynamic framework of poromechanics [295]. This theory relates the adsorption-induced pressure to the adsorption isotherm directly, according to the expression [296–298]:

Table 7

Equilibrium stable basal spacings of calcium silicate hydrates (C-S-H, tobermorite) and properties computed from simulation under volume control compared against experimental data. Note that some values from the literature for the surface energy are presented as two surfaces. These values are corrected for comparison here.

Ref.	d ₁ (d ₂) [d ₃] (Å)	$egin{aligned} E_{zz} &= & & & & & & & & & & & & & & & & & &$	P _{co} (GPa)	$\gamma_s = -rac{1}{2}\int\limits_{d_0}^{\infty} \langle P angle d(d_c) \ (\mathrm{J/m^2})$
Brunauer et al. [287,288] ^a Plassard et al. [182] ^a Pellenq et al. [289] Shahsavari et al. [290] Oh et al. [291] ^a Oh et al. [292] ^a Bauchy et al. [293]	12.5 (14.3) [16.1]	- - - 68.4 61 89	- 0.93 5.0 - -	0.32-0.4 - - - - - 0.53
Bonnaud et al. [146] Masoumi et al.	11.4	42.28	0.95	
[25] ^b Masoumi et al. [202] ^b	13.5 (15.9) 12.1	77.6 77.6	6.5 5	0.67
Honorio [145] $(T = 290 \text{ K})^b$ $(T = 300 \text{ K})^b$ $(T = 310 \text{ K})^b$ $(T = 320 \text{ K})^b$ $(T = 330 \text{ K})^b$	12.6 (15.7) 12.6 (15.7) 12.6 (15.7) 12.6 (15.7) 12.6 (15.7)	60.9 61.5 60.9 77.4 75.7	4.19 4.17 4.23 4.19 4.15	0.61 0.6 0.585 0.58 0.57
Masoumi et al. [187] (Ca/Si =1.1) (Ca/Si =1.3) (Ca/Si =1.3°) (Ca/Si =1.5) (Ca/Si =1.7) (Ca/Si =1.9)	12.5 12.9 12.5 10.4 (13.0) [15.7] 10.4 (12.9) [15.5] 10.4 (12.6) [15.4]	73.56 26.15 52.3 102.43 81.74 89.58	2.9 0.9 1.9 3.7 3	0.3473 0.1065 0.2511 0.1716 0.1905 0.2189

^a Experimental.

$$P_{ads} = \frac{\partial}{\partial \varepsilon} \left[\int_{-\infty}^{\mu} n(\varepsilon, \mu) d\mu \right]_{\mu}$$
 (7)

where $\varepsilon = V/V_0$ is the Lagrangian volumetric strain of the medium (V_0 is the reference volume corresponding to the unstressed configuration in the absence of fluid), and $n(\varepsilon, \mu) = N/V_0$ is the fluid content. The integral in Eq. (7) corresponds to the variation of the (fluid + solid) system's grand potential due to the fluid's introduction at constant deformation. This expression, obtained by thermodynamic integration, is very general, and the only underlying assumption is that the state parameters controlling adsorption are limited to the volumetric deformation ε and the chemical potential μ of the fluid. In particular, one does not need to define any pore volume or specific surface; one needs the fluid content only. Note, however, that the fluid content is a function of both chemical potential and deformation. How adsorption depends on the deformation is often disregarded in the adsorption community, but it appears critical here. One of the most simple illustrations of the above theory is a fictitious 1D porous chain [295] (see Fig. 14). The porosity of this fictitious medium is amorphous in the sense that pore sizes are randomly distributed. Complete characterization by GCMC molecular simulation shows the validity of the extended poromechanics theory (Eq. (7)).

Although the overall adsorption-deformation coupling looks simple (e. g., fluid content linear with strain), the local behavior is highly heterogeneous with local pore contractions or expansions up to one order of magnitude larger than the overall deformation. This simple system may seem irrelevant for real materials. Still, it proves very insightful to understand and model adsorption-induced deformations in disordered carbons with no specific pore sizes (e.g., coal) [295,299]. Moreover, local deformations' significant heterogeneity shows that it is critical to consider the solid structure's flexibility; doing so is not standard in the adsorption community.

One can use the above theory to study drying shrinkage. Assuming constant compressibility κ of the solid skeleton, the magnitude of adsorption-induced deformation for a material submitted to an external loading $P_{control}$ is the quantity $(P_{ads} - P_{control})\kappa$. Accordingly, high adsorption-induced pressure P_{ads} , which corresponds to an adsorption isotherm that increases significantly with strain, favors drying shrinkage. 'Significantly' should be understood compared to the fictitious amount of bulk fluid that would occupy the porous medium's volume. Indeed, if one immerses the medium in the vapor, the external

loading is the pressure of the bulk fluid, which one can write $P_{control}$ =

$$P_{bulk}^{fluid} = \int\limits_{-\infty}^{\mu}
ho_{bulk} d\mu$$
 because of Gibbs-Duhem equation (ho_{bulk} is the number

density of the bulk fluid). Thus, the adsorption-induced deformation

would be equal to
$$\frac{\partial}{\partial \varepsilon} \left[\int\limits_{-\infty}^{\mu} (n - n_{bulk}) d\mu \right] / \kappa$$
 with $n_{bulk} = \varepsilon \rho_{bulk}$. n_{bulk} cor-

responds to the change with deformation of the fictitious bulk fluid content that would occupy the medium's volume in the absence of the adsorbent. If the actual fluid content increases more rapidly than that of the fictitious bulk fluid, then drying shrinkage is expected. In practice, when the bulk fluid is a vapor, the bulk density is much lower than the adsorbed density ($n \gg n_{bulk}$), so that one expects drying shrinkage. Shrinkage is not a generality, and some system can exhibit counterintuitive adsorption-strain couplings (e.g., $\frac{\partial n}{\partial s} < 0$). An example of application is wood. It is well known from everyday experience that wood significantly shrinks when it dries. The wood's hygroscopic behavior originates from the cellulose's water-induced deformation [193] (see Fig. 15). In amorphous cellulose, a hydrophilic nanoporous soft polymer, one cannot define a pore size or a pore surface unambiguously. Following a similar analysis as above, but taking into account the solid compressibility's evolution with adsorption, one can accurately predict the adsorption-induced deformations [298].

The intragranular porosity of C-S-H exhibits significant amorphization because of the chemical defects in the mineral layers. Therefore, intragranular C-S-H typically falls into this category of porous media, for which one cannot clearly define the porosity. Molecular simulation of flexible C-S-H particles combined with the above theory could address the intragranular drying shrinkage, in principle. Such a study remains to be done and may face other difficulties, such as accessibility to intragranular porosity and equilibration dynamics.

4.3. The adsorbed thickness of water on the solid surface

As explained in Section 1.4, one physical process through which the in-pore fluid deforms cement-based materials is through surface adsorption and the associated Bangham effect (see Eq. (4)) [80]. Modeling this effect requires the knowledge of the thickness of water adsorbed at the surface of the C-S-H gel and capillary pores as a function of the environmental conditions (typically as a function of relative humidity and temperature). The models of Hagymassy et al. [41] and Badmann et al. [42] of this adsorbed thickness are, however, limited to 1 temperature close to room temperature, and there is, therefore, a need

^b Tobermorite.

^c Ca/Si ratio was increased by removing less bridging silica tetrahedra and inserting interlayer calcium (Ca_w) atoms, as Geng et al. proposed [232].

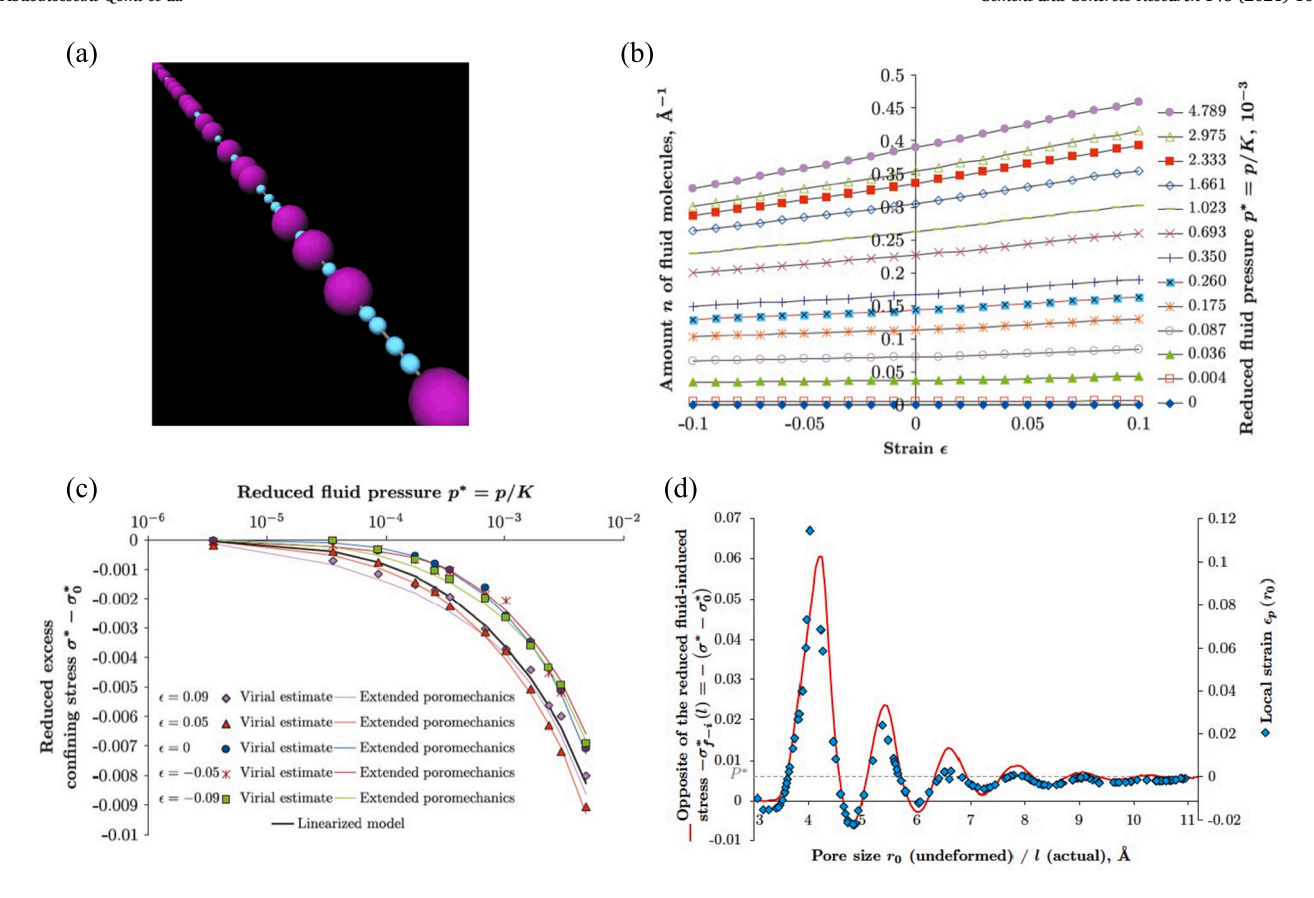


Fig. 14. Illustration of adsorption-deformation couplings in a fictitious 1D porous medium. (a) snapshot of the system, (b) adsorption isotherm versus both deformation and chemical potential, (c) adsorption induced pressure (direct computation vs. application of Eq. (7) to the adsorption isotherms), (d) the heterogeneity of deformation versus the pore size correlates accurately with the disjoining pressure. We obtain the disjoining pressure of given pore size by considering a 1D chain with identical pores.

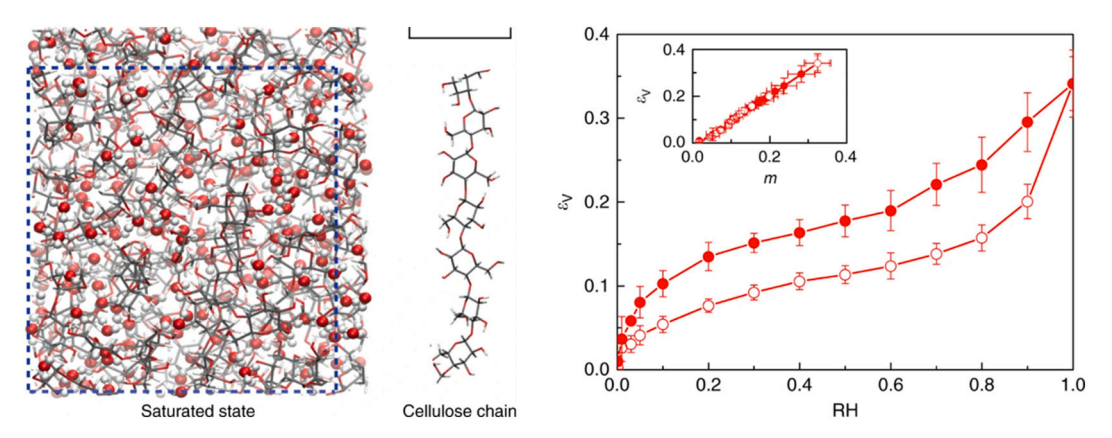


Fig. 15. Drying shrinkage of amorphous cellulose predicted by molecular simulation (Figures from [193]).

for more data at different temperatures.

Obtaining data regarding the thickness of adsorbed water from molecular simulations would be possible. Such data has, in fact, already been simulated, albeit for other systems. Rahaman et al. [300] simulated the water molecules' adsorption on calcite surfaces at room temperature by introducing water molecules drawn from a Maxwell distribution in MD simulations. They modeled relative humidities of 100%, 75%, and 50% by using different collision rates. They obtained the density of adsorbed water molecules at those various relative humidities versus the distance to the solid surface, providing the thickness of the adsorbed layer after integration. For what concerns water adsorption on mica surfaces, both Malani and Ayappa [301] and Cheng and Sun [302]

performed GCMC simulations. They obtained the thickness of the adsorbed film at room temperature over an extended range of relative humidity (namely from 10^{-4} to 98% for Malani and Ayappa [301]). Malani and Ayappa [301] showed that their simulated thicknesses compare very well with experimental data. On top of providing the adsorbed thickness, those molecular simulation studies also provide valuable information regarding the structure or the dynamics of this adsorbed layer.

For what concerns cement-based materials, only very recently was provided a thickness of the adsorbed film of water from molecular simulations: Zare et al. studied the adsorption of water at a relative humidity of about 90% on C-S-H and forsterite surfaces. They showed an

adsorbed water film thickness of ~ 1 nm in agreement with experiments [304]. They furthermore showed that the water nanofilm thickness is not strongly affected by the pressure of the co-injected CO_2 up to 100 bar. Performing such adsorption studies at other relative humidities and temperatures for C-S-H and various phases in the cement paste is the subject of ongoing research. Co-adsorption with various gaseous phases is also studied presently.

5. Drying shrinkage from the atomic scale to the macroscopic scale: limitations and perspectives

5.1. Size limitation and upscaling approaches

An obvious limitation of classical molecular simulations is that the size of the systems that they make possible to study is limited to about a dozen nanometers (see Section 2.2), which is much smaller than the macroscopic scale of interest for engineers. However, various strategies have been used to bypass this limitation and provide information valuable at the macroscopic scale.

One way to inform the macroscopic scale is to feed macroscopic constitutive equations derived in the continuum framework with molecular simulations' results. Pinson et al. [147] do so; they derive a macroscopic model for drying shrinkage that combines capillary effects, surface adsorption effects (i.e., Bangham effects), and volume variations due to variation of the interlayer spacing. In their model, Pinson et al. [147] justify with molecular simulations the existence of a threshold relative humidity below which water starts leaving from the interlayer space. Another example, albeit not for cement-based materials, is the model of Vandamme et al. [305] for deformations of coal induced by surface adsorption. In this model, coal deformation upon injection of CO₂ or pumping of CH₄ is due to variations of the pore's surface energy according to Gibbs' isotherm. The model's required input is the sorption isotherm of the pore fluid on the coal surface: they obtained this sorption isotherm with molecular simulations. As explained in Section 4.3, the molecular simulation of adsorption of water on C-S-H surfaces is the topic of ongoing research.

Another way to move from the molecular scale up to the macroscopic scale is to perform numerical upscaling. Typically, one can upscale results from molecular simulations to inform numerical simulations of a simplified system but performed at a larger scale. Those zoomed-out numerical simulations are named coarse-grained simulations, and the interaction potential between coarse grains is named potential-of-mean-force (PMF). We give examples of such approaches next.

Churakov et al. [191] performed ab-initio DFT calculations of the intrinsic acidity constants of \equiv SiOH and \equiv CaOH $_2$ groups on the C-S-H surfaces. Based on those calculated constants, they proposed a coarse-grained model of the interface between C-S-H and solution, with which they performed GCMC simulations of ion sorption on C-S-H.

Masoero et al. [306] and Ioannidou et al. [307,203] modeled C-S-H in a coarse-grained manner. They represented the C-S-H gel as an assembly of spherical particles interacting through Lennard-Jones potentials [306] or slightly more complex non-oriented pair potentials [203,307] with estimated parameters. Masoero et al. [306] considered polydisperse particles from 1 nm to 10 nm; Ioannidou et al. [307] considered monodisperse particles with a size of about 10 nm; Ioannidou et al. [203] considered polydisperse particles from about 4 nm to 9 nm. Masoero et al. [306] simulated C-S-H precipitation by randomly inserting C-S-H particles in an initially empty simulation box, while Ioannidou et al. [307,203] simulated it by using a hybrid scheme of GCMC and MD steps. From their simulations, Masoero et al. [306] could explore the relationship between elastic stiffness and packing density of the C-S-H numerically; they found good agreement with experimental results obtained by nanoindentation. Ioannidou et al. [307,203] could simulate systems of several hundred nanometers, up to about half a micron: at this scale, they could discuss the heterogeneity of the structure of C-S-H, how this heterogeneity develops during hydration, and its impact on the mechanical properties of the C-S-H gel. They propose that the lower value of the C-S-H's specific surface with N_2 than with H_2O can be due to an adsorbed water film blocking access of the adsorbate to the C-S-H smallest gel pores and interlayer space. Their results also suggest that, but for extreme conditions, drying shrinkage is governed by water in the only pores accessible to their simulations, namely the capillary pores and the largest gel pores.

In coarse-grained approaches, one can also calibrate the interaction potentials between C-S-H grains with molecular simulations' results at a scale below. Honorio [145] and Masoumi et al. [204] used such a method. With molecular simulations in saturated conditions (i.e., at a relative humidity of 100%), they started by calculating free energy landscapes of systems constituted of two parallel C-S-H layers at various distances from each other. Honorio [145] considered face-to-face configurations. Masoumi et al. [204] considered both face-to-face and edgeto-edge configurations [204]. Honorio [145] fitted isotropic PMFs on the free energies calculated, and Masoumi et al. [204] fitted anisotropic ones. They then used them for coarse-grained simulations of the C-S-H gel. While the coarse grains of Honorio [145] were spherical particles, the coarse grains of Masoumi et al. [204] were C-S-H platelets (i.e., each C-S-H layer is a grain). Fitting the PMF directly on results from molecular simulations makes it possible to insert quite complex physics at the mesoscale: for instance, Honorio [145] found that the PMFs are temperature-dependent and could, from his coarse-grained simulations, calculate how the coefficient of thermal expansion of the C-S-H gel depends on temperature. Interestingly, stacks of C-S-H layers with a thickness of about 5 nm naturally come out from the coarse-grained simulations of Masoumi et al. [204], in excellent agreement with the characteristic length observed experimentally in the C-S-H gel (see Section 1.1). While Honorio [145] and Masoumi et al. [204] fitted their PMFs at a relative humidity of 100% (i.e., in saturated conditions), one could readily employ their strategy at other relative humidities. By doing so, one could find out how these PMFs evolve with relative humidity, i.e., during drying and imbibition. Bonnaud et al. [146] did indeed fit anisotropic PMFs between C-S-H layers on molecular simulations results obtained at a relative humidity of 10% for one edge-toface and two face-to-face configurations (among which one turbostratic one). In their fit, they also considered the relative orientation of the two C-S-H layers, to the expense of a more complex PMF than in other studies. This complexity would translate into coarse-grained simulations that would be more expensive, computationally.

On the mesoscale assembly of polydisperse particles representative of the C-S-H gel of Ioannidou et al. [203], Zhou et al. [234,308] aimed at predicting the mechanical effect of drying on the mesostructure numerically. To do so, they introduced a multiscale numerical poromechanical strategy. They first used lattice gas DFT to obtain the water distribution in the structure versus relative humidity. Then, they calculated the stress fields, which they integrated over Voronoi cells around each grain to obtain the capillary forces. Finally, they performed MD simulations under these forces' action to simulate how drying impacts the mesostructure. They showed that drying induced nanoscale irreversibilities, which help relax eigenstresses that prevailed in the C-S-H gel due to the hydration process.

5.2. Some fundamental questions related to drying shrinkage to which molecular simulations could contribute

Despite the decades of research dedicated to better understanding, modeling, and controlling drying shrinkage, and despite the recent advances made possible by molecular simulations and underlined in this review, fundamental questions related to drying shrinkage remain. Molecular simulations could contribute to answering those questions.

As underlined in the review, the sample's macroscopic shrinkage is partly due to the C-S-H gel's alteration during drying. This alteration is partially reversible and partially irreversible during the first drying. It evolves over very long periods (we referred to those evolutions as

'dynamic' evolutions in Section 1.5). However, what happens precisely to the C-S-H microstructure during this alteration remains not fully understood. It is likely that the interlayer calcium ions, which can hydrate with various coordination numbers, plays a crucial factor in this process, which molecular simulations could help elucidate. Molecular simulations can also help assess the effect of temperature on the adsorption of water in the interlayer and on the C-S-H surfaces, and more generally, on the C-S-H's dynamic evolution. The interplay between the solid's flexibility and adsorption could also be addressed to investigate the nanostructure evolution upon drying.

An interesting fact is that only a fraction (i.e., about 5 to 10%) of the C-S-H's volume variation at the nanometric scale (consecutive to its agglomeration during drying) translates into a macroscopic strain, as explained in Section 3.2. Why it is so is unknown. Because of this fact, and because of other reasons (e.g., the sample's heterogeneity), cement paste and concrete contain large amounts of cracks at various scales after drying. However, despite those cracks, the sample mostly keeps its shape, its compressive strength remains primarily unaffected, and the physical properties of similar samples evolve with drying in a reproducible manner. From a physical point of view, how this is possible is not comprehensively answered. Since the C-S-H gel can support considerable compressive stresses, the C-S-H particles' connectivity and the C-S-H layers' flexibility could be fundamental phenomena to explain the hardened cement paste's volumetric stability during drying. Such issues related to the concrete structures' volumetric stability over their life span should be understood and controlled to ensure long-term serviceability.

Drying does not alter only the C-S-H gel but also other hydrates, impacting the macroscopic strains. Molecular simulations can provide information regarding the crystal structure's evolution of some hydrated phases (e.g., ettringite) during drying. A combination of adapted simulation protocols enables following the structural changes related to variations in relative humidity, temperature, or mechanical loading. It also allows quantifying the relative contribution of those various types of solicitation to those structural changes. The tools for quantifying order and disorder (as discussed in Section 2.1) may shed light, for instance, on the main features of the metaettringite structure, whose intrinsic disorder [274] makes it challenging to analyze with experimental procedures. During imbibition, the crystal structure's evolutions can also generate pressures that can contribute to macroscopic strains.

Beyond those questions, drying shrinkage is related to the C-S-H's microstructure and pore structure. Consequently, fundamental questions linked to the microstructure of C-S-H are of interest to better understand drying shrinkage. As described in details in Section 1.5, the very nature of the C-S-H precipitated from ordinary Portland cement remains an unsettled question, with various models proposed for C-S-H and its growth. The chemical composition and structure of C-S-H during its precipitation is not clarified yet. The C-S-H's microstructure is related to the gel pore structure. This gel pore structure is reproducible, but its formation mechanism associated with the C-S-H precipitation is unclear. Gartner et al. [37] suggested that the hydration of Ca ions in the interlayer space plays a crucial role in this formation, but the full picture is still unclear. Regarding the microstructure of C-S-H, the presence of high density and low-density C-S-H also exhibits some mystery. For example, ¹H NMR relaxometry measurement and small-angle X-ray scattering (SAXS) measurement cannot distinguish those two types of C-S-H. Even though some suggest that measurements repeated at various times could, a single measurement performed on a mature sample cannot. In contrast, nanoindentation, scanning electron microscopy (SEM) and transmission electron microscopy (TEM) can distinguish those two types of C-S-H. Additionally, how these two different C-S-H develop during hydration, together with their corresponding pore structures, is not fully understood vet.

Another puzzling aspect of cement pastes' microstructure is that the pore system features (i.e., porosity, specific surface area, pore size distribution) back-calculated from sorption isotherms depend on the fluid

used as adsorbate, as explained in Section 1.5. Why it is so is unclear. Water sorption isotherms exhibit a hysteresis at a low relative humidity (see Section 1.5). Whether this hysteresis is of chemical (i.e., related to hydration [32,309]) or physical [59] origin is debated. On those various questions, molecular simulations could shed new light.

One can also use molecular simulations to quantify how specific ion effects affect drying processes in cement-based materials. Charge balance ions are known to affect the confining pressure and effective interactions of layered materials such as clays (e.g., [310,311]) and crystalline ASR products [258]. Molecular simulation can shed light on the ion exchange mechanisms, ion adsorption, and the repercussion of specific ions on the effective behavior of layered materials in cement-based systems. Such fundamental understanding can also be critical to understanding the ion immobilization capacity of cement-based systems or even the mechanisms driving the formation of AFm phases.

5.3. Perspectives: how molecular simulations could help to mitigate drying shrinkage?

Molecular simulations have already begun assisting researchers with understanding and devising new strategies to mitigate and eliminate shrinkage. For instance, Yang et al. [173] showed experimentally that incorporation of a small amount of nano-ZrO $_2$ eliminates the harmful results of drying shrinkage in sodium-based calcium-alumino-silicate gels (C-(N)-A-S-H). They attributed this to the formation of a silica gel on the surface of nano-ZrO $_2$ upon drying. They subsequently performed a series of Density Functional Theory (DFT) calculations. They showed that a silica monomer binds strongly to the surface of zirconia compared to tobermorite surfaces irrespective of the hydration state and the calcium adsorption on the surface. The proposition of such simulation-informed mechanisms can ultimately open a path forward to minimize shrinkage in otherwise vulnerable construction materials to drying effects by incorporating targeted nanomaterials.

An alternative approach to eliminate drying shrinkage is through modification of the nanostructure of C-S-H (see Fig. 16). Moshiri et al. [312] have recently demonstrated the successful synthesis of crosslinked C-S-H hybrids using a soft chemistry approach that involved hydrolyzing double-functional organosilane molecules. They showed that the organosilane molecules connect the two adjacent calciumhydroxide sheets creating a crosslinked C-S-H (XCSH) analog. Aiming at demonstrating the shrinkage properties of XCSH, Moshiri et al. investigated the effect of drying on the interlayer distance by performing low angle XRD scans (see Fig. 16a). Interestingly, they found that while tobermorite shrinks upon drying, XCSH maintains its basal spacing with no visible shrinkage. Morshedifard et al. [313] performed atomistic simulations to study the structural characteristics of XCSH. They found that the basal spacing is strongly dependent on the grafting degree of calcium hydroxide sheets with organometallic molecules (see Fig. 16b). Their PMF calculations showed that, while the basal spacing can collapse at low grafting percentages, it is difficult to be reduced at high grafting densities as steric repulsion between organic moieties prohibits the already crowded interlayer space. The simultaneous consideration of steric interactions and the hydrophobic nature of aliphatic organic moieties in organosilanes explain the drying shrinkage-free attributes of

In practice, incorporating shrinkage-reducing admixtures (SRA) to the mix can reduce cement-based materials' drying shrinkage. Shrinkage admixtures typically consist of glycol ethers and can reduce the magnitude of drying shrinkage up to 50% [314]. Early on, several proposed (for instance [315]) that shrinkage-reducing admixtures act by decreasing the liquid-air interface's surface tension; hence the capillary forces to which the solid skeleton is submitted also decrease. However, although shrinkage-reducing admixtures do indeed reduce this interface's surface tension, such a mechanism cannot be the only one at play because the reduction of drying shrinkage and the surface tension are not correlated [141]. A variety of other mechanisms have been

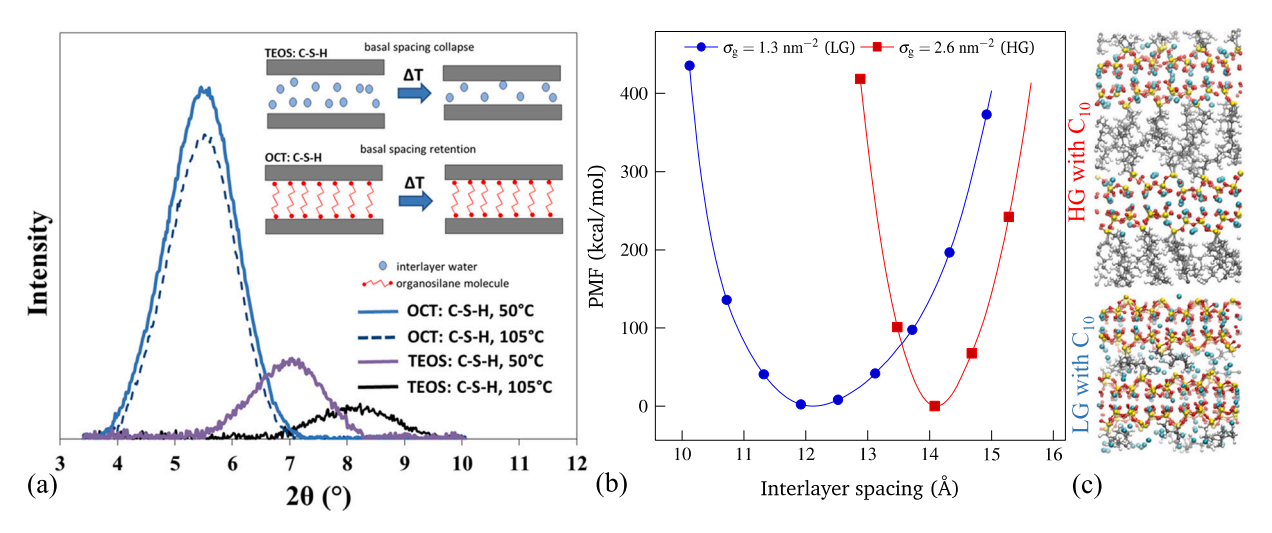


Fig. 16. Crosslinked C-S-H (XCSH) exhibits no drying shrinkage. (a) Moshiri et al.'s [312] high-resolution XRD scans to study the impact of drying on the basal spacing of tobermorite and C8 XCSH. (b) Morshedifard et al.'s [313] PMF calculation shows the impact of grafting density (LG: Low Grafting vs. HG: High Grafting) on adjusting the interlayer spacing of C4 XCSH. (C) The schematic representation of C10 XCSH with LG and HG densities. Silicon, oxygen, hydrogen, calcium, and carbon atoms are shown in yellow, red, white, cyan, and gray colors, respectively. (For interpretation of the references to colour in this figure legend, the reader is referred to the web version of this article.)

proposed to explain why shrinkage-reducing admixtures work, among which: modification of the microstructure of portlandite by the SRA [316], inhibition of microstructural collapse during drying by the SRA [37,141], impact on disjoining pressure [317], the effect of the SRA on the range of relative humidities over which capillary forces act [318,319]. Disentangling those various mechanisms is complex experimentally. Molecular simulations could prove a valuable tool to study them one by one and better understand why some SRAs are more efficient than others, paving the way to develop new and more efficient SRAs.

The first studies presented in this section demonstrate that, by coupling experimental synthesis/characterization efforts with molecular simulations, one can gain unprecedented insight into the molecular origins of drying shrinkage and design novel frameworks to inhibit shrinkage starting from the nanoscale. Perhaps, we could envision that we will design cement chemistries for specific shrinkage/swelling behavior in the future. An extreme case would be the design of concrete that does not swell or shrink, maybe due to a negligible variation of water content in specific ranges of relative humidity, with obvious applications of such durable concrete to civil and energy infrastructure. Another instance that atomistic simulations can perhaps create a quantum leap in concrete practice is designing new shrinkage reducing admixtures to minimize the shrinkage and admixture use while minimizing experimental research and development costs. Regarding the sorptive behavior, it might be possible to tailor cement-based composites bottom-up for optimal moisture buffer capacity or humidity regulation capacity in applications, for example, regarding indoor air quality (e.g., [320]). In a more ambitious perspective at the city scale, building facade design could use such technology to harvest water in arid climates efficiently. From a more general perspective extending beyond drying shrinkage and sorption, as molecular simulations advance in cement and concrete research, we believe such methods will play an indispensable role in designing new generations of eco-friendly, durable cementitious composites.

Declaration of competing interest

The authors Mohammad Javad Abdolhosseini Qomi, Laurent Brochard, Tulio Honorio, Ippei Maruyama, and Matthieu Vandamme of the manuscript "Advances in Atomistic Modeling and Understanding of Drying Shrinkage in Cementitious Materials" submitted to Cement and

Concrete Research declare no conflict of interest.

Acknowledgments

The contribution by M.J.A.Q. was supported by the United States's NSF CMMI Grant No. 1826122. I.M was supported by the JSPS Kakenhi Grant No. 18H03804. T.H. was supported by the French National Research Agency (ANR) through the project THEDESCO (ANR-19-CE22-0004-01). M.V. was supported by The French National Agency for Research (ANR - TWIST - 17-CE08-0003-01). L.B., T.H., and M.V. acknowledge the incentives for collaboration of the Ile-de-France Region in the framework of Respore, the Île-de-France network of Excellence in Porous Solids.

References

- G. Habert, S.A. Miller, V.M. John, J.L. Provis, A. Favier, A. Horvath, K. L. Scrivener, Environmental impacts and decarbonization strategies in the cement and concrete industries, Nat. Rev. Earth Environ. (2020) 1–15, https://doi.org/ 10.1038/s43017-020-0093-3.
- [2] M. Mastali, P. Kinnunen, A. Dalvand, R. Mohammadi Firouz, M. Illikainen, Drying shrinkage in alkali-activated binders – a critical review, Constr. Build. Mater. 190 (2018) 533–550, https://doi.org/10.1016/j. conbuildmat.2018.09.125.
- [3] A. Jain, S.P. Ong, G. Hautier, W. Chen, W.D. Richards, S. Dacek, S. Cholia, D. Gunter, D. Skinner, G. Ceder, K.A. Persson, Commentary: the materials project: a materials genome approach to accelerating materials innovation, APL Materials 1 (2013), 011002, https://doi.org/10.1063/1.4812323.
- [4] J.D. Durrant, J.A. McCammon, Molecular dynamics simulations and drug discovery, BMC Biol. 9 (2011) 71, https://doi.org/10.1186/1741-7007-9-71.
- [5] K. Kovler, S. Zhutovsky, Overview and future trends of shrinkage research, Mater. Struct. 39 (2006) 827.
- [6] T.C. Powers, A Hypothesis on Carbonation Shrinkage, Journal of the PCA Research and Development Laboratories, 1962.
- [7] B. Gérard, J. Marchand, Influence of cracking on the diffusion properties of cement-based materials: part I: influence of continuous cracks on the steady-state regime, Cem. Concr. Res. 30 (2000) 37–43, https://doi.org/10.1016/S0008-8846 (99)00201-X.
- [8] U. Greiner, W. Ramm, Air leakage characteristics in cracked concrete, Nucl. Eng. Des. 156 (1995) 167–172, https://doi.org/10.1016/0029-5493(94)00942-R.
- [9] H. Le Chatelier, Sur les changements de volume qui accompagnent le durcissement des ciments, Bulletin de La Société d'Encouragement Pour l'Industrie Nationale, 1900.
- [10] E. Freyssinet, Etudes sur les déformations lentes des ciments ou retraits 18, Liège, Belgium, 1930.
- [11] R.W. Carlson, Drying shrinkage of large concrete members, JP. 33 (1937) 327–336, https://doi.org/10.14359/8421.

- [12] I. Maruyama, Y. Nishioka, G. Igarashi, K. Matsui, Microstructural and bulk property changes in hardened cement paste during the first drying process, Cem. Concr. Res. 58 (2014) 20–34, https://doi.org/10.1016/j.cemconres.2014.01.007.
- [13] I. Maruyama, Origin of drying shrinkage of hardened cement paste: hydration pressure, J. Adv. Concr. Technol. 8 (2010) 187–200.
- [14] H.F.W. Taylor, Cement Chemistry, 2nd ed., Thomas Telford, London, 1997.
- [15] P.K. Mehta, P.J.M. Monteiro, Concrete: Microstructure, Properties and Materials, 3rd ed., McGraw-Hill, 2006.
- [16] J.J. Thomas, H.M. Jennings, A.J. Allen, The surface area of hardened cement paste as measured by various techniques, Concr. Sci. Eng. 1 (1999) 45–64.
- [17] A.J. Allen, C.G. Windsor, V. Rainey, D. Pearson, D.D. Double, N.M. Alford, A small-angle neutron scattering study of cement porosities, J. Phys. D. Appl. Phys. 15 (1982) 1817–1834, https://doi.org/10.1088/0022-3727/15/9/027.
- [18] H.M. Jennings, Refinements to colloid model of C-S-H in cement: CM-II, Cem. Concr. Res. 38 (2008) 275–289.
- [19] A. Muller, K. Scrivener, A.M. Gajewicz, P.J. McDonald, Densification of C-S-H measured by 1H NMR relaxometry, J. Phys. Chem. C. 117 (2013), https://doi. org/10.1021/JP3102964
- [20] T.C. Powers, T.L. Brownyard, Studies of the Physical Properties of Hardened Portland Cement Paste, Portland Cement Assoc R & D Lab Bulletin. https://trid. trb.org/view/101964, 1948. (Accessed 10 November 2020).
- [21] L.G. Baquerizo, T. Matschei, K.L. Scrivener, M. Saeidpour, A. Thorell, L. Wadsö, Methods to determine hydration states of minerals and cement hydrates, Cem. Concr. Res. 65 (2014) 85–95, https://doi.org/10.1016/j.cemconres.2014.07.009.
- [22] H.M. Jennings, A. Kumar, G. Sant, Quantitative discrimination of the nano-pore-structure of cement paste during drying: new insights from water sorption isotherms, Cem. Concr. Res. 76 (2015) 27–36, https://doi.org/10.1016/j.cemconres.2015.05.006.
- [23] E. Fratini, S.-H. Chen, P. Baglioni, M.-C. Bellissent-Funel, Age-dependent dynamics of water in hydrated cement paste, Phys. Rev. E 64 (2001), 020201, https://doi.org/10.1103/PhysRevE.64.020201.
- [24] E. Fratini, S.-H. Chen, P. Baglioni, M.-C. Bellissent-Funel, Quasi-elastic neutron scattering study of translational dynamics of hydration water in tricalcium silicate, J. Phys. Chem. B 106 (2002) 158–166, https://doi.org/10.1021/ ipol/p36m
- [25] S. Masoumi, H. Valipour, M.J. Abdolhosseini Qomi, Intermolecular forces between nanolayers of crystalline calcium-silicate-hydrates in aqueous medium, J. Phys. Chem. C 121 (2017) 5565–5572, https://doi.org/10.1021/acs. ipcc.6b10735.
- [26] M. Daimon, S. Ueda, R. Kondo, Morphological study on hydration of tricalcium silicate, Cem. Concr. Res. 1 (1971) 391–401, https://doi.org/10.1016/0008-8846 (71)90032-9.
- [27] I.G. Richardson, The nature of C-S-H in hardened cements, Cem. Concr. Res. 29 (1999) 1131–1147.
- [28] G. Constantinides, F.-J. Ulm, The effect of two types of C-S-H on the elasticity of cement-based materials: results from nanoindentation and micromechanical modeling, Cem. Concr. Res. 34 (2004) 67–80.
- [29] J. Thomas, The surface area of cement paste as measured by neutron scattering: evidence for two C-S-H morphologies, Cem. Concr. Res. 28 (1998) 897–905, https://doi.org/10.1016/S0008-8846(98)00049-0.
- [30] P.D. Tennis, H.M. Jennings, A model for two types of calcium silicate hydrate in the microstructure of Portland cement pastes, Cem. Concr. Res. 30 (2000) 855–863
- [31] G. Constantinides, F.-J. Ulm, The nanogranular nature of C-S-H, J. Mech. Phys. Solids 55 (2007) 64–90.
- [32] R.F. Feldman, P.J. Sereda, A model for hydrated Portland cement paste as deduced from sorption-length change and mechanical properties, Mater. Constr. 1 (1968) 509–520, https://doi.org/10.1007/BF02473639.
- [33] H.M. Jennings, A model for the microstructure of calcium silicate hydrate in cement paste, Cem. Concr. Res. 30 (2000) 101–116.
- [34] I.G. Richardson, Tobermorite/jennite- and tobermorite/calcium hydroxide-based models for the structure of C-S-H: applicability to hardened pastes of tricalcium silicate, beta-dicalcium silicate, Portland cement, and blends of Portland cement with blast-furnace slag, metakaolin, or silica fume, Cem. Concr. Res. 34 (2004) 1733–1777, https://doi.org/10.1016/j.cemconres.2004.05.034.
- [35] E.M. Gartner, A proposed mechanism for the growth of C-S-H during the hydration of tricalcium silicate, Cem. Concr. Res. 27 (1997) 665–672, https://doi. org/10.1016/S0008-8846(97)00049-5.
- [36] A.J. Allen, R.C. Oberthur, D. Pearson, P. Schofield, C.R. Wilding, Development of the fine porosity and gel structure of hydrating cement systems, Philos. Mag. B 56 (1987) 263–288.
- [37] E. Gartner, I. Maruyama, J. Chen, A new model for the C-S-H phase formed during the hydration of Portland cements, Cem. Concr. Res. 97 (2017) 95–106, https:// doi.org/10.1016/j.cemconres.2017.03.001.
- [38] S. Grangeon, F. Claret, C. Roosz, T. Sato, S. Gaboreau, Y. Linard, Structure of nanocrystalline calcium silicate hydrates: insights from X-ray diffraction, synchrotron X-ray absorption and nuclear magnetic resonance, J. Appl. Crystallogr. 49 (2016) 1–14, https://doi.org/10.1107/S1600576716003885.
- [39] K.J. Krakowiak, J.J. Thomas, S. James, M. Abuhaikal, F.-J. Ulm, Development of silica-enriched cement-based materials with improved aging resistance for application in high-temperature environments, Cem. Concr. Res. 105 (2018) 91–110.
- [40] P.A. Bonnaud, Q. Ji, B. Coasne, R.J.-M. Pellenq, K.J. Van Vliet, Thermodynamics of water confined in porous calcium-silicate-hydrates, Langmuir. 28 (2012) 11422–11432, https://doi.org/10.1021/la301738p.

- [41] J. Hagymassy, S. Brunauer, R.S. Mikhail, Pore structure analysis by water vapor adsorption: I. t-Curves for water vapor, J. Colloid Interface Sci. 29 (1969) 485–491, https://doi.org/10.1016/0021-9797(69)90132-5.
- [42] R. Badmann, N. Stockhausen, M.J. Setzer, The statistical thickness and the chemical potential of adsorbed water films, J. Colloid Interface Sci. 82 (1981) 534–542, https://doi.org/10.1016/0021-9797(81)90395-7.
- [43] J.J. Thomas, S.A. FitzGerald, D.A. Neumann, R.A. Livingston, State of water in hydrating tricalcium silicate and Portland cement pastes as measured by quasielastic neutron scattering, J. Am. Ceram. Soc. 84 (2001) 1811–1816, https://doi. org/10.1111/j.1151-2916.2001.tb00919.x.
- [44] E. Fratini, S.-H. Chen, P. Baglioni, J.C. Cook, J.R.D. Copley, Dynamic scaling of quasielastic neutron scattering spectra from interfacial water, Phys. Rev. E 65 (2001), 010201, https://doi.org/10.1103/PhysRevE.65.010201.
- [45] E. Fratini, F. Ridi, S.-H. Chen, P. Baglioni, Hydration water and microstructure in calcium silicate and aluminate hydrates, J. Phys. Condens. Matter 18 (2006) S2467, https://doi.org/10.1088/0953-8984/18/36/S18.
- [46] E. Fratini, A. Faraone, F. Ridi, S.-H. Chen, P. Baglioni, Hydration water dynamics in tricalcium silicate pastes by time-resolved incoherent elastic neutron scattering, J. Phys. Chem. C 117 (2013) 7358–7364, https://doi.org/10.1021/ ip312684b.
- [47] H. Li, E. Fratini, W.-S. Chiang, P. Baglioni, E. Mamontov, S.-H. Chen, Dynamic behavior of hydration water in calcium-silicate-hydrate gel: a quasielastic neutron scattering spectroscopy investigation, Phys. Rev. E 86 (2012), 061505, https://doi.org/10.1103/PhysRevE.86.061505.
- [48] F. Ridi, P. Luciani, E. Fratini, P. Baglioni, Water confined in cement pastes as a probe of cement microstructure evolution, J. Phys. Chem. B 113 (2009) 3080–3087, https://doi.org/10.1021/jp808754t.
- [49] F. Barberon, J.-P. Korb, D. Petit, V. Morin, E. Bermejo, What is the surface specific area of porous cement-based material? A nuclear magnetic relaxation dispersion approach, Magn. Reson. Imaging 21 (2003) 355–357, https://doi.org/10.1016/ S0730-725X(03)00137-1.
- [50] P.J. McDonald, J.-P. Korb, J. Mitchell, L. Monteilhet, Surface relaxation and chemical exchange in hydrating cement pastes: a two-dimensional NMR relaxation study, Phys. Rev. E 72 (2005), 011409, https://doi.org/10.1103/ PhysRevE.72.011409.
- [51] L. Monteilhet, J.-P. Korb, J. Mitchell, P.J. McDonald, Observation of exchange of micropore water in cement pastes by two-dimensional T-2-T-2 nuclear magnetic resonance relaxometry, Phys. Rev. E 74 (2006), 061404.
- [52] P.J. McDonald, J. Mitchell, M. Mulheron, P.S. Aptaker, J.-P. Korb, L. Monteilhet, Two-dimensional correlation relaxometry studies of cement pastes performed using a new one-sided NMR magnet, Cem. Concr. Res. 37 (2007) 303–309, https://doi.org/10.1016/j.cemconres.2006.01.013.
- [53] D.P. Bentz, K.K. Hansen, Preliminary observations of water movement in cement pastes during curing using X-ray absorption, Cem. Concr. Res. 30 (2000) 1157–1168, https://doi.org/10.1016/S0008-8846(00)00273-8.
- [54] P. Zhang, F.H. Wittmann, P. Lura, H.S. Müller, S. Han, T. Zhao, Application of neutron imaging to investigate fundamental aspects of durability of cement-based materials: a review, Cem. Concr. Res. 108 (2018) 152–166, https://doi.org/ 10.1016/j.cemconres.2018.03.003.
- [55] P.F. Faure, S. Rodts, Proton NMR relaxation as a probe for setting cement pastes, Magn. Reson. Imaging 26 (2008) 1183–1196, https://doi.org/10.1016/j. mri.2008.01.026.
- [56] R.A. Livingston, D.A. Neumann, A. Allen, J.J. Rush, Application of neutron scattering methods to cementitious materials, in: MRS Online Proceedings Library Archive 376, 1994, https://doi.org/10.1557/PROC-376-459.
- [57] J.J. Thomas, J.J. Chen, A.J. Allen, H.M. Jennings, Effects of decalcification on the microstructure and surface area of cement and tricalcium silicate pastes, Cem. Concr. Res. 34 (2004) 2297–2307, https://doi.org/10.1016/j. cemconres.2004.04.007.
- [58] S. Poyet, S. Charles, Temperature dependence of the sorption isotherms of cement-based materials: heat of sorption and Clausius-Clapeyron formula, Cem. Concr. Res. 39 (2009) 1060–1067, https://doi.org/10.1016/j. cemconres.2009.07.018.
- [59] S. Brunauer, I. Odler, M. Yudenfreund, The new model of hardened Portland cement paste, Highw. Res. Rec. 328 (1970) 89–107.
- [60] I. Langmuir, The adsorption of gases on plane surfaces of glass, mica and platinum, J. Am. Chem. Soc. 40 (1918) 1361–1403, https://doi.org/10.1021/ io02242a004
- [61] S. Brunauer, P.H. Emmett, E. Teller, Adsorption of gases in multimolecular layers, J. Am. Chem. Soc. 60 (1938) 309–319, https://doi.org/10.1021/ja01269a023.
- [62] E.P. Barrett, L.G. Joyner, P.P. Halenda, The determination of pore volume and area distributions in porous substances. I. Computations from nitrogen isotherms, J. Am. Chem. Soc. 73 (1951) 373–380, https://doi.org/10.1021/ja01145a126.
- [63] B.V. Derjaguin, N.V. Churaev, Polymolecular adsorption and capillary condensation in narrow slit pores, J. Colloid Interface Sci. 54 (1976) 157–175, https://doi.org/10.1016/0021-9797(76)90298-8.
- [64] A.V. Neimark, P.I. Ravikovitch, Capillary condensation in MMS and pore structure characterization, Microporous Mesoporous Mater. 44–45 (2001) 697–707, https://doi.org/10.1016/S1387-1811(01)00251-7.
- [65] N.V. Churaev, G. Starke, J. Adolphs, Isotherms of capillary condensation influenced by formation of adsorption films: 1. Calculation for model cylindrical and slit pores, J. Colloid Interface Sci. 221 (2000) 246–253, https://doi.org/ 10.1006/icis.1009.6502
- [66] L.D. Gelb, K.E. Gubbins, R. Radhakrishnan, M. Sliwinska-Bartkowiak, Phase separation in confined systems, Rep. Prog. Phys. 62 (1999) 1573–1659, https://doi.org/10.1088/0034-4885/62/12/201.

- [67] B. Coasne, A. Galarneau, R.J.M. Pellenq, F.D. Renzo, Adsorption, intrusion and freezing in porous silica: the view from the nanoscale, Chem. Soc. Rev. 42 (2013) 4141–4171, https://doi.org/10.1039/C2CS35384A.
- [68] Z. Zhang, M. Thiéry, V. Baroghel-Bouny, A review and statistical study of existing hysteresis models for cementitious materials, Cem. Concr. Res. 57 (2014) 44–60, https://doi.org/10.1016/j.cemconres.2013.12.008.
- [69] Z.P. Bažant, Thermodynamics of hindered adsorption and its implications for hardened cement paste and concrete, Cem. Concr. Res. 2 (1972) 1–16, https:// doi.org/10.1016/0008-8846(72)90019-1.
- [70] J.J. Beaudoin, L. Raki, R. Alizadeh, L. Mitchell, Dimensional change and elastic behavior of layered silicates and Portland cement paste, Cem. Concr. Compos. 32 (2010) 25–33, https://doi.org/10.1016/j.cemconcomp.2009.09.004.
- [71] F. Beltzung, F.H. Wittmann, Role of disjoining pressure in cement based materials, Cem. Concr. Res. 35 (2005) 2364–2370, https://doi.org/10.1016/j. cemconres.2005.04.004.
- [72] T.C. Powers, The thermodynamics of volume change and creep, Mater. Constr. 1 (1968) 487–507, https://doi.org/10.1007/BF02473638.
- [73] T.C. Powers, The Mechanics of Shrinkage and Reversible Creep of Hardened Cement Paste, London, 1965.
- [74] F. Wittmann, Surface tension skrinkage and strength of hardened cement paste, Mater. Constr. 1 (1968) 547–552, https://doi.org/10.1007/BF02473643.
- [75] F.H. Wittmann, Heresies on shrinkage and creep mechanisms, in: Proceedings of the 8th International Conference on Creep, Shrinkage and Durability Mechanics of Concrete and Concrete Structures (CONCREEP 8), Sept, 2008, pp. 3–9.
- [76] F.H. Wittmann, Creep and shrinkage mechanisms, in: Creep and Shrinkage in Concrete Structures, 1982, pp. 129–161.
- [77] G.Y. Gor, P. Huber, N. Bernstein, Adsorption-induced deformation of nanoporous materials—a review, Appl. Phys. Rev. 4 (2017), 011303, https://doi.org/ 10.1063/1.4975001.
- [78] I. Maruyama, J. Rymeš, M. Vandamme, B. Coasne, Cavitation of water in hardened cement paste under short-term desorption measurements, Mater. Struct. 51 (2018), https://doi.org/10.1617/s11527-018-1285-x.
- [79] J.W. Gibbs, The Collected Works of J. Willard Gibbs Volume I Thermodynamics, Longmans, Green and Co, New York, NY, 1928.
- [80] D.H. Bangham, R.I. Razouk, The swelling of charcoal. Part V. The saturation and immersion expansions and the heat of wetting, in: Proceedings of the Royal Society A: Mathematical, Physical and Engineering Sciences 166, 1938, pp. 572–586, https://doi.org/10.1098/rspa.1938.0112.
- [81] G. El Tabbal, P. Dangla, M. Vandamme, M. Bottoni, S. Granet, Modelling the drying shrinkage of porous materials by considering both capillary and adsorption effects, J. Mech. Phys. Solids 142 (2020) 104016, https://doi.org/ 10.1016/j.imps.2020.104016.
- [82] R. Shuttleworth, The surface tension of solids, in: Proceedings of the Physical Society, Section A 63, 1950, pp. 444–457.
- [83] G.Y. Gor, N. Bernstein, Revisiting Bangham's law of adsorption-induced deformation: changes of surface energy and surface stress, Phys. Chem. Chem. Phys. 18 (2016) 9788–9798, https://doi.org/10.1039/C6CP00051G.
- [84] O. Coussy, Mechanics and Physics of Porous Solids, Wiley, 2010.
- [85] R.A. Helmuth, D.M.H. Turk, The reversible and irreversible drying shrinkage of hardened Portland cement and tricalcium silicate paste, in: Portland Cement Association Journal Research and Development Laboratories 9, 1967, pp. 8–21.
- [86] C. Duckheim, M.J. Setzer, Hygric properties of hardened cement paste, in: M. J. Setzer (Ed.), Proceedings of 5th International Essen Workshop Transport in Concrete, Essen, 2007, pp. 217–226.
- [87] E.K. Attiogbe, D. Darwin, Submicrocracking in cement paste and mortar, Mater. J. 84 (1987) 491–500.
- [88] J. Bisschop, F.K. Wittel, Contraction gradient induced microcracking in hardened cement paste, Cem. Concr. Compos. 33 (2011) 466–473, https://doi.org/ 10.1016/j.cemconcomp.2011.02.004.
- [89] Z.P. Bažant, W.J. Raftshol, Effect of cracking in drying and shrinkage specimens, Cem. Concr. Res. 12 (1982) 209–226, https://doi.org/10.1016/0008-8846(82) 90008-4.
- [90] W. Hansen, Drying shrinkage mechanisms in Portland cement paste, J. Am. Ceram. Soc. 70 (1987) 323–328, https://doi.org/10.1111/j.1151-2916.1987 tb05002 v
- [91] I. Maruyama, G. Igarashi, Y. Nishioka, Bimodal behavior of C-S-H interpreted from short-term length change and water vapor sorption isotherms of hardened cement paste, Cem. Concr. Res. 73 (2015) 158–168, https://doi.org/10.1016/j. cemconres.2015.03.010.
- [92] N.N. Skoblinskaya, K.G. Krasilnikov, L.V. Nikitina, V.P. Varlamov, Changes in crystal structure of ettringite on dehydration. 2, in: Cement and Concrete Research 5, 1975, pp. 419–431, https://doi.org/10.1016/0008-8846(75)90017-4.
- [93] Y.F. Houst, Carbonation shrinkage of hydrated cement paste, in: Proc. 4th CANMET/ACI International Conference on Durability of Concrete, CANMET, Ottawa, Canada, 1997: pp. 481–491.
- [94] K. Kamimura, P.J. Sereda, E.G. Swenson, Changes in weight and dimensions in the drying and carbonation of Portland cement mortars, Mag. Concr. Res. 17 (1965) 5–14, https://doi.org/10.1680/macr.1965.17.50.5.
- [95] G. Verbeck, Carbonation of hydrated Portland cement, in: Cement and Concrete, ASTM International, 1958, pp. 17–36.
- [96] H. Ye, A. Radlińska, J. Neves, Drying and Carbonation Shrinkage of Cement Paste Containing Alkalis, 2017, https://doi.org/10.1617/s11527-017-1006-x.
- [97] K.L. Scrivener, H.F.W. Taylor, Delayed ettringite formation: a microstructural and microanalytical study, Adv. Cem. Res. 5 (1993) 139–146, https://doi.org/ 10.1680/adcr.1993.5.20.139.

- [98] H.F.W. Taylor, C. Famy, K.L. Scrivener, Delayed ettringite formation, Cem. Concr. Res. 31 (2001) 683–693. https://doi.org/10.1016/S0008-8846(01)00466-5.
- [99] M.A. Peter, A. Muntean, S.A. Meier, M. Böhm, Competition of several carbonation reactions in concrete: a parametric study, Cem. Concr. Res. 38 (2008) 1385–1393, https://doi.org/10.1016/j.cemconres.2008.09.003.
- [100] K. Kobayashi, K. Suzuki, Y. Uno, Carbonation of concrete structures and decomposition of CSH, Cem. Concr. Res. 24 (1994) 55–61, https://doi.org/ 10.1016/0008-8846(94)90082-5.
- [101] A. Morandeau, M. Thiéry, P. Dangla, Investigation of the carbonation mechanism of CH and C-S-H in terms of kinetics, microstructure changes and moisture properties, Cem. Concr. Res. 56 (2014) 153–170, https://doi.org/10.1016/j. cemconres.2013.11.015.
- [102] K. Suzuki, T. Nishikawa, S. Ito, Formation and carbonation of C-S-H in water, Cem. Concr. Res. 15 (1985) 213–224, https://doi.org/10.1016/0008-8846(85) 90032-8.
- [103] M.W. Grutzeck, A new model for the formation of calcium silicate hydrate (C-S-H), Mater. Res. Innov. 3 (1999) 160–170, https://doi.org/10.1007/
- [104] C.M. Hunt, L.A. Tomes, R.L. Blaine, Some effects of aging on the surface area of Portland cement paste, in: Journal of Research of the National Bureau of Standards Section A: Physics and Chemistry 64A, 1960, p. 163, https://doi.org/ 10.6028/jres.064a.016.
- [105] G.G. Litvan, R.E. Myers, Surface area of cement paste conditioned at various relative humidities, Cem. Concr. Res. 13 (1983) 49–60, https://doi.org/10.1016/ 0008-8846(83)90127-8
- [106] L.J. Parrott, W. Hansen, R.L. Berger, Effect of first drying upon the pore structure of hydrated alite paste, Cem. Concr. Res. 10 (1980) 647–655, https://doi.org/ 10.1016/0008-8846(80)90028-9.
- [107] L.A. Tomes, C.M. Hunt, R.L. Blaine, Some factors affecting the surface area of hydrated Portland cement as determined by water-vapor and nitrogen adsorption, J. Res. Natl. Bur. Stand. 59 (1957) 357, https://doi.org/10.6028/jres.059.039.
- [108] M. Wu, B. Johannesson, M. Geiker, A study of the water vapor sorption isotherms of hardened cement pastes: possible pore structure changes at low relative humidity and the impact of temperature on isotherms, Cem. Concr. Res. 56 (2014) 97–105, https://doi.org/10.1016/j.cemconres.2013.11.008.
- [109] R.E. Beddoe, K. Lang, Effect of moisture on fractal dimension and specific surface of hardened cement paste by small-angle X-ray scattering, Cem. Concr. Res. 24 (1994) 605–612, https://doi.org/10.1016/0008-8846(94)90184-8.
- [110] W.S. Chiang, E. Fratini, P. Baglioni, D. Liu, S.H. Chen, Microstructure determination of calcium-silicate-hydrate globules by small-angle neutron scattering, J. Phys. Chem. C 116 (2012) 5055–5061, https://doi.org/10.1021/ ip300745z.
- [111] J. Kropp, T. Gräfenecker, H.K. Hilsdorf, Characterization of the microstructure of hydrated cement paste by small angle X-ray scattering, in: J.W. Arrowsmith (Ed.), En Principles and Applications of Pore Structural Characterization, Bristol, 1985, pp. 83–96.
- [112] J.J. Thomas, A.J. Allen, H.M. Jennings, Structural changes to the calcium-silicate-hydrate gel phase of hydrated cement with age, drying, and resaturation, J. Am. Ceram. Soc. 91 (2008) 3362–3369, https://doi.org/10.1111/j.1551-2916.2008.02636.x.
- [113] J.J. Völkl, R.E. Beddoe, M.J. Setzer, The specific surface of hardened cement paste by small-angle X-ray scattering effect of moisture content and chlorides, Cem. Concr. Res. 17 (1987) 81–88, https://doi.org/10.1016/0008-8846(87)90062-7.
- [114] D.N. Winslow, S. Diamond, Specific surface of hardened Portland cement paste as determined by small-angle X-ray scattering, J. Am. Ceram. Soc. 57 (1974) 193–197, https://doi.org/10.1111/j.1151-2916.1974.tb10856.x.
- [115] D.H. Bager, E.J. Sellevold, Ice formation in hardened cement paste, part I room temperature cured pastes with variable moisture contents, Cem. Concr. Res. 16 (1986) 709–720, https://doi.org/10.1016/0008-8846(86)90045-1.
- [116] R.E. Beddoe, M.J. Setzer, Phase transformations of water in hardened cement paste a low-temperature DSC investigation, Cem. Concr. Res. 20 (1990) 236–242, https://doi.org/10.1016/0008-8846(90)90076-A.
- [117] P.C. Fonseca, H.M. Jennings, The effect of drying on early-age morphology of C-S-H as observed in environmental SEM, Cem. Concr. Res. 40 (2010) 1673–1680, https://doi.org/10.1016/j.cemconres.2010.08.007.
- [118] I. Maruyama, Multi-scale review for possible mechanisms of natural frequency change of reinforced concrete structures under an ordinary drying condition, J. Adv. Concr. Technol. 14 (2016) 691–705, https://doi.org/10.3151/ jact.14.691.
- [119] W. Soja, F. Georget, H. Maraghechi, K. Scrivener, Evolution of microstructural changes in cement paste during environmental drying, Cem. Concr. Res. 134 (2020) 106093, https://doi.org/10.1016/j.cemconres.2020.106093.
- [120] A. Gajewicz, Characterisation of Cement Microstructure and Pore Water Interaction by 1H Nuclear Magnetic Resonance Relaxometry, Department of Physical Science, 2014.
- [121] A.M. Gajewicz, E. Gartner, K. Kang, P.J. McDonald, V. Yermakou, A 1H NMR relaxometry investigation of gel-pore drying shrinkage in cement pastes, Cem. Concr. Res. 86 (2016) 12–19, https://doi.org/10.1016/j.cemconres.2016.04.013.
- [122] R. Kiran, H. Samouh, G. Igarashi, T. Haji, T. Ohkubo, S. Tomita, I. Maruyama, Temperature-dependent water redistribution from large pores to fine pores after water uptake in hardened cement paste, J. Adv. Concr. Technol. 18 (2020) 588–599, https://doi.org/10.3151/jact.18.588.
- [123] R. Schulte Holthausen, M. Raupach, Monitoring the internal swelling in cementitious mortars with single-sided 1H nuclear magnetic resonance, Cem. Concr. Res. 111 (2018) 138–146, https://doi.org/10.1016/j. cemconres.2018.05.021.

- [124] C. Zhou, F. Ren, Z. Wang, W. Chen, W. Wang, Why permeability to water is anomalously lower than that to many other fluids for cement-based material? Cem. Concr. Res. 100 (2017) 373–384, https://doi.org/10.1016/j. cemcoures.2017.08.002.
- [125] I. Maruyama, T. Ohkubo, T. Haji, R. Kurihara, Dynamic microstructural evolution of hardened cement paste during first drying monitored by 1H NMR relaxometry, Cem. Concr. Res. 122 (2019) 107–117, https://doi.org/10.1016/j. cemconres.2019.04.017.
- [126] A.C.A. Muller, K.L. Scrivener, A.M. Gajewicz, P.J. McDonald, Use of bench-top NMR to measure the density, composition and desorption isotherm of C-S-H in cement paste, Microporous Mesoporous Mater. 178 (2013) 99–103, https://doi. org/10.1016/j.micromeso.2013.01.032.
- [127] C. Zhou, F. Ren, Q. Zeng, L. Xiao, W. Wang, Pore-size resolved water vapor adsorption kinetics of white cement mortars as viewed from proton NMR relaxation, Cem. Concr. Res. 105 (2018) 31–43, https://doi.org/10.1016/j. cementers. 2017.12.002
- [128] S. Gaboreau, S. Grangeon, F. Claret, D. Ihiawakrim, O. Ersen, V. Montouillout, N. Maubec, C. Roosz, P. Henocq, C. Carteret, Hydration properties and interlayer organization in synthetic C-S-H, Langmuir. 36 (2020) 9449–9464, https://doi. org/10.1021/acs.langmuir.0c01335.
- [129] P. Bayliss, Further interlayer desorption studies of CSH(1), Cem. Concr. Res. 3 (1973) 185–188, https://doi.org/10.1016/0008-8846(73)90046-X.
- [130] W.A. Gutteridge, L.J. Parrott, A study of the changes in weight, length and interplanar spacing induced by drying and rewetting synthetic CSH (I), Cem. Concr. Res. 6 (1976) 357–366, https://doi.org/10.1016/0008-8846(76)90098-3.
- [131] R.H. Smith, Basal spacing hysteresis in CSH(1), Cem. Concr. Res. 3 (1973) 829–832, https://doi.org/10.1016/0008-8846(73)90015-X.
- [132] P.J. McDonald, O. Istok, M. Janota, A.M. Gajewicz-Jaromin, D.A. Faux, Sorption, anomalous water transport and dynamic porosity in cement paste: a spatially localised 1H NMR relaxation study and a proposed mechanism, Cem. Concr. Res. 133 (2020) 106045, https://doi.org/10.1016/j.cemconres.2020.106045.
- [133] A. Bentur, R.L. Berger, F.V. Lawrence, N.B. Milestone, S. Mindess, J.F. Young, Creep and drying shrinkage of calcium silicate pastes III. A hypothesis of irreversible strains, Cem. Concr. Res. 9 (1979) 83–95, https://doi.org/10.1016/ 0008-8846(79)90098-X.
- [134] L.J. Parrott, J.F. Young, Effect of prolonged drying upon the silicate structure of hydrated alite pastes, Cem. Concr. Res. 11 (1981) 11–17, https://doi.org/ 10.1016/0008-8846(81)90004-1.
- [135] X. Cong, R.J. Kirkpatrick, Effects of the temperature and relative humidity on the structure of C-S-H gel, Cem. Concr. Res. 25 (1995) 1237–1245, https://doi.org/ 10.1016/0008-8846(95)00116-T.
- [136] I. Maruyama, S. Ishikawa, J. Yasukouchi, S. Sawada, R. Kurihara, M. Takizawa, O. Kontani, Impact of gamma-ray irradiation on hardened white Portland cement pastes exposed to atmosphere, Cem. Concr. Res. 108 (2018) 59–71, https://doi. org/10.1016/j.cemconres.2018.03.005.
- [137] S. Thomas, K. Meise-Gresch, W. Muller-Warmuth, I. Odler, MAS NMR studies of partially carbonated Portland cement and tricalcium silicate pastes, J. Am. Ceram. Soc. 76 (1993) 1998–2004, https://doi.org/10.1111/j.1151-2916.1993. tb08323 x.
- [138] D. Snoeck, L.F. Velasco, A. Mignon, S. Van Vlierberghe, P. Dubruel, P. Lodewyckx, N. De Belie, The influence of different drying techniques on the water sorption properties of cement-based materials, Cem. Concr. Res. 64 (2014) 54–62, https://doi.org/10.1016/j.cemconres.2014.06.009.
- [139] A.C.A. Muller, Characterization of porosity & C-S-H in cement pastes by 1H NMR, in: PhD Thesis, École Polytechnique Fédérale de Lausanne, 2014.
- [140] J. Zhang, G.W. Scherer, Comparison of methods for arresting hydration of cement, Cem. Concr. Res. 41 (2011) 1024–1036, https://doi.org/10.1016/j. cemcoures 2011 06 003
- [141] I. Maruyama, E. Gartner, K. Beppu, R. Kurihara, Role of alcohol-ethylene oxide polymers on the reduction of shrinkage of cement paste, Cem. Concr. Res. 111 (2018) 157–168, https://doi.org/10.1016/j.cemconres.2018.05.017.
- [142] R.S. Mikhail, S.A. Selim, Adsorption of Organic Vapors in Relation to the Pore Structure of Hardened Portland Cement Pastes, Highway Research Board Special Report, 1966.
- [143] S.A. Hamid, The crystal structure of the 11 Ä natural tobermorite Ca2.25[Si307.5 (OH)1.5]·1H2O, in: Zeitschrift Für Kristallographie Crystalline Materials 154, 1981, pp. 189–198, https://doi.org/10.1524/zkri.1981.154.14.189.
- [144] A. Gmira, M. Zabat, R.J.-M. Pellenq, H. Van Damme, Microscopic physical basis of the poromechanical behavior of cement-based materials, Mater. Struct. 37 (2004) 3–14. https://doi.org/10.1007/BF02481622.
- [145] T. Honorio, Monte Carlo molecular modeling of temperature and pressure effects on the interactions between crystalline calcium silicate hydrate layers, Langmuir 35 (2019) 3907–3916, https://doi.org/10.1021/acs.langmuir.8b04156.
- [146] P.A. Bonnaud, C. Labbez, R. Miura, A. Suzuki, N. Miyamoto, N. Hatakeyama, A. Miyamoto, K.J.V. Vliet, Interaction grand potential between calcium-silicate-hydrate nanoparticles at the molecular level, Nanoscale 8 (2016) 4160-4172, https://doi.org/10.1039/C5NR08142D.
- [147] M.B. Pinson, E. Masoero, P.A. Bonnaud, H. Manzano, Q. Ji, S. Yip, J.J. Thomas, M. Z. Bazant, K.J. Van Vliet, H.M. Jennings, Hysteresis from multiscale porosity: modeling water sorption and shrinkage in cement paste, Phys. Rev. Appl. 3 (2015), 064009, https://doi.org/10.1103/PhysRevApplied.3.064009.
- [148] P.A. Bonnaud, Q. Ji, K.J. Van Vliet, Effects of elevated temperature on the structure and properties of calcium-silicate-hydrate gels: the role of confined water, Soft Matter 9 (2013) 6418-6429, https://doi.org/10.1039/c3sm50975c.

- [149] S. Masoumi, S. Zare, H. Valipour, M.J. Abdolhosseini Qomi, Effective interactions between calcium-silicate-hydrate nanolayers, J. Phys. Chem. C 123 (2019) 4755–4766, https://doi.org/10.1021/acs.jpcc.8b08146.
- [150] R.J.-M. Pellenq, A. Kushima, R. Shahsavari, K.J.V. Vliet, M.J. Buehler, S. Yip, F.-J. Ulm, A realistic molecular model of cement hydrates, Proc. Natl. Acad. Sci. 106 (2009) 16102–16107, https://doi.org/10.1073/pnas.0902180106.
- [151] M.J.A. Qomi, K.J. Krakowiak, M. Bauchy, K.L. Stewart, R. Shahsavari, D. Jagannathan, D.B. Brommer, A. Baronnet, M.J. Buehler, S. Yip, F.-J. Ulm, K.J. V. Vliet, R.J.-M. Pellenq, Combinatorial molecular optimization of cement hydrates, Nat. Commun. 5 (2014) 4960, https://doi.org/10.1038/ncomms5960.
- [152] A. Kunhi Mohamed, S.C. Parker, P. Bowen, S. Galmarini, An atomistic building block description of C-S-H - towards a realistic C-S-H model, Cem. Concr. Res. 107 (2018) 221–235, https://doi.org/10.1016/j.cemconres.2018.01.007.
- [153] S. Merlino, E. Bonaccorsi, T. Armbruster, Tobermorites; their real structure and order-disorder (OD) character, Am. Mineral. 84 (1999) 1613–1621, https://doi. org/10.2138/am-1999-1015.
- [154] S. Merlino, E. Bonaccorsi, T. Armbruster, The real structure of tobermorite 11Å: normal and anomalous forms, OD character and polytypic modifications, Eur. J. Mineral. 13 (2001) 577–590, https://doi.org/10.1127/0935-1221/2001/0013-0577.
- [155] M.J.A. Qomi, K.J. Krakowiak, M. Bauchy, K.L. Stewart, Pellenq Nichol Shahsavari, D. Jagannathan, D.B. Brommer, A. Baronnet, M.J. Buehler, S. Yip, F.-J. Ulm, K.J. Van Vliet, R.J.-M. Pellenq, Combinatorial molecular optimization of cement hydrates, Nat. Commun. 5 (2014) 4960, https://doi.org/ 10.1038/ncomms5960.
- [156] M.P. Allen, D.J. Tildesley, Computer Simulation of Liquids, Oxford University Press, New York, 1989.
- [157] I.-C. Yeh, G. Hummer, Diffusion and electrophoretic mobility of single-stranded RNA from molecular dynamics simulations, Biophys. J. 86 (2004) 681–689, https://doi.org/10.1016/S0006-3495(04)74147-8.
- [158] R.J.-M. Pelleng, D. Nicholson, Intermolecular potential function for the physical adsorption of rare gases in silicalite, J. Phys. Chem. 98 (1994) 13339–13349, https://doi.org/10.1021/j100101a039.
- [159] R. Shahsavari, R.J.-M. Pellenq, F.-J. Ulm, Empirical force fields for complex hydrated calcio-silicate layered materials, Phys. Chem. Chem. Phys. 13 (2010) 1002–1011, https://doi.org/10.1039/COCP00516A.
- [160] H. Manzano, R.J.M. Pellenq, F.-J. Ulm, M.J. Buehler, A.C.T. van Duin, Hydration of calcium oxide surface predicted by reactive force field molecular dynamics, Langmuir 28 (2012) 4187–4197, https://doi.org/10.1021/la204338m.
- [161] R. Mishra, A. Kunhi, D. Geissbühler, H. Manzano, T. Jamil, R. Shahsavari, A. G. Kalinichev, S. Galmarini, L. Tao, H. Heinz, R. Pellenq, A. van Duin, S.C. Parker, R. Flatt, P. Bowen, cemff: A force field database for cementitious materials including validations, applications and opportunities, Cem. Concr. Res. (2017), https://doi.org/10.1016/j.cemconres.2017.09.003.
- [162] Q. Ji, R.J.-M. Pellenq, K.J. Van Vliet, Comparison of computational water models for simulation of calcium-silicate-hydrate, Comput. Mater. Sci. 53 (2012) 234–240, https://doi.org/10.1016/j.commatsci.2011.08.024.
 [163] N. Metropolis, A.W. Rosenbluth, M.N. Rosenbluth, A.H. Teller, E. Teller, Equation
- [163] N. Metropolis, A.W. Rosenbluth, M.N. Rosenbluth, A.H. Teller, E. Teller, Equation of state calculations by fast computing machines, J. Chem. Phys. 21 (1953) 1087–1092, https://doi.org/10.1063/1.1699114.
- [164] D. Frenkel, B. Smit, Understanding Molecular Simulation, 2nd ed., Academic Press. San Diego, 2002.
- [165] S. Plimpton, Fast parallel algorithms for short-range molecular dynamics, J. Comput. Phys. 117 (1995) 1–19, https://doi.org/10.1006/jcph.1995.1039.
- [166] I.T. Todorov, W. Smith, K. Trachenko, M.T. Dove, DL POLY 3 new dimensions in molecular dynamics simulations via massive parallelism, J. Mater. Chem. 16 (2006) 1911–1918, https://doi.org/10.1039/B517931A.
- [167] J.D. Gale, GULP: a computer program for the symmetry-adapted simulation of solids, J. Chem. Soc. Faraday Trans. 93 (1997) 629–637, https://doi.org/ 10.1039/A606455H.
- [168] B. Hess, C. Kutzner, D. van der Spoel, E. Lindahl, GROMACS 4: algorithms for highly efficient, load-balanced, and scalable molecular simulation, J. Chem. Theory Comput. 4 (2008) 435–447, https://doi.org/10.1021/ct700301q.
- [169] M.G. Martin, MCCCS towhee: a tool for Monte Carlo molecular simulation, Mol. Simul. 39 (2013) 1212–1222, https://doi.org/10.1080/08927022.2013.828208.
- [170] D.C. Rapaport, The Art of Molecular Dynamics Simulation, Cambridge University Press, 2004.
- [171] C. Meral, C.J. Benmore, P.J.M. Monteiro, The study of disorder and nanocrystallinity in C–S–H, supplementary cementitious materials and geopolymers using pair distribution function analysis, Cem. Concr. Res. 41 (2011) 696–710, https://doi.org/10.1016/j.cemconres.2011.03.027.
- [172] M. Bauchy, M.J.A. Qomi, F.-J. Ulm, R.J.-M. Pellenq, Order and disorder in calcium-silicate-hydrate, J. Chem. Phys. 140 (2014) 214503, https://doi.org/ 10.1063/1.4879656
- [173] K. Yang, V.O. Özçelik, N. Garg, K. Gong, C.E. White, Drying-induced atomic structural rearrangements in sodium-based calcium-alumino-silicate-hydrate gel and the mitigating effects of ZrO ₂ nanoparticles, Phys. Chem. Chem. Phys. 20 (2018) 8593–8606, https://doi.org/10.1039/C7CP07876E.
- [174] M. Youssef, R.J.-M. Pellenq, B. Yildiz, Glassy nature of water in an ultraconfining disordered material: the case of calcium—silicate—hydrate, J. Am. Chem. Soc. 133 (2011) 2499–2510, https://doi.org/10.1021/ja107003a.
- [175] K.F. Rinne, S. Gekle, R.R. Netz, Ion-specific solvation water dynamics: single water versus collective water effects, J. Phys. Chem. A 118 (2014) 11667–11677, https://doi.org/10.1021/jp5066874.
- [176] D. Li, W. Zhao, D. Hou, T. Zhao, Molecular dynamics study on the chemical bound, physical adsorbed and ultra-confined water molecules in the nano-pore of

- calcium silicate hydrate, Constr. Build. Mater. 151 (2017) 563–574, https://doi.org/10.1016/j.conbuildmat.2017.06.053.
- [177] D.E. Smith, Molecular computer simulations of the swelling properties and interlayer structure of cesium montmorillonite, Langmuir 14 (1998) 5959–5967, https://doi.org/10.1021/la980015z.
- [178] S.V. Churakov, Structure of the interlayer in normal 11 a tobermorite from an ab initio study, Eur. J. Mineral. 21 (2009) 261–271, https://doi.org/10.1127/0935-1221/2009/0021-1865.
- [179] M. Zhou, A new look at the atomic level virial stress: on continuum-molecular system equivalence, in: Proceedings of the Royal Society of London. Series A: Mathematical, Physical and Engineering Sciences 459, 2003, pp. 2347–2392, https://doi.org/10.1098/rspa.2003.1127.
- [180] B. Jönsson, A. Nonat, C. Labbez, B. Cabane, H. Wennerström, Controlling the cohesion of cement paste, Langmuir 21 (2005) 9211–9221, https://doi.org/ 10.1021/ja051048z
- [181] B. Jönsson, H. Wennerström, A. Nonat, B. Cabane, Onset of cohesion in cement paste, Langmuir 20 (2004) 6702–6709, https://doi.org/10.1021/la0498760.
- [182] C. Plassard, E. Lesniewska, I. Pochard, A. Nonat, Nanoscale experimental investigation of particle interactions at the origin of the cohesion of cement, Langmuir 21 (2005) 7263–7270, https://doi.org/10.1021/la050440+.
- [183] T. Honorio, O.M. Chemgne Tamouya, Z. Shi, A. Bourdot, Intermolecular interactions of nanocrystalline alkali-silica reaction products under sorption, Cem. Concr. Res. 136 (2020) 106155, https://doi.org/10.1016/j. cemconres.2020.106155.
- [184] R.J. Kirkpatrick, A.G. Kalinichev, X. Hou, L. Struble, Experimental and molecular dynamics modeling studies of interlayer swelling: water incorporation in kanemite and ASR gel, Mater. Struct. 38 (2005) 449–458, https://doi.org/ 10.1617/14344
- [185] T.J. Tambach, P.G. Bolhuis, E.J.M. Hensen, B. Smit, Hysteresis in clay swelling induced by hydrogen bonding: accurate prediction of swelling states, Langmuir 22 (2006) 1223–1234, https://doi.org/10.1021/la051367q.
- [186] H.D. Whitley, D.E. Smith, Free energy, energy, and entropy of swelling in Cs-, Na-, and Sr-montmorillonite clays, J. Chem. Phys. 120 (2004) 5387–5395, https://doi. org/10.1063/1.1648013.
- [187] S. Masoumi, S. Zare, H. Valipour, M.J. Abdolhosseini Qomi, Effective interactions between calcium-silicate-hydrate nanolayers, J. Phys. Chem. C 123 (2019) 4755–4766, https://doi.org/10.1021/acs.jpcc.8b08146.
- [188] T. Honorio, L. Brochard, M. Vandamme, Hydration phase diagram of clay particles from molecular simulations, Langmuir 33 (2017) 12766–12776, https:// doi.org/10.1021/acs.langmuir.7b03198.
- [189] M.Z. Bazant, Z.P. Bažant, Theory of sorption hysteresis in nanoporous solids: part II molecular condensation, J. Mech. Phys. Solids 60 (2012) 1660–1675, https://doi.org/10.1016/j.imps.2012.04.015.
- [190] Z.P. Bazant, M.Z. Bazant, Theory of sorption hysteresis in nanoporous solids: part I. Snap-through instabilities. J. Mech. Phys. Solids 60 (2012) 1644–1659.
- [191] S.V. Churakov, C. Labbez, L. Pegado, M. Sulpizi, Intrinsic acidity of surface sites in calcium silicate hydrates and its implication to their electrokinetic properties, J. Phys. Chem. C 118 (2014) 11752–11762, https://doi.org/10.1021/jp502514a.
- [192] Y. Marcus, Effect of ions on the structure of water: structure making and breaking, Chem. Rev. 109 (2009) 1346–1370, https://doi.org/10.1021/cr8003828.
- [193] M. Chen, B. Coasne, R. Guyer, D. Derome, J. Carmeliet, Role of hydrogen bonding in hysteresis observed in sorption-induced swelling of soft nanoporous polymers, Nat. Commun. 9 (2018) 3507, https://doi.org/10.1038/s41467-018-05897-9.
- [194] D. Hou, H. Ma, Y. Zhu, Z. Li, Calcium silicate hydrate from dry to saturated state: structure, dynamics and mechanical properties, Acta Mater. 67 (2014) 81–94, https://doi.org/10.1016/j.actamat.2013.12.016.
- [195] S.V. Churakov, Structural position of H2O molecules and hydrogen bonding in anomalous 11 A tobermorite, Am. Mineral. 94 (2009) 156–165, https://doi.org/ 10.2138/am.2009.2907.
- [196] S.V. Churakov, Hydrogen bond connectivity in jennite from ab initio simulations, Cem. Concr. Res. 38 (2008) 1359–1364, https://doi.org/10.1016/j. cemconres.2008.08.004.
- [197] D.J. Earl, M.W. Deem, Parallel tempering: theory, applications, and new perspectives, Phys. Chem. Chem. Phys. 7 (2005) 3910–3916, https://doi.org/ 10.1039/B509983H.
- [198] D. Bousquet, F.-X. Coudert, A. Boutin, Free energy landscapes for the thermodynamic understanding of adsorption-induced deformations and structural transitions in porous materials, J. Chem. Phys. 137 (2012), 044118, https://doi. org/10.1063/1.4738776.
- [199] Y. Sugita, Y. Okamoto, Replica-exchange molecular dynamics method for protein folding, Chem. Phys. Lett. 314 (1999) 141–151, https://doi.org/10.1016/S0009-2614(99)01123-9
- [200] A. Laio, M. Parrinello, Escaping free-energy minima, PNAS 99 (2002) 12562–12566, https://doi.org/10.1073/pnas.202427399.
- [201] P.G. Bolhuis, D. Chandler, C. Dellago, P.L. Geissler, Transition path sampling: throwing ropes over rough mountain passes, in the dark, Annu. Rev. Phys. Chem. 53 (2002) 291–318, https://doi.org/10.1146/annurev. physchem.53.082301.113146.
- [202] S. Masoumi, H. Valipour, M.J. Abdolhosseini Qomi, Interparticle interactions in colloidal systems: toward a comprehensive mesoscale model, ACS Appl. Mater. Interfaces 9 (2017) 27338–27349, https://doi.org/10.1021/acsami.7b08465.
- [203] K. Ioannidou, K.J. Krakowiak, M. Bauchy, C.G. Hoover, E. Masoero, S. Yip, F.-J. Ulm, P. Levitz, R.J.-M. Pellenq, E. Del Gado, Mesoscale texture of cement hydrates, Proc. Natl. Acad. Sci. 113 (2016) 2029–2034, https://doi.org/10.1073/pnas.1520487113.

- [204] S. Masoumi, D. Ebrahimi, H. Valipour, M.J. Abdolhosseini Qomi, Nanolayered attributes of calcium-silicate-hydrate gels, J. Am. Ceram. Soc. 103 (2020) 541–557
- [205] H. Manzano, S. Moeini, F. Marinelli, A.C.T. van Duin, F.-J. Ulm, R.J.-M. Pellenq, Confined water dissociation in microporous defective silicates: mechanism, dipole distribution, and impact on substrate properties, J. Am. Chem. Soc. 134 (2012) 2208–2215, https://doi.org/10.1021/ja209152n.
- [206] P.A. Bonnaud, H. Manzano, R. Miura, A. Suzuki, N. Miyamoto, N. Hatakeyama, A. Miyamoto, Temperature dependence of nanoconfined water properties: Application to cementitious materials, J. Phys. Chem. C. (2016), https://doi.org/ 10.1021/acs.ipcc.6b00944.
- [207] A.G. Kalinichev, J. Wang, R.J. Kirkpatrick, Molecular dynamics modeling of the structure, dynamics and energetics of mineral–water interfaces: application to cement materials, Cem. Concr. Res. 37 (2007) 337–347, https://doi.org/ 10.1016/j.cemconres.2006.07.004.
- [208] J.-P. Korb, L. Monteilhet, P.J. McDonald, J. Mitchell, Microstructure and texture of hydrated cement-based materials: a proton field cycling relaxometry approach, Cem. Concr. Res. 37 (2007) 295–302, https://doi.org/10.1016/j. cemconres.2006.08.002.
- [209] J.S. Bhatt, P.J. McDonald, D.A. Faux, N.C. Howlett, S.V. Churakov, NMR relaxation parameters from molecular simulations of hydrated inorganic nanopores, Int. J. Quantum Chem. 114 (2014) 1220–1228, https://doi.org/ 10.1002/gua.24708.
- [210] M.J.A. Qomi, M. Bauchy, F.-J. Ulm, R.J.-M. Pellenq, Anomalous composition-dependent dynamics of nanoconfined water in the interlayer of disordered calcium-silicates, J. Chem. Phys. 140 (2014) 054515, https://doi.org/10.1063/1.4864118.
- [211] M.J.A. Qomi, F.-J. Ulm, R.J.-M. Pellenq, Physical origins of thermal properties of cement paste, Phys. Rev. Appl. 3 (2015), 064010, https://doi.org/10.1103/ PhysRevApplied.3.064010.
- [212] D.P. Bentz, Transient plane source measurements of the thermal properties of hydrating cement pastes, Mater. Struct. 40 (2007) 1073, https://doi.org/ 10.1617/s11527-006-9206-9.
- [213] D.J. Bonthuis, S. Gekle, R.R. Netz, Dielectric profile of interfacial water and its effect on double-layer capacitance, Phys. Rev. Lett. 107 (2011) 166102, https://doi.org/10.1103/PhysRevLett.107.166102.
- [214] A. Schlaich, E.W. Knapp, R.R. Netz, Water dielectric effects in planar confinement, Phys. Rev. Lett. 117 (2016), 048001, https://doi.org/10.1103/ PhysRevLett.117.048001.
- [215] A.C.A. Muller, K.L. Scrivener, J. Skibsted, A.M. Gajewicz, P.J. McDonald, Influence of silica fume on the microstructure of cement pastes: new insights from 1H NMR relaxometry, Cem. Concr. Res. 74 (2015) 116–125, https://doi.org/ 10.1016/j.cemconres.2015.04.005.
- [216] J.-P. Korb, P.J. McDonald, L. Monteilhet, A.G. Kalinichev, R.J. Kirkpatrick, Comparison of proton field-cycling relaxometry and molecular dynamics simulations for proton-water surface dynamics in cement-based materials, Cem. Concr. Res. 37 (2007) 348–350, https://doi.org/10.1016/j. cemcourses 2006.02.009
- [217] Y. Wu, H.L. Tepper, G.A. Voth, Flexible simple point-charge water model with improved liquid-state properties, J. Chem. Phys. 124 (2006), 024503, https://doi. org/10.1063/1.2136877
- [218] D.G. Archer, P. Wang, The dielectric constant of water and Debye-Hückel limiting law slopes, J. Phys. Chem. Ref. Data 19 (1990) 371–411, https://doi.org/ 10.1063/1.555853
- [219] K. Fujii, W. Kondo, Heterogeneous equilibrium of calcium silicate hydrate in water at 30 °C, J. Chem. Soc. Dalton Trans. (1981) 645–651, https://doi.org/ 10.1039/DT9810000645.
- [220] I.G. Richardson, Model structures for C-(A)-S-H(I), Acta Cryst. B. 70 (2014) 903–923, https://doi.org/10.1107/S2052520614021982.
- [221] J.J. Beaudoin, V.S. Ramachandran, R.F. Feldman, Interaction of chloride and C-S-H, Cem. Concr. Res. 20 (1990) 875–883, https://doi.org/10.1016/0008-8846(90) 90049-4.
- [222] X. Cong, R.J. Kirkpatrick, 29Si MAS NMR study of the structure of calcium silicate hydrate, Adv. Cem. Based Mater. 3 (1996) 144–156, https://doi.org/10.1016/ \$1065-7355(96)90046-2
- [223] E. L'Hôpital, B. Lothenbach, D.A. Kulik, K. Scrivener, Influence of calcium to silica ratio on aluminium uptake in calcium silicate hydrate, Cem. Concr. Res. 85 (2016) 111–121, https://doi.org/10.1016/j.cemconres.2016.01.014.
- [224] A.J. Allen, J.J. Thomas, H.M. Jennings, Composition and density of nanoscale calcium-silicate-hydrate in cement, Nat. Mater. 6 (2007) 311–316, https://doi. org/10.1038/nmat1871.
- [225] J.J. Thomas, J.J. Chen, H.M. Jennings, D.A. Neumann, Ca-OH bonding in the C-S-H gel phase of tricalcium silicate and white Portland cement pastes measured by inelastic neutron scattering, Chem. Mater. 15 (2003) 3813–3817.
- [226] K. Garbev, G. Beuchle, M. Bornefeld, L. Black, P. Stemmermann, Cell dimensions and composition of nanocrystalline calcium silicate hydrate solid solutions. Part 1: synchrotron-based X-ray diffraction, J. Am. Ceram. Soc. 91 (2008) 3005–3014, https://doi.org/10.1111/j.1551-2916.2008.02484.x.
- [227] G.L. Kalousek, A.F. Prebus, Crystal chemistry of hydrous calcium silicates: III, morphology and other properties of tobermorite and related phases, J. Am. Ceram. Soc. 41 (1958) 124–132, https://doi.org/10.1111/j.1151-2916.1958. tb13525.x.
- [228] H. Matsuyama, J.F. Young, Effects of pH on precipitation of quasi-crystalline calcium silicate hydrate in aqueous solution, Adv. Cem. Res. 12 (2000) 29–33, https://doi.org/10.1680/adcr.2000.12.1.29.

- [229] G. Renaudin, J. Russias, F. Leroux, F. Frizon, C. Cau-dit-Coumes, Structural characterization of C–S–H and C–A–S–H samples—part I: long-range order investigated by Rietveld analyses, J. Solid State Chem. 182 (2009) 3312–3319, https://doi.org/10.1016/j.jssc.2009.09.026.
- [230] D. Sugiyama, Chemical alteration of calcium silicate hydrate (C-S-H) in sodium chloride solution, Cem. Concr. Res. 38 (2008) 1270–1275, https://doi.org/ 10.1016/j.cemconres.2008.06.002.
- [231] H.F.W. Taylor, J.W. Howison, Relationships between calcium silicates and clay minerals, in: Clay Minerals Bulletin 3, 1956, pp. 98–111, https://doi.org/ 10.1180/claymin.1956.003.16.06.
- [232] G. Geng, R.J. Myers, M.J.A. Qomi, P.J.M. Monteiro, Densification of the interlayer spacing governs the nanomechanical properties of calcium-silicate-hydrate, Sci. Rep. 7 (2017) 10986, https://doi.org/10.1038/s41598-017-11146-8.
- [233] A. Morshedifard, S. Masoumi, M.J.A. Qomi, Nanoscale origins of creep in calcium silicate hydrates, Nat. Commun. 9 (2018) 1785, https://doi.org/10.1038/s41467-018-04174-7
- [234] T. Zhou, K. Ioannidou, F.-J. Ulm, M.Z. Bazant, R.J.-M. Pellenq, Multiscale poromechanics of wet cement paste, Proc. Natl. Acad. Sci. 116 (2019) 10652–10657, https://doi.org/10.1073/pnas.1901160116.
- [235] G. Geng, R.N. Vasin, J. Li, M.J.A. Qomi, J. Yan, H.-R. Wenk, P.J.M. Monteiro, Preferred orientation of calcium aluminosilicate hydrate induced by confined compression, Cem. Concr. Res. 113 (2018) 186–196, https://doi.org/10.1016/j. cemconres.2018.09.002.
- [236] I. Maruyama, N. Sakamoto, K. Matsui, G. Igarashi, Microstructural changes in white Portland cement paste under the first drying process evaluated by WAXS, SAXS, and USAXS, Cem. Concr. Res. 91 (2017) 24–32, https://doi.org/10.1016/j. cemconres.2016.10.002.
- [237] H. Rahoui, Contribution to Understanding the Action of Shrinkage Reducing Admixtures in Cementitious Materials: Experiments and Modeling (Ph.D thesis), Université Paris-Est, 2018.
- [238] C. Biagioni, E. Bonaccorsi, S. Merlino, D. Bersani, New data on the thermal behavior of 14Å tobermorite, Cem. Concr. Res. 49 (2013) 48–54, https://doi.org/ 10.1016/j.cemconres.2013.03.007.
- [239] P. Pourbeik, J.J. Beaudoin, R. Alizadeh, L. Raki, Dimensional stability of 1-4 nm tobermorite, jennite and other layered calcium silicate hydrates, Adv. Cem. Res. 27 (2015) 2–10. https://doi.org/10.1680/adcr.13.00054.
- [240] H.F.W. Taylor, The dehydration of tobermorite, Clay Clay Miner. 6 (1957) 101–109.
- [241] N.M.A. Krishnan, B. Wang, G. Falzone, Y. Le Pape, N. Neithalath, L. Pilon, M. Bauchy, G. Sant, Confined water in layered silicates: the origin of anomalous thermal expansion behavior in calcium-silicate-hydrates, ACS Appl. Mater. Interfaces (2016). https://doi.org/10.1021/acsami.6b11587.
- [242] J.P. Ciardullo, D.J. Sweeney, G.W. Scherer, Thermal expansion kinetics: Method to measure permeability of cementitious materials, IV. Effect of thermal gradients and viscoelasticity, J. Am. Ceram. Soc. 88 (2005) 1213–1221, https://doi.org/ 10.1111/j.1551-2916.2005.00214.x.
- [243] S.L. Meyers, Thermal coefficient of expansion of Portland cement long-time tests, Ind. Eng. Chem. 32 (1940) 1107–1112, https://doi.org/10.1021/ ie50368a018
- [244] J.J. Valenza, G.W. Scherer, Evidence of anomalous thermal expansion of water in cement paste, Cem. Concr. Res. 35 (2005) 57–66, https://doi.org/10.1016/j. cemconres.2004.08.022.
- [245] C.R. Cruz, M. Gillen, Thermal expansion of Portland cement paste, mortar and concrete at high temperatures, Fire Mater. 4 (1980) 66–70, https://doi.org/
- [246] D. Hou, Y. Zhu, Y. Lu, Z. Li, Mechanical properties of calcium silicate hydrate (C-S-H) at nano-scale: a molecular dynamics study, Mater. Chem. Phys. 146 (2014) 503–511, https://doi.org/10.1016/j.matchemphys.2014.04.001.
- [247] T. Honorio, L. Brochard, M. Vandamme, Effective stresses and estimations of the apparent biot coefficient in stacked clay layers, Géotechnique Lett. 8 (2018) 97–101, https://doi.org/10.1680/jgele.17.00170.
- [248] P. Simonnin, B. Noetinger, C. Nieto-Draghi, V. Marry, B. Rotenberg, Diffusion under confinement: hydrodynamic finite-size effects in simulation, J. Chem. Theory Comput. 13 (2017) 2881–2889, https://doi.org/10.1021/acs. ictc.7b00342.
- [249] P. Liu, E. Harder, B.J. Berne, On the calculation of diffusion coefficients in confined fluids and interfaces with an application to the liquid—vapor interface of water, J. Phys. Chem. B 108 (2004) 6595–6602, https://doi.org/10.1021/ in0375057
- [250] R. Metzler, J.-H. Jeon, A.G. Cherstvy, E. Barkai, Anomalous diffusion models and their properties: non-stationarity, non-ergodicity, and ageing at the centenary of single particle tracking, Phys. Chem. Chem. Phys. 16 (2014) 24128–24164, https://doi.org/10.1039/C4CP03465A.
- [251] R. Bergman, J. Swenson, Dynamics of supercooled water in confined geometry, Nature 403 (2000) 283–286, https://doi.org/10.1038/35002027.
- [252] S. Hong, S. Qin, W. Yao, B. Guo, D. Hou, Y. Zhang, W. Liu, W. Li, B. Dong, Visualized tracing of capillary absorption process in cementitious material based on X ray computed tomography, Cem. Concr. Compos. 107 (2020) 103487, https://doi.org/10.1016/j.cemconcomp.2019.103487.
- [253] A. Botan, B. Rotenberg, V. Marry, P. Turq, B. Noetinger, Hydrodynamics in clay nanopores, J. Phys. Chem. C 115 (2011) 16109–16115, https://doi.org/10.1021/ ip204772c.
- [254] T. Honorio, K. Abahri, Non equilibrium molecular dynamics simulation of the hydrodynamics in crystalline calcium silicate hydrates nanopores, in: RILEM Spring Convention and Sustainable Materials, Systems and Structures Conference,

- Rovinj, Croatia, 2019. https://hal.archives-ouvertes.fr/hal-02074624. (Accessed 30 June 2020).
- [255] V. Ballenegger, J.-P. Hansen, Dielectric permittivity profiles of confined polar fluids, J. Chem. Phys. 122 (2005) 114711, https://doi.org/10.1063/1.1845431.
- [256] P. Suwanmaneechot, A. Aili, I. Maruyama, Creep behavior of C-S-H under different drying relative humidities: interpretation of microindentation tests and sorption measurements by multi-scale analysis, Cem. Concr. Res. 132 (2020) 106036, https://doi.org/10.1016/j.cemconres.2020.106036.
- [257] Z. Chen, L. Sorelli, Effect of relative humidity and porosity on the logarithmic creep of the layered C–S–H minerals tobermorite and jennite, Cem. Concr. Compos. 103872 (2020), https://doi.org/10.1016/j.cemconcomp.2020.103872.
- [258] T. Honorio, O.M.C. Tamouya, Z. Shi, Specific ion effects control the thermoelastic behavior of nanolayered materials: the case of crystalline alkali-silica reaction products, Phys. Chem. Chem. Phys. (2020), https://doi.org/10.1039/ D0CP04955G.
- [259] Z. Shi, A. Leemann, D. Rentsch, B. Lothenbach, Synthesis of alkali-silica reaction product structurally identical to that formed in field concrete, in: Materials & Design, 2020, p. 108562, https://doi.org/10.1016/j.matdes.2020.108562.
- [260] Z. Shi, G. Geng, A. Leemann, B. Lothenbach, Synthesis, characterization, and water uptake property of alkali-silica reaction products, Cem. Concr. Res. 121 (2019) 58–71, https://doi.org/10.1016/j.cemconres.2019.04.009.
- [261] L.G. Baquerizo, T. Matschei, K.L. Scrivener, M. Saeidpour, L. Wadsö, Hydration states of AFm cement phases, Cem. Concr. Res. 73 (2015) 143–157, https://doi. org/10.1016/j.cemconres.2015.02.011.
- [262] T. Honorio, P. Guerra, A. Bourdot, Molecular simulation of the structure and elastic properties of ettringite and monosulfoaluminate, Cem. Concr. Res. 135 (2020) 106126, https://doi.org/10.1016/j.cemconres.2020.106126.
- [263] A.G. Kalinichev, R.J. Kirkpatrick, R.T. Cygan, Molecular modeling of the structure and dynamics of the interlayer and surface species of mixed-metal layered hydroxides: chloride and water in hydrocalumite (Friedel's salt), Am. Mineral. 85 (2000) 1046–1052, https://doi.org/10.2138/am-2000-0720.
- [264] A.G. Kalinichev, R.J. Kirkpatrick, Molecular dynamics modeling of chloride binding to the surfaces of calcium hydroxide, hydrated calcium aluminate, and calcium silicate phases, Chem. Mater. 14 (2002) 3539–3549, https://doi.org/ 10.1021/cm0107070.
- [265] R.J. Kirkpatrick, A.G. Kalinichev, J. Wang, X. Hou, J.E. Amonette, Molecular modeling of the vibrational spectra of interlayer and surface species of layered double hydroxides, in: The Application of Vibrational Spectroscopy to Clay Minerals and Layered Double Hydroxides, Clay Minerals Society, 2005, https:// doi.org/10.1346/CMS-WLS-13.9.
- [266] R.J. Kirkpatrick, P. Yu, X. Hou, Y. Kim, Interlayer structure, anion dynamics, and phase transitions in mixed-metal layered hydroxides; variable temperature ³⁵ Cl NMR spectroscopy of hydrotalcite and Ca-aluminate hydrate (hydrocalumite), Am. Mineral. 84 (1999) 1186–1190, https://doi.org/10.2138/am-1999-7-823.
- [267] D. Nied, K. Enemark-Rasmussen, E. L'Hopital, J. Skibsted, B. Lothenbach, Properties of magnesium silicate hydrates (M-S-H), Cem. Concr. Res. 79 (2016) 323–332, https://doi.org/10.1016/j.cemconres.2015.10.003.
- [268] T. Mitsuda, H. Taguchi, Formation of magnesium silicate hydrate and its crystallization to talc, Cem. Concr. Res. 7 (1977) 223–230, https://doi.org/ 10.1016/0008-8846(77)90083-7.
- [269] E. Bernard, B. Lothenbach, C. Chlique, M. Wyrzykowski, A. Dauzères, I. Pochard, C. Cau-Dit-Coumes, Characterization of magnesium silicate hydrate (M-S-H), Cem. Concr. Res. 116 (2019) 309–330, https://doi.org/10.1016/j. cemconres.2018.09.007.
- [270] L.G. Baquerizo, T. Matschei, K.L. Scrivener, Impact of water activity on the stability of ettringite, Cem. Concr. Res. 79 (2016) 31–44, https://doi.org/ 10.1016/j.cemconres.2015.07.008.
- [271] B. Chen, F. Kuznik, M. Horgnies, K. Johannes, V. Morin, E. Gengembre, Physicochemical properties of ettringite/meta-ettringite for thermal energy storage: review, Sol. Energy Mater. Sol. Cells 193 (2019) 320–334, https://doi. org/10.1016/j.solmat.2018.12.013.
- [272] L.J. Struble, P.W. Brown, An Evaluation of Ettringite and Related Compounds for Use in Solar Energy Storage, National Bureau of Standards, Gaithersburg, MD, 1984, https://doi.org/10.6028/NBS.IR.84-2942.
- [273] H. Manzano, A. Ayuela, A. Telesca, P.J.M. Monteiro, J.S. Dolado, Ettringite strengthening at high pressures induced by the densification of the hydrogen bond network, J. Phys. Chem. C 116 (2012) 16138–16143, https://doi.org/ 10.1021/jp301822e.
- [274] Q. Zhou, E.E. Lachowski, F.P. Glasser, Metaettringite, a decomposition product of ettringite, Cem. Concr. Res. 34 (2004) 703–710, https://doi.org/10.1016/j. cemconres.2003.10.027.
- [275] R.T. Cygan, J.-J. Liang, A.G. Kalinichev, Molecular models of hydroxide, oxyhydroxide, and clay phases and the development of a general force field, J. Phys. Chem. B 108 (2004) 1255–1266, https://doi.org/10.1021/jp0363287.
- [276] R.J.-M. Pellenq, H. Van Damme, Why does concrete set?: the nature of cohesion forces in hardened cement-based materials, MRS Bull. 29 (2004) 319–323, https://doi.org/10.1557/mrs2004.97.
- [277] E. Ferrage, B. Lanson, B.A. Sakharov, V.A. Drits, Investigation of smectite hydration properties by modeling experimental X-ray diffraction patterns: Part I. Montmorillonite hydration properties, in: American Mineralogist 90, 2005, pp. 1358–1374, https://doi.org/10.2138/am.2005.1776.
- [278] T.J. Tambach, E.J.M. Hensen, B. Smit, Molecular simulations of swelling clay minerals, J. Phys. Chem. B 108 (2004) 7586–7596, https://doi.org/10.1021/ in040790b
- [279] E.J.W. Verwey, Theory of the stability of lyophobic colloids, J. Phys. Chem. 51 (1947) 631–636, https://doi.org/10.1021/j150453a001.

- [280] B.V. Derjaguin, N.V. Churaev, V.M. Muller, The Derjaguin-Landau-Verwey-Overbeek (DLVO) theory of stability of lyophobic colloids, in: B.V. Derjaguin, N. V. Churaev, V.M. Muller (Eds.), Surface Forces, Springer US, Boston, MA, 1987, pp. 293–310, https://doi.org/10.1007/978-1-4757-6639-4-8.
- [281] B.E. Viani, P.F. Low, C.B. Roth, Direct measurement of the relation between interlayer force and interlayer distance in the swelling of montmorillonite, J. Colloid Interface Sci. 96 (1983) 229–244, https://doi.org/10.1016/0021-9797 (83)90025-5.
- [282] S. Karaborni, B. Smit, W. Heidug, J. Urai, E. van Oort, The swelling of clays: molecular simulations of the hydration of montmorillonite, Science. 271 (1996) 1102–1104, https://doi.org/10.1126/science.271.5252.1102.
- [283] T. Honorio, L. Brochard, M. Vandamme, A. Lebée, Flexibility of nanolayers and stacks: implications in the nanostructuration of clays, Soft Matter 14 (2018) 7354–7367, https://doi.org/10.1039/C8SM01359D.
- [284] R.T. Cygan, J.A. Greathouse, H. Heinz, A.G. Kalinichev, Molecular models and simulations of layered materials, J. Mater. Chem. 19 (2009) 2470–2481, https:// doi.org/10.1039/B819076C.
- [285] X.-D. Liu, X.-C. Lu, A thermodynamic understanding of clay-swelling inhibition by potassium ions, Angew. Chem. Int. Ed. 45 (2006) 6300–6303, https://doi.org/ 10.1002/anie.200601740.
- [286] C. Labbez, B. Jönsson, I. Pochard, A. Nonat, B. Cabane, Surface charge density and electrokinetic potential of highly charged minerals: experiments and Monte Carlo simulations on calcium silicate hydrate, J. Phys. Chem. B 110 (2006) 9219–9230, https://doi.org/10.1021/jp057096+.
- [287] S. Brunauer, D.L. Kantro, C.H. Weise, The surface energy of tobermorite, Can. J. Chem. 37 (1959) 714–724, https://doi.org/10.1139/v59-097.
- [288] S. Brunauer, Surfaces of solids, Pure Appl. Chem. 10 (1965) 293–308, https://doi. org/10.1351/pac196510040293.
- [289] R.J.-M. Pellenq, N. Lequeux, H. van Damme, Engineering the bonding scheme in C-S-H: the iono-covalent framework, Cem. Concr. Res. 38 (2008) 159–174, https://doi.org/10.1016/j.cemconres.2007.09.026.
- [290] R. Shahsavari, M.J. Buehler, R.J.-M. Pellenq, F.-J. Ulm, First-principles study of elastic constants and interlayer interactions of complex hydrated oxides: case study of tobermorite and jennite, J. Am. Ceram. Soc. 92 (2009) 2323–2330, https://doi.org/10.1111/j.1551-2916.2009.03199.x.
- [291] J.E. Oh, S.M. Clark, P.J.M. Monteiro, Does the Al substitution in C-S-H(I) change its mechanical property? Cem. Concr. Res. 41 (2011) 102–106, https://doi.org/ 10.1016/j.cemconres.2010.09.010.
- [292] J.E. Oh, S.M. Clark, H.-R. Wenk, P.J.M. Monteiro, Experimental determination of bulk modulus of 14 Å tobermorite using high pressure synchrotron X-ray diffraction, Cem. Concr. Res. 42 (2012) 397–403, https://doi.org/10.1016/j. cemconres.2011.11.004.
- [293] M. Bauchy, H. Laubie, M.J. Abdolhosseini Qomi, C.G. Hoover, F.-J. Ulm, R.J.-M. Pelleng, Fracture toughness of calcium–silicate–hydrate from molecular dynamics simulations, J. Non-Cryst. Solids 419 (2015) 58–64, https://doi.org/10.1016/j.inoncrysol.2015.03.031.
- [294] C.T. Kresge, M.E. Leonowicz, W.J. Roth, J.C. Vartuli, J.S. Beck, Ordered mesoporous molecular sieves synthesized by a liquid-crystal template mechanism, Nature 359 (1992) 710–712, https://doi.org/10.1038/359710a0.
- [295] L. Brochard, M. Vandamme, R.J.-M. Pellenq, Poromechanics of microporous media, J. Mech. Phys. Solids 60 (2012) 606–622, https://doi.org/10.1016/j. imps.2012.01.001.
- [296] P.I. Ravikovitch, A.V. Neimark, Density functional theory model of adsorption deformation, Langmuir 22 (2006) 10864–10868, https://doi.org/10.1021/ https://doi.org/10.1021/
- [297] F.-X. Coudert, M. Jeffroy, A.H. Fuchs, A. Boutin, C. Mellot-Draznieks, Thermodynamics of guest-induced structural transitions in hybrid organic—inorganic frameworks, J. Am. Chem. Soc. 130 (2008) 14294–14302, https://doi.org/10.1021/ja805129c.
- [298] M. Chen, B. Coasne, D. Derome, J. Carmeliet, Coupling of sorption and deformation in soft nanoporous polymers: molecular simulation and poromechanics, J. Mech. Phys. Solids 137 (2020) 103830, https://doi.org/ 10.1016/j.jmps.2019.103830.

- [299] L. Brochard, M. Vandamme, R.J.-M. Pellenq, T. Fen-Chong, Adsorption-induced deformation of microporous materials: coal swelling induced by CO2–CH4 competitive adsorption, Langmuir 28 (2012) 2659–2670, https://doi.org/ 10.1021/la204072d.
- [300] A. Rahaman, V.H. Grassian, C.J. Margulis, Dynamics of water adsorption onto a calcite surface as a function of relative humidity, J. Phys. Chem. C 112 (2008) 2109–2115, https://doi.org/10.1021/jp077594d.
- [301] A. Malani, K.G. Ayappa, Adsorption isotherms of water on mica: redistribution and film growth, J. Phys. Chem. B 113 (2009) 1058–1067.
- [302] T. Cheng, H. Sun, Adsorption of ethanol vapor on mica surface under different relative humidities: a molecular simulation study, J. Phys. Chem. C 116 (2012) 16436–16446, https://doi.org/10.1021/jp3020595.
- [304] J.S. Loring, C.J. Thompson, Z. Wang, A.G. Joly, D.S. Sklarew, H.T. Schaef, E. S. Ilton, K.M. Rosso, A.R. Felmy, In situ infrared spectroscopic study of forsterite carbonation in wet supercritical CO2, Environ. Sci. Technol. 45 (2011) 6204–6210, https://doi.org/10.1021/es201284e.
- [305] M. Vandamme, L. Brochard, B. Lecampion, O. Coussy, Adsorption and strain: the CO2-induced swelling of coal, J. Mech. Phys. Solids 58 (2010) 1489–1505, https://doi.org/10.1016/j.jmps.2010.07.014.
- [306] E. Masoero, E. Del Gado, R.J.-M. Pellenq, F.-J. Ulm, S. Yip, Nanostructure and nanomechanics of cement: polydisperse colloidal packing, Phys. Rev. Lett. 109 (2012) 155503, https://doi.org/10.1103/PhysRevLett.109.155503.
- [307] K. Ioannidou, R.J.-M. Pelleng, E. Del Gado, Controlling local packing and growth in calcium-silicate-hydrate gels, Soft Matter 10 (2014) 1121–1133.
- [308] T. Zhou, K. Ioannidou, E. Masoero, M. Mirzadeh, R.J.-M. Pellenq, M.Z. Bazant, Capillary stress and structural relaxation in moist granular materials, Langmuir 35 (2019) 4397–4402, https://doi.org/10.1021/acs.langmuir.8b03400.
- [309] R.F. Feldman, Sorption and length-change scanning isotherms of methanol and water on hydrated portland cement, in: Fifth International Symposium on the Chemistry of Cement, Tokyo, 1968: pp. 53–66.
- [310] E.S. Boek, P.V. Coveney, N.T. Skipper, Monte Carlo molecular modeling studies of hydrated Li-, Na-, and K-smectites: understanding the role of potassium as a clay swelling inhibitor, J. Am. Chem. Soc. 117 (1995) 12608–12617, https://doi.org/ 10.1021/ja00155a025.
- [311] T. Underwood, V. Erastova, H.C. Greenwell, Ion adsorption at clay-mineral surfaces: the Hofmeister series for hydrated smectite minerals, Clay Clay Miner. 64 (2016) 472–487, https://doi.org/10.1346/CCMN.2016.0640310.
- [312] A. Moshiri, D. Stefaniuk, S.K. Smith, A. Morshedifard, D.F. Rodrigues, M.J. A. Qomi, K.J. Krakowiak, Structure and morphology of calcium-silicate-hydrates cross-linked with dipodal organosilanes, Cem. Concr. Res. 133 (2020) 106076, https://doi.org/10.1016/j.cemconres.2020.106076.
- [313] A. Morshedifard, A. Moshiri, K.J. Krakowiak, M.J.A. Qomi, Spectral attributes of sub-amorphous thermal conductivity in cross-linked organic-inorganic hybrids, Nanoscale 12 (2020) 13491–13500, https://doi.org/10.1039/D0NR02657C.
- [314] R. Gettu, J. Roncero, M.A. Martin, Long-term Behaviour of Concrete Incorporating a Shrinkage-reducing Admixture, Indian Concrete Journal, 2002.
- [315] H. Ai, J.F. Young, Mechanism of Shrinkage Reduction Using a Chemical Admixture, 1997, pp. 18–22.
- [316] I. Maruyama, K. Beppu, R. Kurihara, A. Furuta, Action mechanisms of shrinkage reducing admixture in hardened cement paste, J. Adv. Concr. Technol. 14 (2016) 311–323, https://doi.org/10.3151/jact.14.311.
- [317] A.B. Eberhardt, On the mechanisms of shrinkage reducing admixtures in self consolidating mortars and concretes, in: Bauhaus Universität Weimar 270, 2009.
- [318] J. Weiss, P. Lura, F. Rajabipour, G. Sant, Performance of shrinkage-reducing admixtures at different humidities and at early ages, ACI Mater. J. 105 (2008) 478
- [319] H. Rahoui, I. Maruyama, M. Vandamme, J.-M. Pereira, M. Mosquet, Impact of an SRA (hexylene glycol) on irreversible drying shrinkage and pore solution properties of cement pastes, Cem. Concr. Res.. (accepted).
- [320] M.O. Abadie, K.C. Mendonça, Moisture performance of building materials: from material characterization to building simulation using the moisture buffer value concept, Build. Environ. 44 (2009) 388–401, https://doi.org/10.1016/j. buildenv.2008.03.015.

Preflight Results

Document Information

Preflight Information

Title: Advances in atomistic modeling and understanding directly in the Republif in the Republic in the Republif in the Republic in the Republ

Creator: Elsevier Date: Aug 23, 2021 3:53:52 PM

Producer: Acrobat Distiller 8.1.0 (Windows)

Legend: (X) - Can NOT be fixed by PDF/A-1b conversion.

(!X) - Could be fixed by PDF/A-1b conversion. User chose to be warned in PDF/A settings.

Page 3 Results

(X) Font widths must be the same in both the font dictionary and the embedded font file.

Page 4 Results

- (X) Font widths must be the same in both the font dictionary and the embedded font file.
- (X) Font widths must be the same in both the font dictionary and the embedded font file.
- (X) Font widths must be the same in both the font dictionary and the embedded font file.
- (X) Font widths must be the same in both the font dictionary and the embedded font file.
- (X) Font widths must be the same in both the font dictionary and the embedded font file.

Page 5 Results

- (X) Font widths must be the same in both the font dictionary and the embedded font file.
- (X) Font widths must be the same in both the font dictionary and the embedded font file.
- (X) Font widths must be the same in both the font dictionary and the embedded font file.
- (X) Font widths must be the same in both the font dictionary and the embedded font file.
- (X) Font widths must be the same in both the font dictionary and the embedded font file.
- (X) Font widths must be the same in both the font dictionary and the embedded font file.
- (X) Font widths must be the same in both the font dictionary and the embedded font file.
- (X) Font widths must be the same in both the font dictionary and the embedded font file.
- (X) Font widths must be the same in both the font dictionary and the embedded font file.
- (X) Font widths must be the same in both the font dictionary and the embedded font file.

Page 6 Results

- (X) Font widths must be the same in both the font dictionary and the embedded font file.
- (X) Font widths must be the same in both the font dictionary and the embedded font file.
- (X) Font widths must be the same in both the font dictionary and the embedded font file.
- (X) Font widths must be the same in both the font dictionary and the embedded font file.
- (X) Font widths must be the same in both the font dictionary and the embedded font file.
- (X) Font widths must be the same in both the font dictionary and the embedded font file.

Page 7 Results

- (X) Font widths must be the same in both the font dictionary and the embedded font file.
- (X) Font widths must be the same in both the font dictionary and the embedded font file.
- (X) Font widths must be the same in both the font dictionary and the embedded font file.
- (X) Font widths must be the same in both the font dictionary and the embedded font file.

Page 9 Results

(X) Font widths must be the same in both the font dictionary and the embedded font file.

Page 11 Results

- (X) Font widths must be the same in both the font dictionary and the embedded font file.
- (X) Font widths must be the same in both the font dictionary and the embedded font file.
- (X) Font widths must be the same in both the font dictionary and the embedded font file.
- (X) Font widths must be the same in both the font dictionary and the embedded font file.

Page 12 Results

- (X) Font widths must be the same in both the font dictionary and the embedded font file.
- (X) Font widths must be the same in both the font dictionary and the embedded font file.
- (X) Font widths must be the same in both the font dictionary and the embedded font file.
- (X) Font widths must be the same in both the font dictionary and the embedded font file.

Page 12 Results (contd.)

- (X) Font widths must be the same in both the font dictionary and the embedded font file.
- (X) Font widths must be the same in both the font dictionary and the embedded font file.
- (X) Font widths must be the same in both the font dictionary and the embedded font file.
- (X) Font widths must be the same in both the font dictionary and the embedded font file.
- (X) Font widths must be the same in both the font dictionary and the embedded font file.

Page 13 Results

- (X) Font widths must be the same in both the font dictionary and the embedded font file.
- (X) Font widths must be the same in both the font dictionary and the embedded font file.
- (X) Font widths must be the same in both the font dictionary and the embedded font file.
- (X) Font widths must be the same in both the font dictionary and the embedded font file.

Page 14 Results

- (X) Font widths must be the same in both the font dictionary and the embedded font file.
- (X) Font widths must be the same in both the font dictionary and the embedded font file.
- (X) Font widths must be the same in both the font dictionary and the embedded font file.
- (X) Font widths must be the same in both the font dictionary and the embedded font file.
- (X) Font widths must be the same in both the font dictionary and the embedded font file.

Page 15 Results

- (X) Font widths must be the same in both the font dictionary and the embedded font file.
- (X) Font widths must be the same in both the font dictionary and the embedded font file.

Page 18 Results

- (X) Font widths must be the same in both the font dictionary and the embedded font file.
- (X) Font widths must be the same in both the font dictionary and the embedded font file.
- (X) Font widths must be the same in both the font dictionary and the embedded font file.
- (X) Font widths must be the same in both the font dictionary and the embedded font file.
- (X) Font widths must be the same in both the font dictionary and the embedded font file.
- (X) Font widths must be the same in both the font dictionary and the embedded font file.
- (X) Font widths must be the same in both the font dictionary and the embedded font file.
- (X) Font widths must be the same in both the font dictionary and the embedded font file.
- (X) Font widths must be the same in both the font dictionary and the embedded font file.
- (X) Font widths must be the same in both the font dictionary and the embedded font file.
- (X) Font widths must be the same in both the font dictionary and the embedded font file.
- (X) Font widths must be the same in both the font dictionary and the embedded font file.
- (X) Font widths must be the same in both the font dictionary and the embedded font file.
- (X) Font widths must be the same in both the font dictionary and the embedded font file.

Page 19 Results

- (X) Font widths must be the same in both the font dictionary and the embedded font file.
- (X) Font widths must be the same in both the font dictionary and the embedded font file.
- (X) Font widths must be the same in both the font dictionary and the embedded font file.
- (X) Font widths must be the same in both the font dictionary and the embedded font file.
- (X) Font widths must be the same in both the font dictionary and the embedded font file.
- (X) Font widths must be the same in both the font dictionary and the embedded font file.
- (X) Font widths must be the same in both the font dictionary and the embedded font file.
- (X) Font widths must be the same in both the font dictionary and the embedded font file.

Page 20 Results

(X) Font widths must be the same in both the font dictionary and the embedded font file.

Page 21 Results

- (X) Font widths must be the same in both the font dictionary and the embedded font file.
- (X) Font widths must be the same in both the font dictionary and the embedded font file.
- (X) Font widths must be the same in both the font dictionary and the embedded font file.

Page 23 Results

- (X) Font widths must be the same in both the font dictionary and the embedded font file.
- (X) Font widths must be the same in both the font dictionary and the embedded font file.
- (X) Font widths must be the same in both the font dictionary and the embedded font file.
- (X) Font widths must be the same in both the font dictionary and the embedded font file.
- (X) Font widths must be the same in both the font dictionary and the embedded font file.
- (X) Font widths must be the same in both the font dictionary and the embedded font file.

Page 24 Results

(X) Font widths must be the same in both the font dictionary and the embedded font file.

Page 30 Results

- (X) Font widths must be the same in both the font dictionary and the embedded font file.
- (X) Font widths must be the same in both the font dictionary and the embedded font file.

Page 32 Results

(X) Font widths must be the same in both the font dictionary and the embedded font file.

Page 33 Results

(X) Font widths must be the same in both the font dictionary and the embedded font file.